NANOPARTICLES IN THE SCANNING TRANSMISSION ELECTRON MICROSCOPE

A Dissertation

Presented to the Faculty of the Graduate School

of Cornell University

in Partial Fulfillment of the Requirements for the Degree of

Doctor of Philosophy

by

Sara Elizabeth Zacher

August 2009

NANOPARTICLES IN THE SCANNING TRANSMISSION ELECTRON MICROSCOPE

Sara Elizabeth Zacher, Ph.D.

Cornell University 2009

The process of improving and producing novel nanomaterials requires visibility at the nanoscale–something the scanning transmission electron microscopes (STEM), especially the new, aberration-corrected STEM, can provide. This thesis focuses on ways to improve our use of STEM on nanoparticles by understanding damage of quantum particles (QPs), and how annular dark field (ADF) can be used to measure QP shape and provide proofs for oriented attachment growth in quantum rods using both low- and high-resolution ADF imaging.

Also, in an attempt to increase our understanding of the differences between simulation and experimental images and how the probe behaves inside of the sample, simulated STEM ADF images of amorphous layers and small tilts in crystalline specimens were studied and experimentally measured and simulated convergent beam electron diffraction pattern intensities were closely matched by including inelastic scattering in the form of bulk plasmon scattering into simulation

BIOGRAPHICAL SKETCH

Sara Zacher was born Sara Elizabeth Maccagnano in Elko, Nevada in 1971, the youngest of four children. Her family moved from Nevada to Churchill, Montana, when she was four years old. Up through sixth grade she attended a small, two-room schoolhouse in Amsterdam, Montana, where grades 1-3 and grades 4-6 were in the same classrooms, mixing with and learning from and teaching eachother. After graduating from sixth grade she moved to Manhattan Public School where she graduated from high school in 1989. Not sure of what major to pursue, she decided against going to college right after high school and instead attended Bible school and worked a variety of jobs for ten years, seven of which she worked at Big Sky Carvers in Manhattan, Montana, as a professional artist painting decorative decoys. During her time at Big Sky Carvers she listened to a portion of A Brief History of Time by Stephen Hawking as a book-on-tape while painting and was inspired by the double-slit experiment described therein, which proved the wave-particle duality of electrons. She was so excited by the concept that she decided to become a physicist and, though she had never taken physics before, she quit her job and enrolled full-time as a freshman in physics at Montana State University in Bozeman, Montana, where she obtained her Bachelor of Science degree in Physics in 2003. She moved to Ithaca, New York, to attend graduate school in the Department of Applied Physics at Cornell University. In the midst of working on her degree she found an old friend, Steven Zacher, and they got married in March of 2007. Their first child, Christopher Steven, was born on February 11, 2009. She received her M.S. from Cornell in August of 2008 and her Ph.D. from Cornell in August of 2009.

This document is dedicated to my two men, Steven and Christopher.
It is also dedicated to my parents, John and Robyn, who taught me I could be anything.

ACKNOWLEDGEMENTS

First and foremost I would like to acknowledge my thesis advisor, Professor John Silcox, who enthusiastically took me into his group and guided my learning. His knowledge of electron microscopy and solid state physics is staggering, and at every meeting he manages to bring out some nugget of information or a reference that is beautifully relevant and helpful. My thanks go to him for his patience and gentle guidance as I explored many different aspects of colloidal quantum particles, some of which were developed into the chapters in this thesis. I also would like to thank Profs. Melissa Hines and W. Watt Webb for serving on my special committee.

The Cornell VG STEM is an outstanding instrument because of the tender care of Dr. Earl Kirkland and Mick Thomas, who trained me in the use of the STEM and kept it going during my six years of study. Special thanks to Mick for spending tedious hours realigning the STEM for the different optical settings required for some of my studies and for chasing down strange vibrations and charging issues with me. Also, to Earl, for patiently answering questions about his multislice programs and providing me with improved versions as he developed them.

My studies of quantum particles were possible because of the many splendid samples provided primarily by Professor Todd Krauss' group in the University of Rochester, with dots and rods designed and grown by his students Jack Calcines, Li Guo, Lisa Carlson, Meghan Hahn and Jeff Peterson. Jie Yao of Prof. Webb's group also provided excellent dots, as well as the group at Kodak with whom we collaborated. I would also like to thank Zhiheng Yu for bequeathing me the quantum particle study as he left the Silcox group and I entered it, and for giving me invaluable tricks for sample preparation and cleaning that saved

me months of frustration.

I also owe a debt of gratitude to K. Andre Mkhoyan, who spent five years with me in the basement of Clark and who was always there to answer any question or join in a discussion about how to run the STEM, solve sample problems, perform data analysis, prepare talks and publications, and how the world should be run. Without his help and company the time I spent in F7 Clark would not have been as fruitful professionally and would have been much less interesting. In every way he is on the happy end of any Gaussian distribution.

A graduate student who wants to remain sane needs a life that extends past the lab, and I would like to thank those who brought balance and refreshing in the midst of intense study. The lunchtime crossword group shared the joys and stresses of graduate student life and made lunch an oasis, and whose members included Michael and Alison Durst, Judy Cha, Alex Kwan, Jennifer Lee, Lena Fitting Kourkoutis and Kirsten Hensley. Kiran Thadani quickly became a sweet and sympathetic friend as we entered Cornell, and I look forward to a continuing friendship for life. The family that I gained when I entered the doors of Asbury Church has been so important for me, and I thank all of them for their love, prayers and acceptance. I especially thank Dave and Rachel Quigley for their friendship and support from the very beginning, dragging me out of the lab and into enjoyable reality when I most needed it.

I have such love and respect for my family whose unswerving support has given me ballast in times that seemed too dark to go on and who joined me in celebrating each small victory: my parents, John and Robyn Maccagnano, my amazing siblings and their spouses and children, and my large and very dear extended family.

I can't express enough thanks to my husband for the sacrifice and patience

and love he has shown as he put so much of his life on the side while I finished up my studies. When he moved to Ithaca and into my life he brought me immeasurable love, fun and life. He also gave me such amazing support while I developed our greatest collaboration; our son, Christopher. Thank you, Steve.

Finally, I would like to acknowledge my God who gave me the idea of being a physicist in the first place and the ability and the courage to pursue it, finish it and head into the next chapter of my life.

TABLE OF CONTENTS

LIST OF TABLES

LIST OF FIGURES

CHAPTER 1

INTRODUCTION

1.1 Quantum Nanoparticles

Quantum nanoparticles are of great value in our nano-crazy world because they are small and bright light sources that can provide many colors with ten times the brightness of organic dyes and with much less possibility of photobleaching. This makes them useful for many applications from biological dyes and imaging of single proteins in cancer cells [1] to traditional bulk solid-state territory like light-emitting diodes (LEDs) [2] and solar cell technology [3]. The color of light emitted by the quantum particle is easily engineered during growth by controlling the size of the particle.

In bulk semiconductors, the energy bands are a continuum of allowed states created by the overlapping of the atomic energy levels of the many atoms in the crystal. This continuum of allowed states becomes quantized as the bulk semiconductor reduces in size and the boundary of the crystal begin to play a role in the development of the states. Figure 1.1 shows a schematic drawing to illustrate this idea.

This quantization of energy states in the conduction and valence band can be understood by picturing the quantum particle, especially the quantum dot, as a particle-in-a-box problem. The particle in a box is confined in a potential which, in the case of the quantum particle, is created by the confinement of the exciton inside the boundaries of the nanocrystal itself. The exciton is considered confined if the Bohr radius of the exciton, a_B, is on the scale of or larger than the

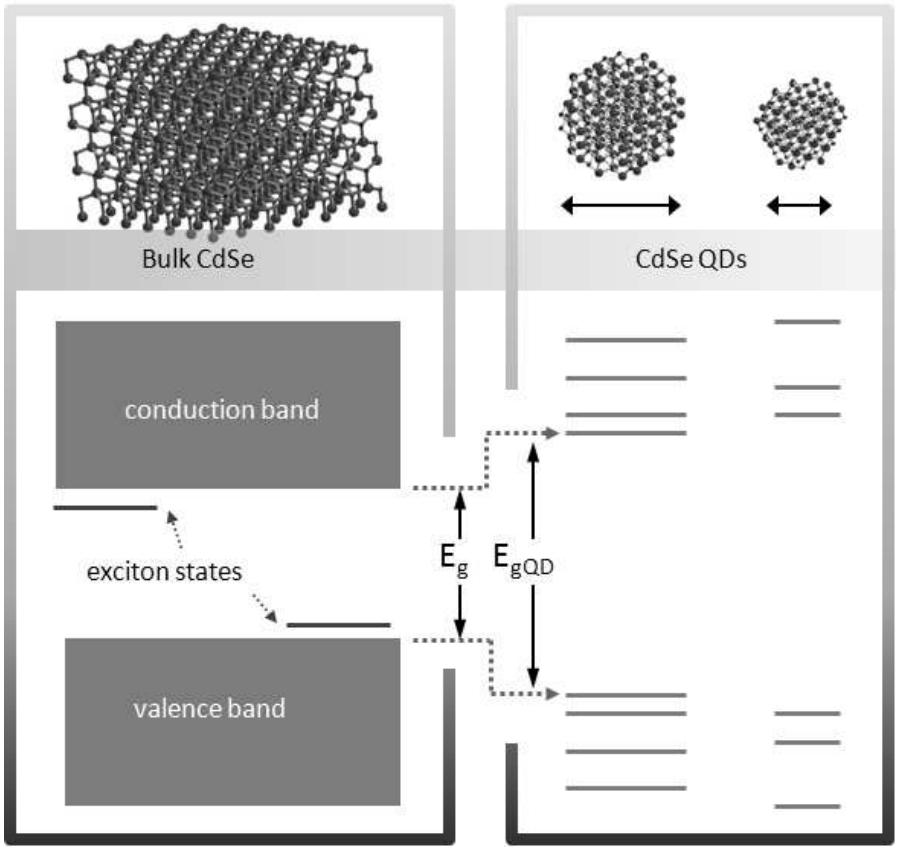

Figure 1.1: Schematic drawings showing energy bands of a bulk and nanoparticle CdSe semiconductor. As the semiconductor particle size moves from bulk to nanoparticle the band gap energy, E_g, between the bulk conduction and valence band increases to E_{gQD}, the energy gap between the ground energy states of the nanoparticle, which is inversely proportional to the square of the radius of the nanoparticle.

radius of the nanoparticle itself. For CdSe the a_B is 6 nm, which compares closely to the radii of the CdSe nanoparticles studied of ~5-15 nm.

The Hamiltonian of the electrostatic interaction of a hole and electron confined to a spherically symmetric potential, $U(r)$, is given as

$$H = -\frac{\hbar^2}{2m_e}\nabla_e^2 - \frac{\hbar^2}{2m_h}\nabla_h^2 - \frac{e^2}{\varepsilon_r|r_e - r_h|} + U(r) \tag{1.1}$$

where $\hbar$ is Planck's constant, r_e and r_h and m_e and m_h are the radii and effective masses of the electron and the hole of the exciton, e is the charge of the electron

and hole and ε_r is the dielectric function. This Hamiltonian can be solved for the energy levels in a spherical quantum dot, with the ground state energy given as:

$$E_{gQD} = E_g + \frac{\hbar^2 \pi^2}{2\mu R^2} \tag{1.2}$$

$$\mu = \frac{m_e m_h}{m_e + m_h} \tag{1.3}$$

where the energy of the band gap, E_g, is for that of the bulk semiconductor, R is the radius of the spherical quantum dot (QD), and μ is the reduced mass of the hole and electron.

To make the quantum particle shine it is exposed to UV light. Some of the light is absorbed and excites an electron from a valence state into a conduction state. The electron and hole are weakly bound to one another due to Coulomb forces. This electron-hole pair is the exciton, which remains confined within the crystal until the electron falls back to the valence state and recombines with the hole. The energy emitted by a QD, if the two states were the ground states calculated in Equation 1.2, will be E_{gQD} and will produce a photon of a wavelength corresponding to that energy. Because the square of the radius of the QD, R, is in the denominator of the second term of Equation 1.2, the energy of the gap in the QD, E_{gQD}, increases as the size of the particle gets smaller and, therefore, the color of the light emitted from the particle goes from red to yellow to green to blue as the size of the particle is decreased. A schematic illustrating the band gap increase is shown in Figure 1.1.

When the electron in the QD is excited, the valence and conduction bands are quantized and offer only a limited number of states into which to be excited. The smallest energy gap in the QD, from the highest valence energy state to the lowest conduction state, is similar to a 1s state in an atom. However, unlike an atom where the selection rules restrict transitions between states with Δl=±1,

the symmetry of the energy states for QDs allows only transitions of Δl=0 and consequently the electron from the valence 1s state is favored to go into the 1s conduction state. Likewise for p-like second-highest valence state and second-lowest conduction state. However, the 1p-like states are less likely to be excited than the 1s ground states of the quantum particle. Because the states in the quantum particle display this quantized behavior of energy states so similar to the orbitals of an atom, quantum dots are often called "super atoms".

The situation of the energy states in an actual quantum particle is much more complicated, however. Within the band gap are charge trap sites created by imperfect surface geometries of the crystal. These can cause the electron to recombine with charges in these sites instead of with its matching hole, releasing the energy in the form of heat instead of light. Figure 1.2 (a) shows a diagram of charge trap sites within the band gap and a schematic of an electron excited into a 1s electron state and then recombining with a surface charge to create two low-energy photons. Figure 1.2 (b) shows an experimental plot of the absorption and flourescence of a ~2.2 nm CdSe quantum dot (QD) as measured by the Krauss group. This QD, whose surface atoms consist of over half of the total atoms in the particle, has a small, narrow peak of flourescence at the expected wavelength for its radius (~480 nm) but also an additional broad peak in the red and infared wavelengths that suggest this QD's surface has charge trap sites that are recombining with the exciton electron. Much effort has gone into eradicating the surface charge trap sites, such as the addition of organic ligands and semiconductor capping layers. These additional layers create a sudden increase in band gap at the surface in an attempt to confine the exciton further within the core to prevent it from recombining with surface charges. This has worked with limited success. However, a new method of sintering a ternary core of CdZnSe

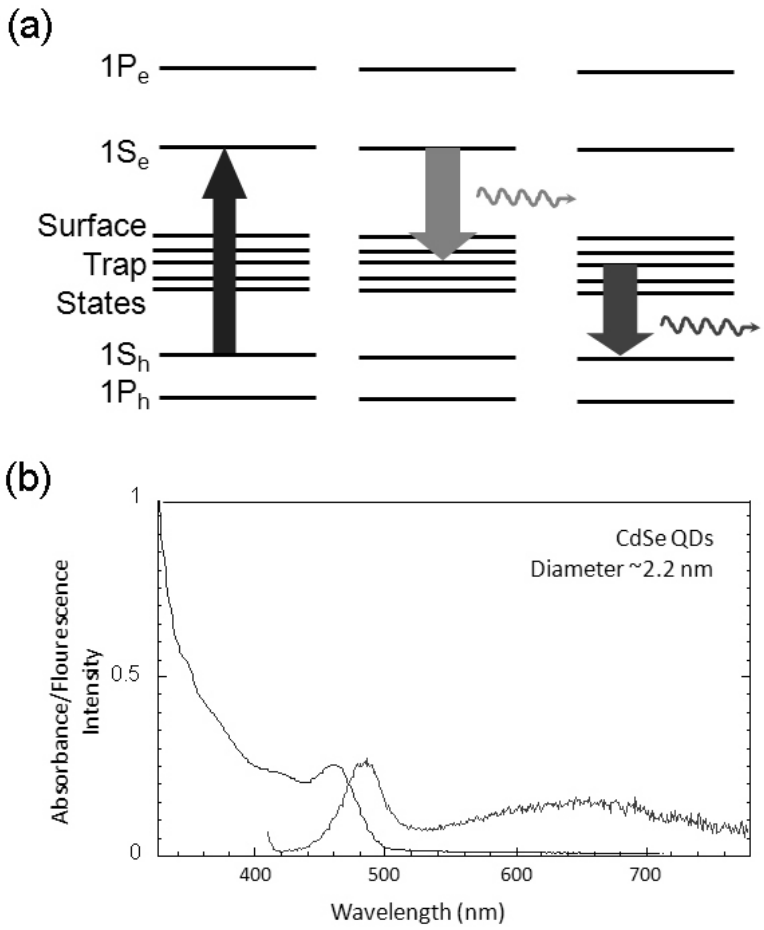

Figure 1.2: (a) Schematic of charge trap sites within the energy gap of a semiconductor nanoparticle. The arrow up represents an electron excited into the $1S_e$ conduction state and the two arrows down illustrate the absorption of the electron by surface charges, resulting in the creation of multiple low-energy photons. (b) Experimental measurements of the absorbance (left) and flourescence (right) peaks of a ~2.2 nm CdSe QD. The sharp peak at ~480 nm is the expected flourescence from this size of QD, but the broad peak centered at ~660 nm demonstrates the recombination of electrons into charge trap sites. Experimental measurements courtesy of the Krauss group.

with a shell of ZnSe, believed to have created a continuous boundary between core and shell, has produced unblinking, colloidally grown quantum dots for the first time [5].

The case study of the new, sintered, unblinking core/shell dots mentioned demonstrates the difficulties surrounding the characterization of novel nano-sized materials. Many aspects of the materials can be measured, such as emission and quantum yield, but measurements showing the arrangement of the atoms in the crystals, for instance the distribution of core and shell material at the atomic level, have been elusive. Other challenges in characterizing nanomaterials, especially nanoparticles, have been the difficulties of getting measurements of the crystal structure of a single particle, determining the robustness of nanoparticles under exposure to high-energy electrons, and predicting growth processes of nanoparticles from the "magic" seed particle to the often-elaborate structures grown in the colloidal processes. New microscopes capable of making nano-scale measurements, such as nanodiffraction and atomic-scale mapping of atom columns, are becoming available because of advances in aberration correction of electron probes in scanning transmission electron microscopes (STEMs). These instruments, with probes reaching sub-Ångström sizes, have the potential to provide the resolution needed to image and do science on these nanomaterials. However, the promised resolution will not be realized unless we are able to reduce signal noise wherever possible. Simulation can provide the answers, giving us the confidence that we are "seeing" what we think we are. It has been said that "we are blind at the nano-scale" [6] but these instruments can open up the vistas of the nano-world.

1.2 Nanomicroscopy, Nanodiffraction and Nanospectroscopy

The STEM is an ideal instrument to characterize quantum nanoparticles because of the ease of obtaining annular dark-field (ADF) images and the ability to obtain localized electron energy-loss spectra (EELS) and nanodiffraction information from specific areas on the nanoparticles. The ADF images are largely incoherent and are easily interpretable, especially for these extremely small particles. When the particles are homogeneous, the ADF images can be used to interpret the third dimension of thickness, giving a good idea of their shape very quickly. Because of the high contrast of the ADF images for even very tiny particles such as quantum nanoparticles, these images can also be used to interpret the distribution of sizes and aspect ratios for large rafts of particles [7]. When the particles are shelled to improve the quantum yield, EELS can be used to determine the distribution of the shell material [8] and the approximate size of the core particle [4]. Nanodiffraction can be used along the length of an extended-length nanoparticle, such as a nanorod or nanowire, to determine the crystal orientation to an accuracy not obtainable by using the features on the image itself [9, 10]. However, any measurement of a material in the STEM is subject to damage by the electron beam, and it is important to measure the robustness of the crystal under electron bombardment and the rate of material sputter when damage is present.

Advances in spherical aberration corrected conventional transmission electron microscopes (CTEMs) and STEMs [11, 12], where probe sizes reach below 1Å, allow imaging of crystalline specimens with atomic resolution routinely [13, 14]. However, a full understanding of all the processes that create the intensity variations in the high-resolution images (bright spots in the locations of the

atomic columns on a dark background) is still an unsolved problem. The problem exists for TEM bright field as well as for STEM ADF images. For CTEMs, the discrepancy between the contrasts obtained from theoretically modeled and experimentally recorded images, known as the "Stobbs factor", has been a subject of extensive research for many years. A series of papers by Boothroyd and co-authors discussing possible explanations deserve close attention [15, 16, 17].

The problem of the Stobbs Factor has caused so much interest because transmission microscopy will only be truly effective as a characterization tool and for in-situ science when the images and diffraction patterns collected are able to be matched by simulations. The simulations allow the microscopist to predict and calculate what is truly going on in the sample, as well as understanding fully the interaction of the electrons and (electron probe in the case of STEM) with the sample. Until the simulations match the measurements, can anyone be asked to believe that the microscopist truly understands their sample and the interaction of the incident electrons with the sample?

In early ADF-STEM studies the effects of phonon scattering [18] was discussed as the primary factor contributing to contrast reduction in experimentally recorded high-resolution images, and the contributions from plasmons was also discussed in early studies [19]. Studies described in chapters 3, 4 and 5 of this thesis investigate amorphous layers on the specimen, inelastic scattering and specimen tilt and their contribution to the contrast discrepancy between simulation (see also references [20, 21, 22, 23]). These studies relied heavily on the multislice method of simulating ADF STEM images and convergent-beam electron diffraction (CBED) patterns [24].

Similar studies have been done recently for high-angle ADF (HAADF) STEM

images using Bloch wave simulation and multislice simulation on crystal silicon [25] and $SrTiO_3$ [26], where the discrepancy between experiment and simulation was largely resolved by convolving the simulation images with a 0.08 nm full-width-half-maximum Gaussian. The Gaussian was chosen to represent the effect of a finite source size, but was found to be insufficient to explain discrepancies in further work with $SrTiO_3$, $PbTiO_3$, InP and $In_{0.53}Ga_{0.47}As$ [28]. In these [25, 26, 28] studies the Bloch wave simulations were similar to experimental image intensities only for thin samples, eg. 25 nm of $SrTiO_3$. The multislice method was found to match the intensities of thicker samples much more closely than the Bloch wave technique, but the computation time needed for multislice simulated images causes many researchers to continue to rely heavily on Bloch wave simulations.

This thesis will study the effect of amorphous layers, tilt and inelastic scattering on the ADF STEM images and the beam broadening that subsequently occurs in the STEM probe.

The thesis chapters are arranged in the following fashion: An introduction to STEM and the processes used in this thesis are in Chapter 2. Chapters 3, 4 and 5 explore the effect of beam broadening in STEM. Chapter 3 discusses the effect amorphous layers have on ADF STEM images of crystal Si using simulation. Chapter 4 makes a direct comparison of simulation with experiment using CBED patterns of amorphous Si, and Chapter 5 uses simulation to discover the contrast reduction of ADF STEM images that occurs with small sample tilts of crystal Si. Chapters 6, 7 and 8 show experimental use of STEM in studying quantum nanoparticles. Chapter 6 is an in-depth study of the damage that can occur on CdSe quantum nanorods using the focused electron beam. Chap-

ter 7 explores the use of the intensity of ADF images to understand the three-dimensional shape of quantum nanoparticles, and Chapter 8 discusses oriented attachment as a growth mechanism for quantum nanorods, using STEM ADF images.

BIBLIOGRAPHY

[1] I.L. Medintz, A.R. Clapp, F.M. Brunel, T. Tiefenbrunn, H.T. Uyeda, E.L. Chang, J.R. Deschamps, P.E. Dawson and H. Mattoussi, Nature Mat. **5**, 581-589 (2006).

[2] S. Coe, W.-K. Woo, M. Bawendi and V. Bulovi̇c, Nature **420**, 800-803 (2002).

[3] S.A. McDonald, G. Konstantatos, S. Zhang, P.W. Cyr, E.J.D. Klem, L. Levina and E.H. Sargent, Nature Mat. **4**, 138-142 (2005).

[4] L.J. Carlson, S.E. Maccagnano, M. Zheng, J. Silcox and T.D. Krauss, Nanoletters **7**, 3698-3703 (2007).

[5] X. Wang, X. Ren, K. Kahen, M.A. Hahn, M. Rajeswaran, S. Maccagnano-Zacher, J. Silcox, G.E. Cragg, A.L. Efros and T.D. Krauss, Nature **459**, 686-689 (2009).

[6] Statement widely attributed to the International Technology Roadmap for Semiconductors publications.

[7] Z. Yu, M.A. Hahn, S.E. Maccagnano-Zacher, J. Calcines, T.D. Krauss, E.S. Alldredge and J. Silcox, ACS Nano **2**, 1179-1188 (2008).

[8] Z. Yu, L. Guo, H. Du, T. Krauss and J. Silcox, Nanoletters **5**, 565-570 (2005).

[9] Z. Yu, M.A. Hahn, J. Calcines, T.D. Krauss, J. Silcox, App. Phys. Lett. **86**, 013101 (2005).

[10] Z. Yu, PhD Thesis, Cornell University, Ithaca NY 2004.

[11] M. Haider, S. Uhlmann, E. Schhwan, H. Ross, B. Kabius and K. Urban, Nature **392**, 768 (1998).

[12] P.E. Batson, O.L. Krivanek, N. Dellby, Nature **418**, 617 (2002).

[13] P.D. Nellist, M.F. Chisholm, N. Dellby, O.L. Krivanek, M.F. Murffit, Z.S. Szilagyi, A.R. Lupini, A. Borisevich, W.H. Sides, and S.J. Pennycook, Science **305**, 1741 (2004).

[14] K.A. Mkhoyan, P.E. Batson, J. Cha, W.J. Schaff and J. Silcox, Science **312**, 1354 (2006).

[15] C. Boothroyd and W.M. Stobbs Ultramicroscopy **26**, 361 (1988); C. Boothroyd and W.M. Stobbs Ultramicroscopy **31**, 259 (1989).

[16] C. Boothroyd, J. Microscopy **190**, 99 (1997).

[17] C. Boothroyd, Ultramicroscopy **83**, 159 (2000).

[18] R.F. Loane, P. Xu, J. Silcox, Acta. Cryst. **A47**, 267 (1991).

[19] P. Xu, R.F. Loane and J. Silcox, Ultramicroscopy **99**, 125 (1991).

[20] K.A. Mkhoyan, S.E. Maccagnano-Zacher, E.J. Kirkland and J. Silcox, Ultramicroscopy **108**, 791-803 (2008).

[21] S.E. Maccagnano-Zacher, K.A. Mkhoyan and J. Silcox, Quantitative Electron Microscopy for Materials Science, edited by E. Snoeck, R. Dunin-Borkowski, J. Verbeeck, and U. Dahmen (Mater. Res. Soc. Symp. Proc. Volume 1026E, Warrendale, PA, 2007), 1026-C16-02.

[22] K.A. Mkhoyan, S.E. Maccagnano-Zacher, M.G. Thomas and J. Silcox, Phys. Rev. Lett. **100**, 025503 (2008).

[23] S.E. Maccagnano-Zacher, K.A. Mkhoyan, E.J. Kirkland and J. Silcox, Ultramicroscopy **108**, 718-726 (2008).

[24] E. J. Kirkland, *Advanced Computing in Electron Microscopy* (Plenum Press, 1998).

[25] D.O. Klenov, S.D. Findlay, L.J. Allen and S. Stemmer, Phys. Rev. B **76** 014111 (2007).

[26] J.M. LeBeau, S.D. Findlay, L.J. Allen and S. Stemmer, PRL **100**, 206101 (2008).

[27] J.M. LeBeau and S. Stemmer, Ultramicroscopy **108**, 1653-1658 (2008).

[28] S.D. Findlay, D.O. Klenov, S. Stemmer and L.J. Allen, Mat. Sci. and Tech. **24**, 660-666 (2008).

CHAPTER 2

GENERAL INTRODUCTION TO STEM

In the world of electron microscopy, scanning transmission electron microscopes (STEMs) are showing themselves to be increasingly powerful instruments for atomic-scale analysis of many different systems. [1, 2, 3, 4] Starting with the first truly useable dedicated STEM, the ultra-high vacuum (UHV) STEM made by Vacuum Generators in the 1970s and 1980s implemented a high-brightness cold field emission source that allowed data to be taken with a small energy dispersion and in reasonable time scales. The STEM produces a focused electron probe which impacts a very small area on the sample. If the sample is thin enough (~300Å) most electrons travel through the sample and either pass through unaffected or interact in some way with the sample. Figure 2.1 shows the various ways by which the electrons that pass through the sample can be collected. Images of the sample can be created by rastering the probe wherein each spot where data is collected constitutes a pixel on the image. Two kinds of images, bright field (BF) and annular dark field (ADF), can be taken simultaneously using STEM. BF images are created from electrons that are unscattered or are scattered to low angles (from zero to a few mrad), and electrons scattered to high angle (>~30 mrad) are collected to form ADF images.

Electrons that are unscattered or scattered to low angles can also be sent through a spectrometer and sifted according to energy to create electron energy loss spectra (EELS). The EELS data can be taken in raster mode, and therefore represent a larger portion of the sample, or in spot mode where the beam is held stationary. ADF values can also be taken simultaneously with EELS in spot mode, and an example of how this can be used is shown in Figure 2.2

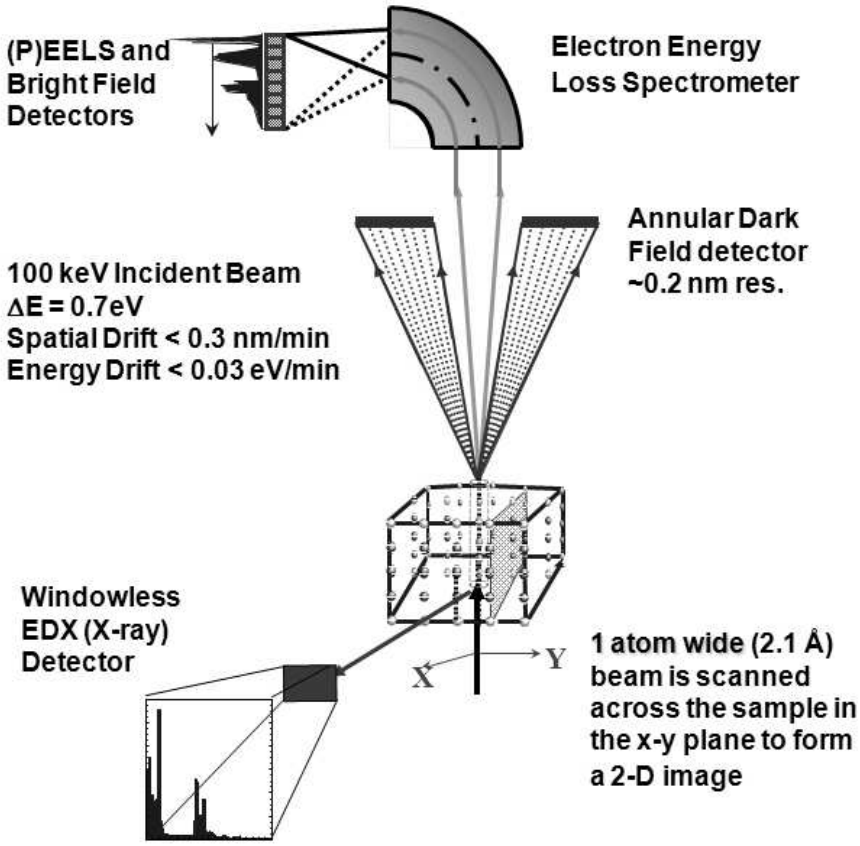

Figure 2.1: Schematic showing the different ways to collect electrons transmitted through the sample. The ADF collector gathers electrons scattered to high angle, the electrons scattered to low angles are collected either by a BF detector to be made into an image or sent through a spectrometer and plotted as an energy loss spectra with the EELS detector. Also, the fast electrons create X-rays that can be collected with the EDX detector.

where the EELS signal from the shell material, sulfur, of a core/shell quantum dot is plotted as a function of distance across the dot. At the same time the ADF intensity of each spot is plotted with the ADF intensity being largest where the dot is thickest. This simultaneous acquisition of data in perfect registration (within one pixel) allows for analysis of the distribution of shell material on the quantum dot and, in this particular case, makes it possible to locate and measure

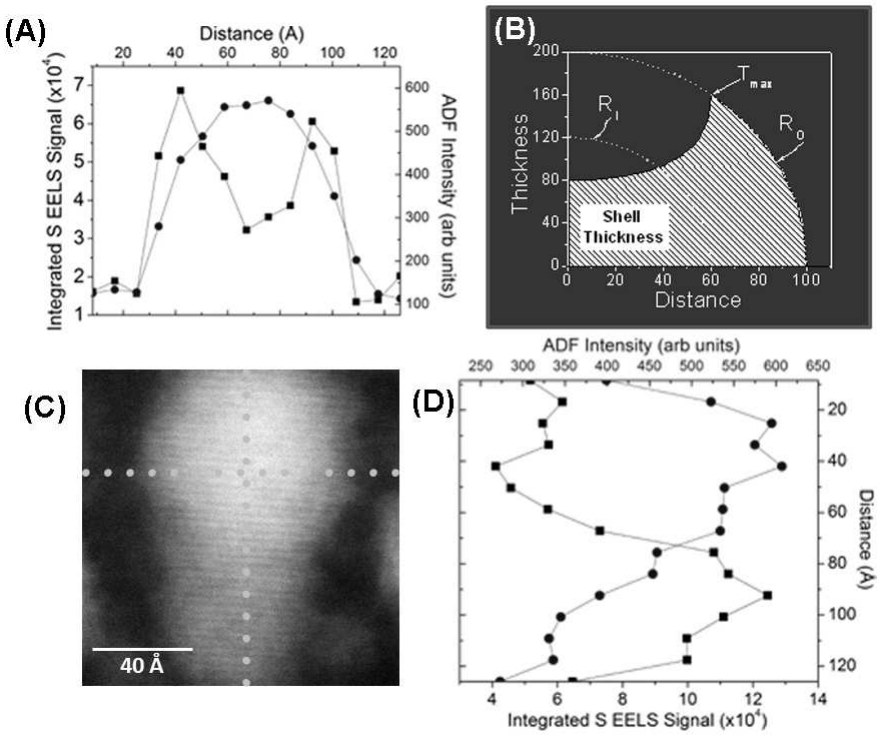

Figure 2.2: (A) and (D) show plots of ADF intensity (squares) and relative amount of sulfur (circles) across the short and long axis of an elongated core/shell CdSe/CdS QD. The ADF image of the dot taken before the measurement is shown in (C) with circles marking the areas from which data was taken. (B) demonstrates the relative thickness distribution of shell material to be expected from a uniformly shelled spherical QD. The inner (R_0) and outer (R_1) boundaries of the shell are sketched on the thickness diagram. The use of ADF intensities to learn something about thickness is covered in Chapter 7 of this thesis.

the QD core.

The optics in the STEM can be chosen to allow the measurement of diffracted electrons. Diffraction patterns can be created by either using a large, parallel beam and finding the selected-area diffraction (SAD) or by using a focused probe and gathering the convergent-beam electron diffraction (CBED) pattern. SAD patterns give information about a micron-sized area, and can be used for crystal alignment and detecting areas of strain. Because of the small probe used

to create them, CBED patterns give information about sub-nm and nm sized areas and can be used to analyze atomic parameters and thickness. A modified optical setting that creates SAD patterns from a very small (~7 nm), almost parallel probe is called nanodiffraction, and is used in Chapter 4 to find small-angle rotations along the length of a nanoparticle. Finally, energy dispersive X-rays (EDX) created by the high-energy STEM electrons can be detected and used to analyze the sample.

2.1 Operational Details

The bulk of the experiments in this thesis were performed using the Cornell ultra-high-vacuum (UHV) VG-HB501 STEM operated using a 100 keV electron beam (Figure 2.3). The microscope was installed at Cornell in 1987, and has been in operation ever since. Modifications made to the original microscope include an improved ADF detector system [5], a computer interface for digital recording of data [6] and the installation of a parallel EELS (PEELS) detector [7, 8].

The VG STEM uses a high-brightness cold field emission gun as a source, and a gun lens directly above the gun anode focuses the emitted electrons to increase the current of the electron beam. The beam current under standard operating parameters is ~15 pA and has an energy spread of ± 0.35 eV. The electrons emitted by the gun leave the gun chamber, whose pressure is ~10^{-12} Torr, and enter the microscope chamber, held at ~3x10^{-10} Torr. A detailed optical schematic of the main microscope chamber is shown in Figure 2.4. After passing through the gun lens and into the main microscope chamber, the electrons pass through the condenser lens(es). For imaging and most diffraction modes, only one of the two identical condenser lenses is used to demagnify the source

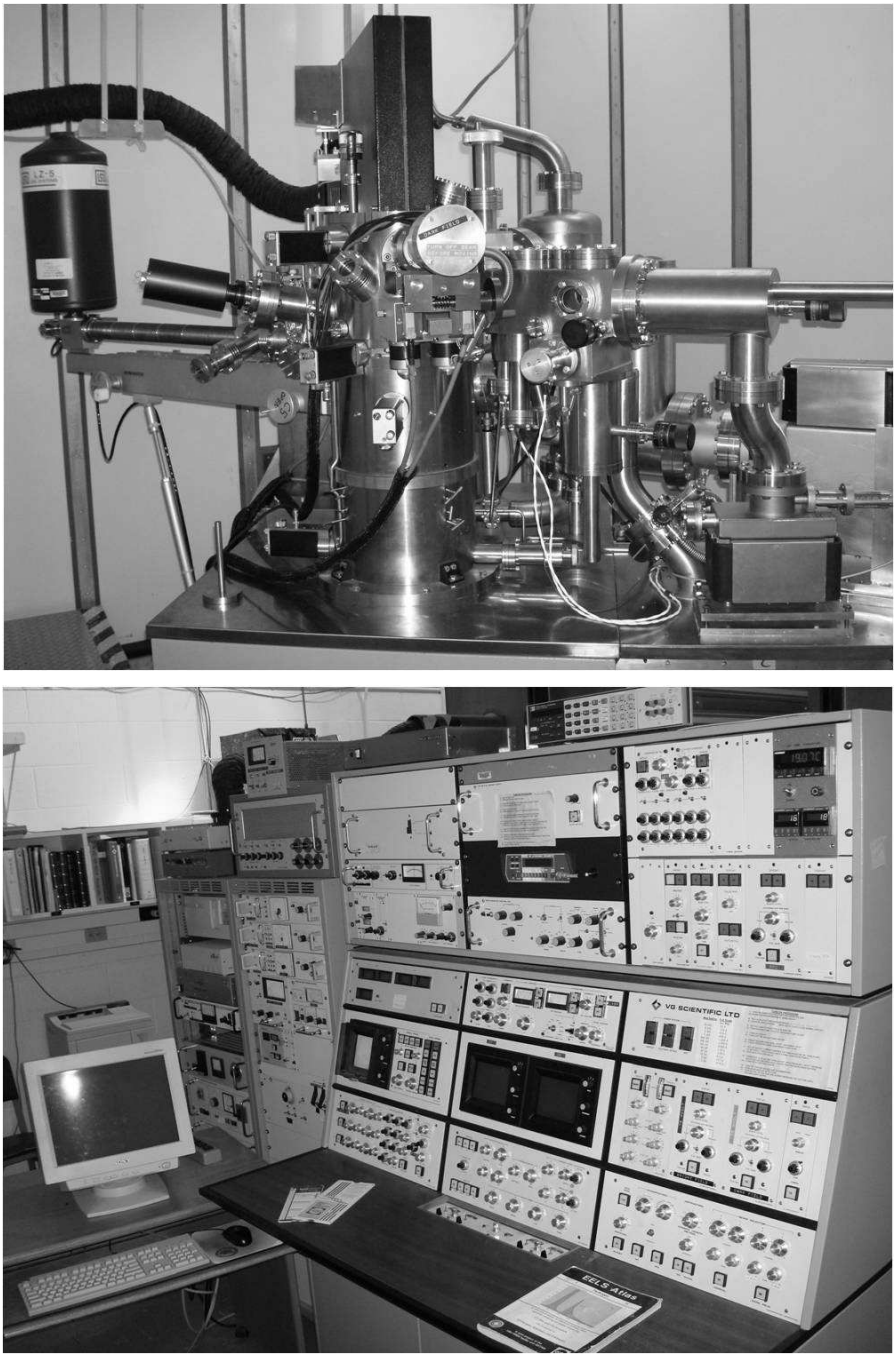

Figure 2.3: Pictures of the column (upper) and control panel (lower) for the Cornell VG STEM microscope.

(namely lens C2). However, for nanodiffraction (the acquisition of diffraction patterns from a nanometer sized area) both C1 and C2 are used. The next lens the electrons encounter is the objective lens (spherical aberration C_s=1.3 mm) which focuses the electron beam onto the sample as a probe whose FWHM is approximately 0.2 nm. A physical objective aperture can be used to set the convergence angle (~10 mrad) of the electron probe or the virtual objective aperture (VOA) below the condenser lenses can also be used for this purpose. The beam is rastered over the sample using the scan coils which are located pre-specimen, and electrons that go directly through or are scattered to low angles pass through the collection aperture and into the BF detector. The electrons that scatter to high angle are collected by the ADF detector, which can have a variety of inner and outer angles but which are set fixed in the Cornell microscope at 54-330 mrad. The Grigson coils, located post-specimen, are used to scan diffraction patterns onto the BF detector.

2.2 ADF Images

Unlike BF images where the phase relationships of the incident, unscattered electron wavefunction, $\psi_0(x - x_0, y - y_0, \vec{k})$ and the final, scattered wavefunction, $\psi(x, y, \vec{k})$ control the intensities detected at the detector plane for pixel x_0, y_0, the electrons collected by the annular detector are largely incoherent and the intensity of each pixel in the image is determined by,

$$I_{adf} = \int_{k_{outer}}^{k_{inner}} |\psi(x, y, \vec{k})|^2 2\pi k dk \tag{2.1}$$

where $\psi(x, y, \vec{k})$ is dependent upon the spatial coordinates x and y and the wave vector $\vec{k}$. The integral is summed over the total angle of the detector, k_{inner} to

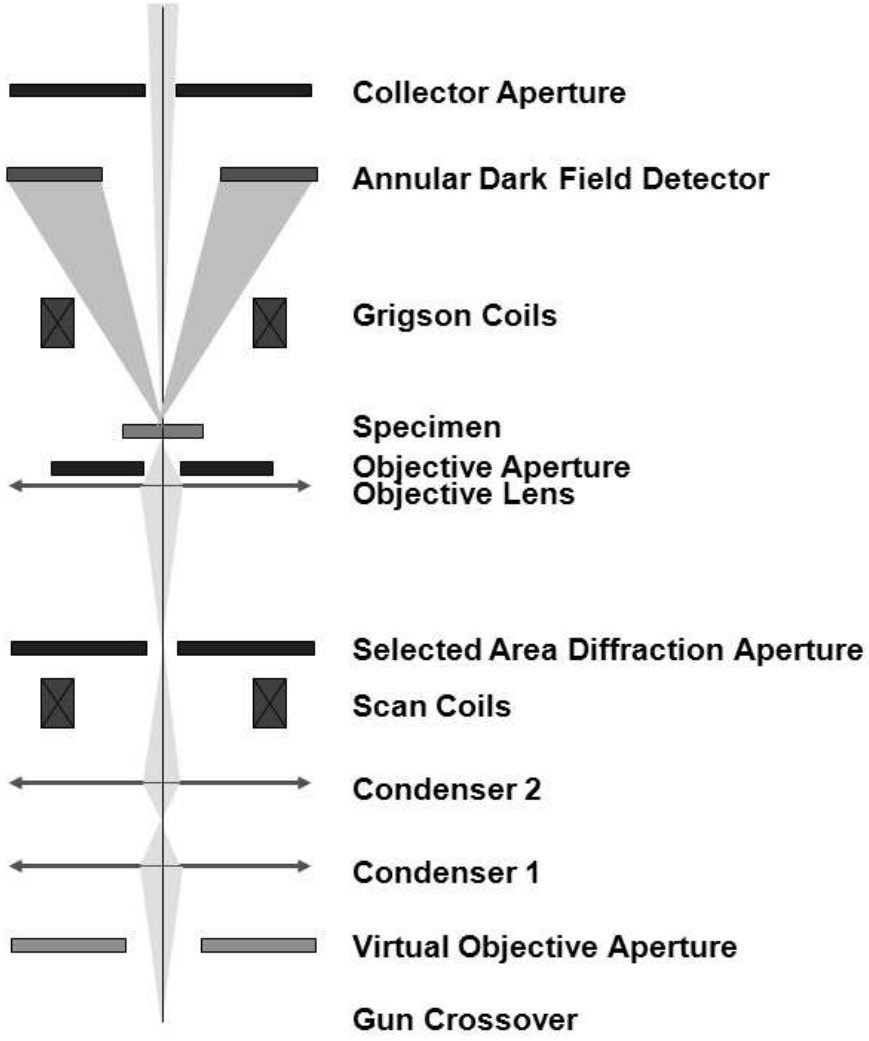

Figure 2.4: Optical schematic of the STEM microscope showing the main lenses, apertures and collectors.

k_{outer}. This incoherency of the scattered electrons makes the ADF images easy to interpret since areas that scatter highly are bright and areas that scatter very little are dark. For example, in all but the thickest samples, ADF intensities for the atom columns in a crystalline sample image are bright and the spaces between the columns are dark. This is rarely true of BF images, where the phase contrast may cause a contrast reversal making atom columns appear dark or bright depending upon the defocus of the microscope. Another advantage of ADF is

the thickness contrast in the images. Thicker areas in the sample scatter more electrons to high angle than thin areas, so for samples of homogeneous material the contrast in the image shows thickness variations. The interpretation of this contrast is explored in detail in Chapter 9 of this thesis. Further, atoms of higher chemical or atomic number, or Z, scatter more electrons to higher angle than low-Z atoms and therefore create a Z-contrast in the ADF images. This can be seen quite clearly by the image in Figure 2.5 where the single higher-Z atom of gold has good contrast against the lower-Z carbon substrate, even though the carbon substrate is much thicker than one atom. The ADF intensity due to Z-contrast has been shown to be proportional to Z^x where x is somewhere between 1.5 and 2 approaching 2 with very large inner angles of the ADF detector [9]. High angle scattering approaches Z^2, modeling the Rutherford scattering from an unscreened nucleus. As lower angle scattering is included, however, the screening of the nucleus by core-shell electrons becomes important, and reduces the Z-dependence to somewhere between Z^2 and $Z^{1.5}$. Kirkland, et al. [10] calculated the elastic partial cross-section for 100 keV electrons as a function of Z, and plotted the results for four different ADF inner angles. These plots are shown in Figure 2.6. The curve labeled (c) is one calculated for an ADF detector whose inner angle (50 mrad) is very close to that of the Cornell VG STEM (54 mrad). The slope of this line is 1.7, thereby estimating the Z-dependence of ADF images produced on the Cornell VG STEM to be $Z^{1.7}$.

Though most of the electrons scattered to high angle are incoherent, some dynamic processes such as multiple scattering and beam channeling can cause the images to become less straightforward than simple Z- and thickness-contrast would suggest (See Figure 5 in Stallknecht, et al. [12]). This complication of the ADF images with dynamic processes can occur even when the inner angle of

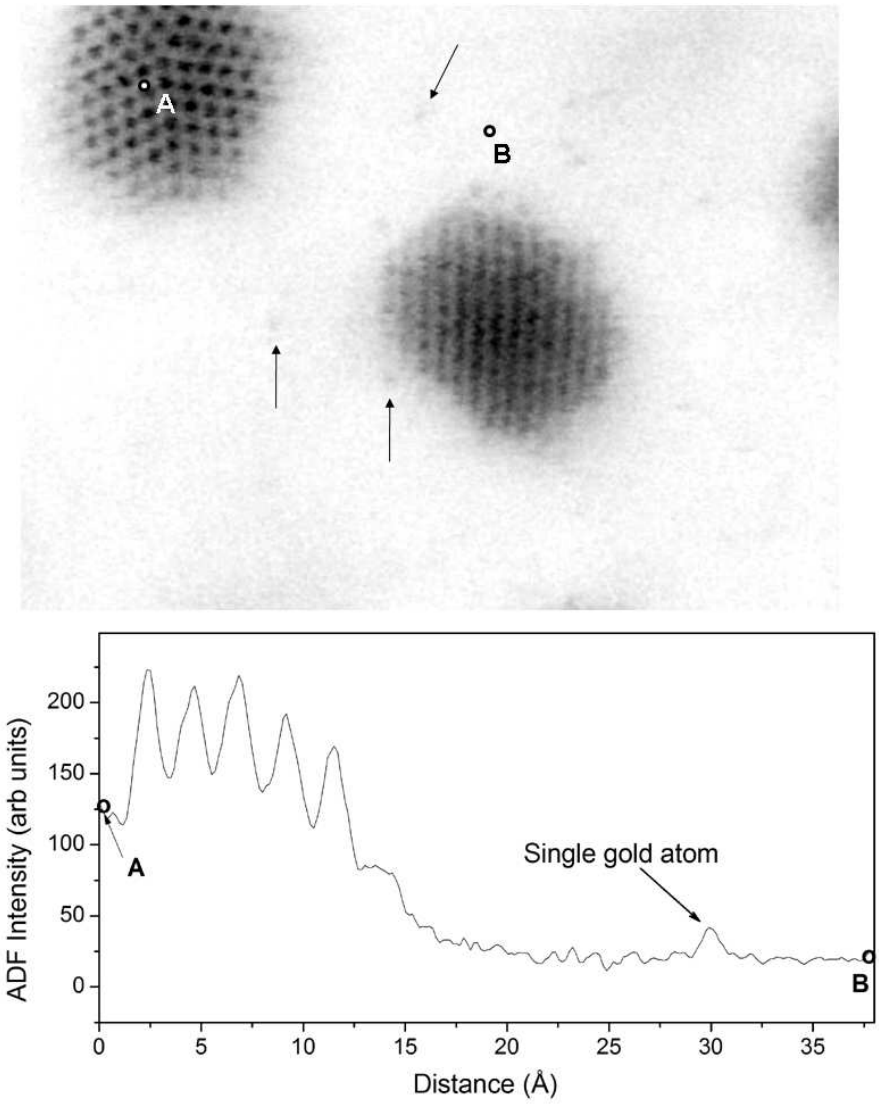

Figure 2.5: (Upper) ADF STEM image of gold particles acquired with an aberration-corrected microscope. With the small probe of ~1 Å, individual gold atoms are visible on the carbon substrate. Grey arrows point to a few of the bright spots corresponding to gold atoms. A linescan was taken of the ADF intensities between points A and B and are plotted below the image. (Lower) Plot of the ADF intensity linescan between points A and B showing the bright columns of gold atoms from the particle and the small peak above the carbon background from an individual gold atom. The ADF image was filtered to remove background noise with a simple Butterworth high-pass filter.

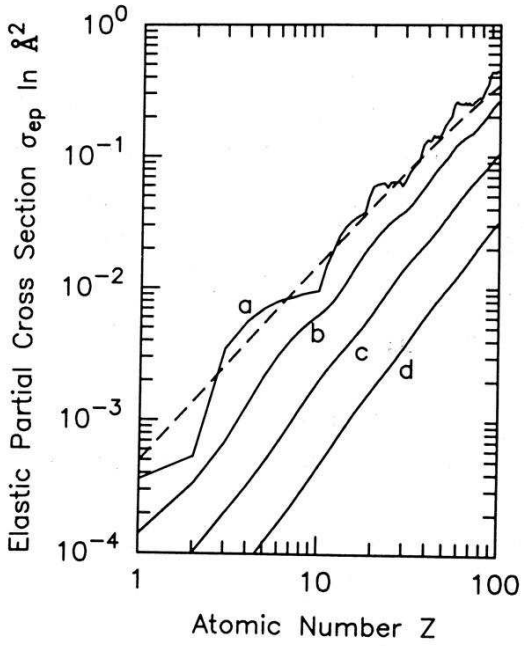

Figure 2.6: Plot of the elastic partial scattering cross-section of 100 keV electrons as a function of atomic number, Z. The cross-sections were calculated with the eikonal approximation, and only the electrons scattered into an annular dark field detector contributed to the cross-section. The detector ranges for the curves are (a) 0-200 mrad, (b) 20-200 mrad, (c) 50-200 mrad, and (d) 100-200 mrad. The dashed line is the curve fit by Langmore, Wall and Isaacson [11]. The plot was calculated by Kirkland, et al. [10].

the ADF detector is sufficiently large to eliminate the collection of coherently scattered electrons. This can be explained by the fact that the scattered electrons are coming from an electron probe whose shape is being altered by coherent scattering as it travels through the sample, and this changing shape is being mapped by the elastically, incoherently scattered electrons. However, if the inner angle of the ADF detector is not large enough coherently scattered electrons can find their way into the images (and CBED patterns) and cause further confusion. Some of the artifacts in image intensity from dyanmic processes such as beam channeling and multiple scattering are shown in Chapter 5 in simulated

ADF images of tilted silicon crystals.

Having an inner angle that is ”large enough” to eliminate the collection of coherently scattered electrons is a definition that changes since scattering angle depends upon the scattering factors in each particular sample. A simple way to define low-angle ADF (LAADF) and high-angle ADF (HAADF) would be to look at the angular distribution of the scattered intensities of a sample. HAADF detectors would be those that choose only scattering angles that no longer include diffraction peaks and other coherent effect, whereas LAADF detectors would have coherently scattered electrons included. Such an effect was shown by Yu et al. [13] where in Figure 5 of the paper they show how strain amplitude changes the image intensity for the LAADF image (20-64 mrad) and is constant for the HAADF image (64-200 mrad).

2.3 EELS

When the fast electrons from the STEM probe interact with atoms in the sample, inelastic scattering can occur in several ways. The electrons may interact with the vibrations of the lattice and lose energy in the range of 10-100 meV due to phonons. With the Cornell VG STEM these losses are not able to be resolved in the EELS spectra because they are swamped by the peak in signal due to the majority of electrons that pass through with no energy-changing interactions, called the zero-loss peak. With improved EELS energy resolution the phonon signal can be resolved [14].

Most of the inelastic scattering events in EELS occur with the valence electrons (or conduction electrons in metals). These electrons can be approximated

as a continuum, or sea of electrons in the solid that begin to oscillate when perturbed by the fast incident electron. These oscillations are called plasmons, and are quickly damped and long-range. The plasmon energy loss in the EEL spectra is found in the low-loss region, from 0-50 eV, and consists of bulk plasmons excited from the volume of the sample, multiple plasmon peaks due to multiple scattering in the volume, and surface plasmons from two-dimensional electron density oscillations localized at the sample surface or at interfaces. Surface plasmons tend to be at lower energy than bulk plasmons and the loss peaks are of less intensity than bulk losses because of the relatively insignificant area of the surface compared to the bulk except in very thin samples. Plasmons and the theory used to calculate their energy dispersion are discussed in Chapter 4 and Appendix A.

When inner-shell electrons of the atoms in the sample are excited by the incident electron, core-shell losses are detected in the EELS at distinct energies for different atoms. Because the energy of the incident electrons (100 keV) is much higher than the energy of the interaction (<1 keV), the first Born approximation can be used to find a differential cross-section for a scattering event with an inner-shell electron:

$$\frac{d^2\sigma(E,q)}{dEdq} = \frac{8\pi e^4}{\hbar^2 v^2}\frac{1}{q^3}\sum_f |M_{0f}|^2 \delta(E-(E_f-E_0)), \tag{2.2}$$

$$M_{0f} = \langle \psi_f | e^{i\vec{q}\cdot\vec{r}} | \psi_0 \rangle \tag{2.3}$$

$$N_{0f} = \delta(E-(E_f-E_0)) = \text{final density of states} \tag{2.4}$$

where ψ_f and ψ_0 are the final- and initial-state wavefunctions with energies of E_f and E_0 respectively, and q is the momentum transferred in the inelastic scattering event. Over a small range of energies, M_{0f} is a slowly varying function of energy loss and therefore any changes in the cross-section (and number of

scattering events) should roughly map the final density of states (DOS) above the Fermi level. This is not exactly true, but the core-loss EEL spectra has been found to match the general location of peaks in the DOS though often not matching the predicted intensity. When a small collection aperture is used and only electrons scattered to very small angles are collected, the dipole approximation applies and the transition matrix becomes

$$M_{0f} = i\langle\psi_f|\vec{q}\cdot\vec{r}|\psi_0\rangle. \tag{2.5}$$

Therefore, dipole selection rules apply and $\Delta l = \pm 1$ and in excitations Δl will almost always be +1. This means that K-shell (1s) electrons will be excited into p states and L-shell electrons will be excited into d states. The fine structure of K-edges will look different than those of L-edges, and therefore N_{0f} is a symmetry-projected DOS. Also, because the core-shell excitations are very localized, the DOS from different atoms in different lattice positions will reflect their individual bonding and environment. Therefore N_{0f} is also a local DOS. Another convenient feature of the core-shell edges is that the integration under the edge is proportional to the number of atoms that created it. This can be used to measure the relative amount of a particular material on the sample either as a function of distance or as a function of time. The use of EELS to measure the change in amount of shell-material (sulfur) across the diameter of a quantum dot was shown previously in Figure 2.2. Chapter 8 will show the use of EELS to measure the reduction of Cd as a function of time in a CdSe quantum rod due to beam damage.

2.4 Multislice

The multislice method of simulating TEM and STEM images and diffraction patterns has been successfully implemented to understand experimental observations of the changes in the contrast of the crystal lattice fringes as a function of defocus, [15, 16] and CBED patterns [17]. It has also been used to describe the effects of beam broadening in GaN/AlN quantum wells [18]. A large portion of this thesis uses the multislice method to predict what happens to the electrons as they pass through various materials, giving a basis for understanding and accurately interpreting experimental results.

The algorithm for all calculations of ADF-STEM images is based on the multislice method first proposed by Cowley and Moodie [19], developed by Ishizuka et al. [20, 21], and further developed and made accessible by Kirkland [22].

High-energy electrons traveling through crystals experience forces due to the potentials of the atoms. The multislice program calculates the potentials in the crystal and the transmission of the electrons through these potentials. Instead of calculating the potential of the entire crystal, however, it is easier to approximate the thin crystal as a series of very thin slices. Each slice can then be analyzed separately, simplifying the calculation of the potential and the transmission of the electron beam and the transmitted beam can be subsequently propogated to the next slice of crystal and the calculation can be run again.

The potential for one slice in the crystal consists of collecting the locations in x and y of all the atoms in the slice, placing them in the same z-plane, calculating the potential due to each atom, and then summing the potentials up for that

slice. This way of calculating potentials ignores the charge redistribution due to bonding between atoms, but because the electron beam used in these simulations is a high-energy one the effects from such inter-atomic forces will be a small perturbation of the potential and can thus be disregarded [23].

To calculate the propagation and transmission of a beam of fast electrons, one must solve the wave equation for these electrons,

$$\frac{\partial\psi(x,y,z)}{\partial z} = \left[\frac{i\lambda}{4\pi}\nabla_{xy}^2 + i\sigma V(x,y,z)\right]\psi(x,y,z), \tag{2.6}$$

where $\psi(x,y,z)$ is the electron wavefunction and $V(x,y,z)$ is the projected potential at a depth z in the crystal, λ is the wavelength of the incident electrons, and $\sigma = 2\pi me\lambda/h^2$ is the interaction parameter of the electron passing through the crystal potential. The wave equation can then be solved for the wavefunction at some small distance through the crystal, $z + \Delta z$ as,

$$\psi(x,y,z+\Delta z) = p(x,y,\Delta z) \otimes [t(x,y,z)\psi(x,y,z)] + \vartheta(\Delta z^2), \tag{2.7}$$

where $\psi(x,y,z+\Delta z)$ is the electron wavefunction, $\psi(x,y,z)$, after traveling from z to $z + \Delta z$, $p(x,y,\Delta z)$ is the propagation function through a small distance, Δz, and $t(x,y,z)$ is the transmission function of the electron in the slice at the depth z in the crystal. The transmission function consists of scattering the fast, incident electron by adding a phase shift proportional to the projected potential of the atoms in each slice to the wave function of incident electron, and the propagation function between slices can be treated as a Fresnel diffraction.

To practically create these simulated images and diffraction patterns for STEM, first, the complex, incident probe wavefunction must be created using typical experimental parameters. The crystal itself also is created by generating an XYZ file describing the exact location of each atom for a unit cell. This unit

cell must be replicated an integer number of times in the x, y and z directions depending upon the size of the crystal defined by the user. The potentials must be calculated for each slice, the slice thickness also defined by the user with typically an atomic layer for each slice. The potential for each slice can then be calculated.

Once the probe and the potential for a slice is calculated, the transmission of the probe through the potential and the propagation to the top of the next slice is accomplished by using Equation 2.7. This process is continued until the bottom of the crystal is reached. Figure 2.7 shows a diagram that roughly illustrates how the crystal is divided into slices and how the wavefunction propagates and transmits from slice to slice. The final wavefunction is the CBED pattern of the electron probe through the crystal. This CBED pattern can be used on its own or it can be used to create an ADF image. The ADF intensity is calculated by summing up all of the electrons in the CBED pattern that are elastically scattered from the atoms of the specimen into the conical solid angle of the ADF detector. This intensity is the value for one pixel of the image. To create the rest of the ADF image the probe is moved to a new spot on the specimen and the calculation is done all over again, repeating this process until the entire image is created. The thermal vibrations of the atoms (or phonons) are included in the calculation by randomly displacing atoms from their lattice sites using a Gaussian distribution function with the corresponding Debye-Waller factors [17] for each atom species.

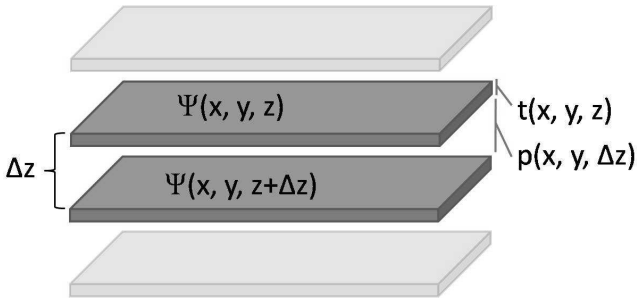

Figure 2.7: A rough illustration of how the crystal is divided into slices for the multislice simulation method. The electron wavefunction, $\psi(x, y, z)$, enters the slice at z and is transmitted through the projected potential with the function $t(x, y, z)$. This newly phase-shifted wavefunction is then propagated through a distance Δz by the function $p(x, y, \Delta z)$ until it reaches the top of the next slice at $z + \Delta z$. The process can now be repeated for the new wavefunction, $\psi(x, y, z + \Delta z)$, using the projected potential at $z + \Delta z$.

2.5 Quantum Particle Sample Preparation

The quantum rods (QRs) used in this thesis were produced by the Krauss group at the University of Rochester and were synthesized according to variations on literature procedures [24, 25, 26]. Samples for use in the STEM are made by depositing a ~20 μL drop of the QR suspension onto an ultrathin carbon film on a holey carbon support film [27]. This provides a sufficiently thin and low-contrast substrate for such tiny specimens.

The presence of trioctylphosphine oxide (TOPO) and other miscellaneous organics in the synthesis of the QRs and other colloidally-grown quantum particles (QPs) introduces a large amount of potentially contaminating organic carbon into the STEM sample. This contaminant may not cause a detrimental loss of contrast in conventional TEMs, but is a persistent problem for those trying to do high-resolution imaging in the STEM. The following section discusses various methods found to reduce and, sometimes, eliminate the occurrence of con-

tamination on these colloidally-grown QPs.

The first step taken to reduce contamination on the TEM QP samples is simply to use clean implements, surfaces and gloves every time a sample is prepared. The tweezers and surfaces are washed with an acetone rinse, and then further with a methanol or ethanol rinse to remove as much of the acetone as possible.

After the sample has been deposited on the grid, the grid is placed over a bath of boiling acetone and allowed to sit in this acetone reflux system for ~15 minutes. It is then removed from the acetone reflux system and placed immediately into the VG STEM prep chamber which is held at a vacuum of $\sim 10^{-7}$ Torr. A photo of the acetone reflux system is shown in Figure 2.8.

The Cornell VG STEM prep chamber has been fitted with a heater bulb which is set to allow a bake temperature on the sample of ~120°C. The sample is baked for two hours unless it is suspected to be a particularly dirty sample, when it is then baked for four hours initially. The sample is cooled overnight and placed directly into the STEM column to determine the contamination level. This baking of the sample is, in the author's opinion, the most effective single method found for cleaning these kinds of samples and creating useable samples from heavily contaminated ones that, unbaked, could not even be used for low-resolution imaging. Baking can also clean a marginal sample to the point that it can be used for spot-mode EELS, which requires the probe to be held in one position from 10 seconds to 4 minutes or more. A hotter bake may be found to be even more effective but was untried in these experiments because the temperature of 120°C was set as a maximum in the Cornell VG STEM due to the heat sensitivity of the sample holder and not the sample itself.

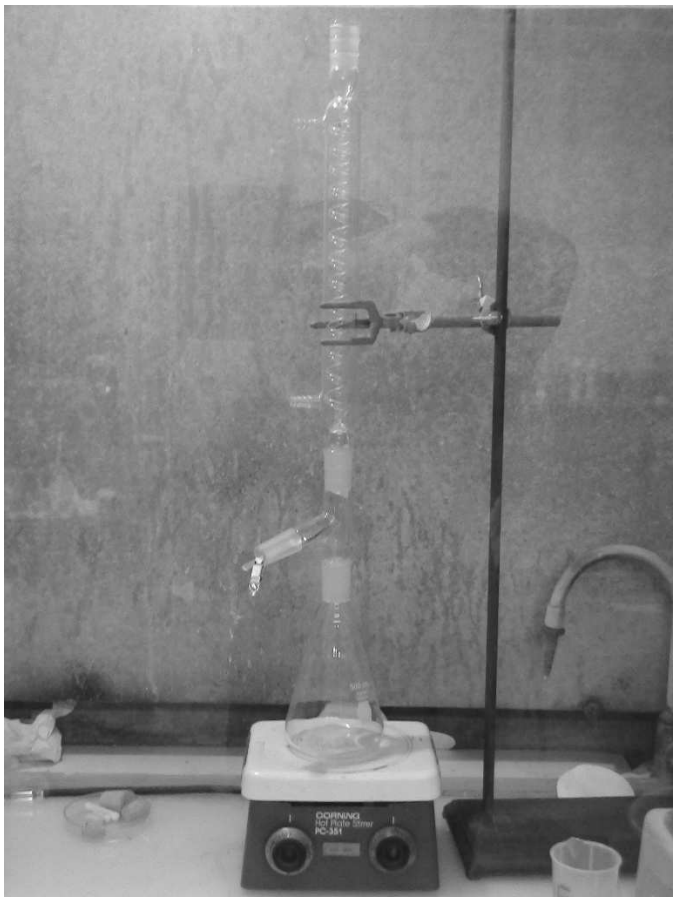

Figure 2.8: Photograph of the acetone reflux system used to assist removing contamination from quantum particle samples used in this thesis. The acetone in the beaker is just brought to a boil and the sample held on self-closing tweezers is inserted in the opening above the beaker, allowing the sample to sit in the rising acetone vapor. The boiled acetone then distills on the distiller column and runs back into the beaker along the sides of the glass.

If a sample is still found to be contaminated after the acetone reflux and four hours of bake, additional hours of baking time may be added. It has been observed that the amount of contamination decreases with every added hour of bake time, but some samples will not come clean this way. For these very dirty samples a more aggressive cleaning method is needed, called a QP "wash", which was developed by J. Calcines of the Krauss group.

To wash a heavily contaminated sample of QPs, one must remove as much TOPO or other organics as possible. This is achieved by causing the QPs to fall out of the TOPO-rich suspension, separate out the QPs, and resuspend them in a clean solution. The contaminating organics in the sample are all made of long organic chains and are, therefore, essentially hydrophobic. Hexane, chloroform, and toluene, the most commonly-used suspension solvents, are good solvents for these organics but alcohols are not. Therefore, the first step in the wash process is to add 1 mL of butanol to 1.5 mL of concentrated QP dispersion in a centrifuge tube. Then, add methanol until the solution just clouds up and remains cloudy. Centrifuge this mixture at 1700-2100G for 10-15 minutes. The sample should be separated into a pellet of QPs at the tip of the tube and the cloudy supernatent full of organics. The supernatent is removed and the pellet allowed to dry in air. Then, 1 mL of hexane or other solvent is added and the pellet is resuspended. This washing process can be repeated as many times as necessary to remove the organics, however one must be cautious because each wash cycle removes QPs from the sample and also can sift the QP sample to favor keeping larger particles. In addition, these washes can disrupt the relative stasis between the concentration of organics in solution and the surfectant on the QPs. This produces a driving force for the adsorbed organic molecules to come off the QP and go into the solution. This reduced amount of surfectant on the QP can cause it to lose stability upon prolonged storage and ”crash out” of the solution, aggregate and even dissolve. It is best, therefore, to take a sample out of the solution directly after washing and observe the sample in the (S)TEM as a baseline of what the sample should look like. Further samples taken from the washed solution can then be compared to this initial measurement and it can be determined if the sample is aggregating or dissolving or changing in any

observable fashion.

Other methods of cleaning these kinds of samples have been suggested, but not systematically used and tested for efficacy. These include critical point drying and a very quick run of a few seconds in a plasma cleaner. If the sample is in the plasma cleaner for only a few seconds it is unlikely to remove all of the ultrathin carbon substrate, theoretically removing some of the contamination and leaving areas of thinner substrate with the QPs still suspended.

BIBLIOGRAPHY

[1] D.A. Muller, Nature Materials **8**, 263 - 270 (2009).

[2] D.A. Muller, L. Fitting Kourkoutis, M. Murfitt, J.H. Song, H.Y. Hwang, J. Silcox, N. Dellby, O L. Krivanek, Science **319**, 1073-1076 (2008).

[3] K.A. Mkhoyan, P.E. Batson, J. Cha, W.J. Schaff, J. Silcox, Science, **312**, 1354 (2006).

[4] U. Bangert, T. Eberlein, R.R. Nair, R. Jones, M. Gass, A.L. Bleloch, K.S Novoselov, A. Geim, P.R. Briddon, Physica Status Solidi (A) Applications and Materials **205**, 2265-2269 (2008), Hasselt Diamond Workshop 2008 - SBDD XIII.

[5] E.J. Kirkland and M.G. Thomas, Ultramicroscopy **62**, 79 (1995).

[6] E.J. Kirkland, Ultramicroscopy **32**, 349-364 (1990).

[7] D. McMullan, P.J. Fallon, Y. Ito and A.J. McGibbon, Proc. Eurem 92, Electron Microscopy Vol 1, V103 (Granada, Spain) 1992.

[8] D.A. Muller, PhD Thesis, Appendix B, Cornell University, Ithaca NY 1996.

[9] R.F. Loane, E.J. Kirkland and J. Silcox, Acta Cryst. A **44**, 912-927 (1988).

[10] E.J. Kirkland, R.F. Loane and J. Silcox, Ultramicroscopy **23**, 77-96 (1987).

[11] J.P Langmore, J. Wall and M.S. Isaacson, Optik **38**, 335 (1973).

[12] P. Stallknecht and H. Kohl, Ultramicroscopy **66**, 261-275 (1996).

[13] Z.H. Yu, D.A. Muller and J. Silcox, Jour. App. Phys. **95**, 3362 (2004).

[14] H. Ibach, Journ. Elect. Spectrosc. and Rel. Phenom. **64-55**, 819-823 (1993).

[15] R.F. Loane, P. Xu and J. Silcox, Ultramicroscopy **40**, 121 (1992).

[16] S. Hillyard and J. Silcox, Ultramicroscopy **52**, 325 (1993).

[17] R.F. Loane, P. Xu, J. Silcox, Acta. Cryst. **A47**, 267 (1991).

[18] K.A. Mkhoyan, E.J. Kirkland, J. Silcox and E.S. Alldredge, J. Appl. Phys. **96**, 738 (2004).

[19] J.M. Cowley, A.F. Moodie, Acta. Cryst. **10**, 609 (1957).

[20] K. Ishizuka and N. Uyeda, Acta Cryst. A**33**, 740-749 (1977).

[21] K. Ishizuka, Microsc. and Miroanal. **10**, 34-40 (2004).

[22] E.J. Kirkland, *Advanced Computing in Electron Microscopy* (Plenum Press, 1998).

[23] D.A. Muller, B. Edwards, E.J. Kirkland and J. Silcox, Ultramicroscopy **86**, 371-380 (2001).

[24] Z.A. Peng and X. Peng, J. of Am. Chem. Soc. **123**, 183 (2001).

[25] Z.A. Peng and X. Peng, J. of Am. Chem. Soc. **123**, 1389 (2001).

[26] Z.A. Peng and X. Peng, J. of Am. Chem. Soc. **124**, 3343 (2002).

[27] The ultrathin carbon supports used for this study were purchased from Ted Pella: Ultrathin Carbon Film on Holey Carbon Support Film, 400 mesh, Copper, Product No. 01824.

CHAPTER 3

EFFECT OF AMORPHOUS LAYERS ON ADF-STEM IMAGING

3.1 Introduction

Very often layers of amorphous material are present on the surfaces of crystalline specimens prepared for study in conventional TEMs or STEMs. The reasons for the presence of the amorphous layers in these specimens vary. Thin, electron-transparent specimens are often prepared by manual polishing [1, 2, 3] or ion milling [4, 5]. Both methods almost always result in the creation of amorphous layers on the polished/milled surfaces, although the thickness of these layers varies with technique, setup and operator skill. Amorphous carbon films often also serve as supports for specimens such as quantum dots, rods and wires. In some cases specimens are sensitive to electron-beam-induced knock-on damage [6, 7] and are often intentionally covered with a layer of amorphous carbon for protection [6].

The presence of amorphous layers on the surface of a crystalline specimen is expected to have an effect on high-resolution ADF imaging, most likely producing a reduction in contrast. However, it is not clear what the limits are and how exactly the presence of the amorphous layers will effect imaging in the ADF-STEM. It is also not clear what the differences in contrast will be when specimens are imaged with uncorrected probes or aberration-corrected sub-Å probes [8, 9, 10]. Some studies of the effects of an amorphous layer on the probe modification and ADF-STEM imaging have been reported previously [11, 13], wherein primarily uncorrected probes were considered.

This chapter will present an extensive study of the possible effects that amorphous layers may have on high-resolution ADF-STEM image formation and on the visibility of atomic columns [14, 15] using the computational multislice method described previously in Chapter 2.4.

3.2 Multislice ADF-STEM Simulations

The crystalline Si (c-Si) specimen model for the simulations was constructed by locating the electrostatic atomic potentials of Si atoms in the corresponding lattice sites of the diamond crystal. The lattice constant used for Si was a=5.42Å.

The effects of thermal vibrations of the atoms (or phonons) are included in the calculation by randomly displacing atoms from their lattice sites using a Gaussian distribution with the corresponding Debye-Waller factors [17]. The amorphous layers were constructed using c-Si as a starting point and randomly displacing atoms so far from the crystal atomic locations that layers lose all possible periodicities. As a result the amorphous layers have the same density as the crystal layers. Even more realistic models for amorphous Si exist in the literature, but this model is a sufficiently good approximation for this study of electron beam scattering.

All ADF-STEM simulations presented in this paper were performed primarily on Si specimens. The sizes of the Si supercells used in the calculations were: 27.15×26.88Å for the sample oriented along the [110] direction and 27.15×27.15Å and 26.88×26.60Å for the samples along [100] and [111] respectively. The images were obtained by scanning the probe only over a 12×12Å area in the middle of the supercell with 70×70 steps. The following slice thicknesses were used in

all simulations: 1.920Å in the crystals aligned along [110] and 3.135 and 1.357Å for the crystals along [100] and [111] respectively. The inner and outer angles of the ADF detector were 54 and 240 mrads. All calculated ADF intensities are normalized with respect to the incident beam and, because the incident probe intensities in all calculations are kept the same, they are all normalized to the same value. This normalization to a single incident electron is essential for a quantitative comparison of different ADF intensities.

Two STEM probes have been considered for this study. A ≃2Å probe was generated by using the following electron optical parameters: 100 kV acceleration voltage, spherical aberration of C_s=1.3 mm, objective angle of 11.4 mrad, and defocus of 850Å. While these numbers are typical for the Cornell VG-HB501 STEM, they are also comparable to the optical conditions of other STEMs with similar resolutions. A new probe of ≃0.8Å was created using corrections to the axial aberrations: acceleration voltage of 100 kV, $C_{s(3)}$=-0.015 mm, C_5=10 mm, objective angle of 25 mrad, and defocus of -30Å. These are close to the conditions used in Reference [10]. Chromatic aberration is not included in these probe calculations. The profiles of these two probes and corresponding ADF transfer functions are presented in Figure 3.1. Both probes have the same total intensities. The visibility of the atomic columns in pure crystalline Si was also studied experimentally and with multislice simulation by Batson for 120 kV STEM [18].

3.3 Results

Before discussing the effects of the amorphous layers on the surfaces of the crystalline specimens it is critical to address the issue of what is the optimal focus-

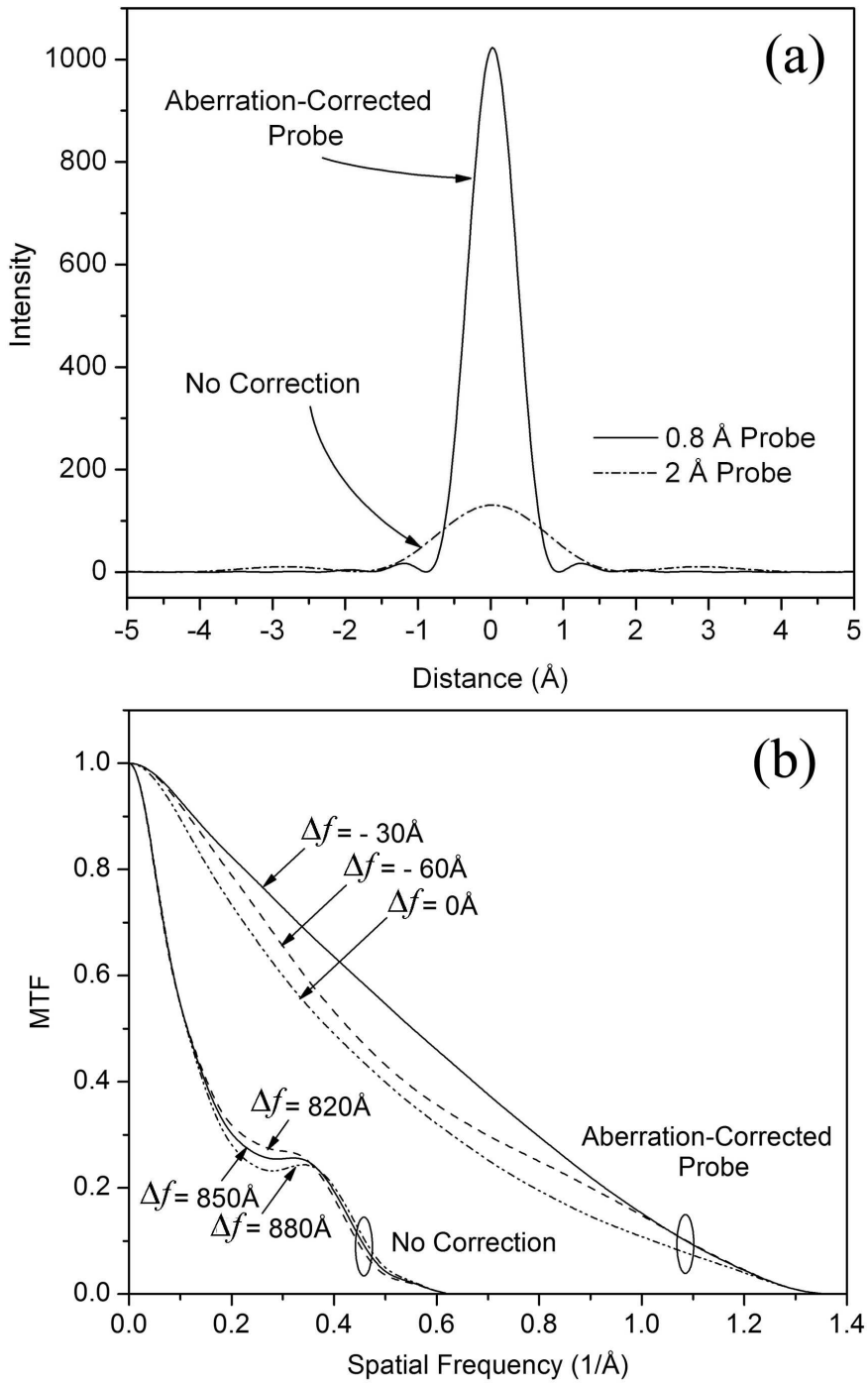

Figure 3.1: Profiles of aberration-corrected and uncorrected STEM probes. (a) Line profiles of two STEM probes: uncorrected 2Å probe and aberration-corrected 0.8Å probe. These two probes are normalized to the same total intensity. The optical parameters used in the calculations are as follows: for non-corrected probe: E_0=100 kV, C_s=1.3 mm, α_{obj}=11.4 mrad, and Δf=850Å, and for aberration-corrected probe: E_0=100 kV, $C_{s(3)}$=-0.015 mm, C_5=10 mm, α_{obj}=25 mrad, and Δf=-30Å. (b) ADF-STEM transfer functions for the two probes in (a) with changes in defocus of ±30Å.

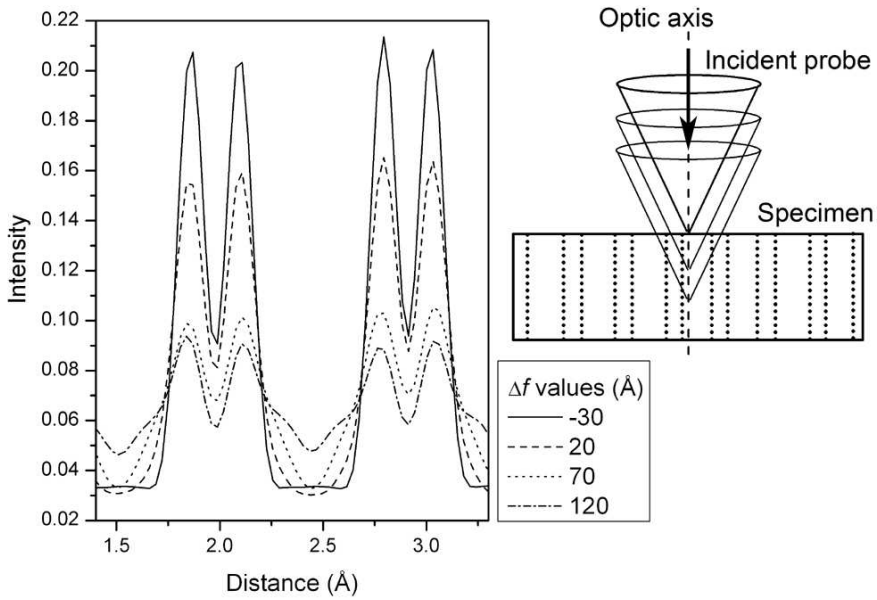

Figure 3.2: Linescans of ADF-STEM images showing Si dumbbell visibility for various defocus values of the probe. ADF intensities are calculated for 300Å thick specimen with a 0.8Å probe where the probe is focused at different depths from the top (entry) surface. The schematic diagram is presented on the right.

ing condition for the STEM probe relative to specimen. To clarify this, several ADF-STEM intensity linescans across Si dumbbells (in [110] projection) were calculated using an aberration-corrected 0.8Å probe by focusing the probe at different depths in the specimen. The results are presented in Figure 3.2. The depth of focus for this probe is estimated to be ≈40Å and, therefore, 50Å steps were chosen in these calculations. As Figure 3.2 shows, the best contrast in ADF images occurs when the probe is focused at the probe entry surface of the specimen. Therefore, in the proceeding section of this paper we discuss the contrast in high-resolution ADF images by focusing the beam on the top surface of the specimen as the optimal condition expected in experimental measurements. It should be noted that slight fluctuations in the intensity values from similar points in these line scans are due to finite sampling of the images during simulation.

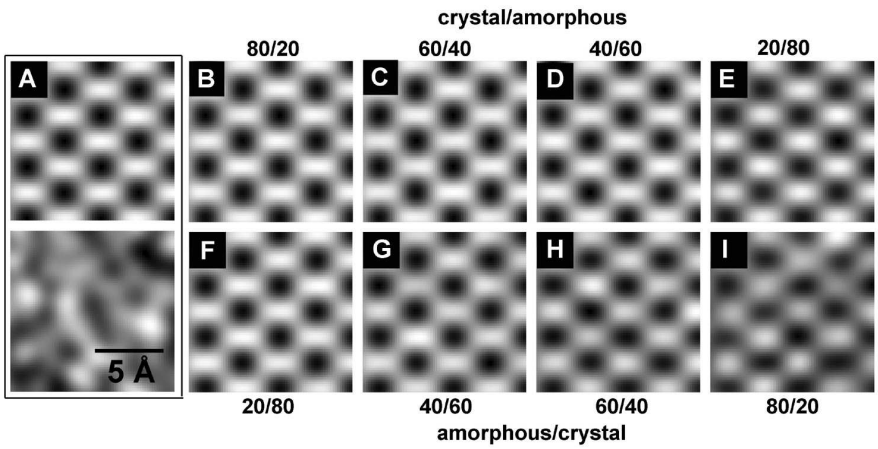

Figure 3.3: Simulated ADF-STEM images of 300Å silicon specimens with different percentages of crystalline and amorphous layers using a probe uncorrected for aberrations. The 2Å probe was oriented along the [110] crystallographic direction. Images in (A) are pure crystalline (top) and pure amorphous (bottom) silicon. Images (B-E) were calculated for 80% crystal and 20% amorphous, then 60% and 40%, 40% and 60%, 20% and 80% specimens. Here the probe propagates through the crystal layer first and then through the amorphous layer. Images (F-I) are calculated similarly to the previous images but the probe enters the amorphous layer first and then the crystal layer. All images are individually scaled to fill the available grayscale.

3.3.1 Uncorrected probe

ADF-STEM images of silicon specimens calculated using the 2Å probe are presented in Figure 3.3. Two cases were considered here: (i) only the probe exit surface of the specimen is covered with an amorphous layer and (ii) only the probe entry surface contains an amorphous layer. While the total thickness of the specimen was kept at 300Å, the proportion of crystal to amorphous layers was varied from 100% crystal to 100% amorphous. Every image in Figure 3.3 is individually scaled to fill the available grayscale as in most displayed experimental images. This often enhances visibility of small features or small contrast in the image.

As expected, even for pure crystalline specimens the individual atomic columns in the dumbbells are not resolved due to insufficient spatial resolution. However, the pairs are quite distinct and their visibility is essentially unaffected by the presence of the amorphous layers. These simulations suggest that when the probe propagates through the crystalline layer first, a sample only 20% crystalline is sufficient to clearly identify the dumbbell units relative to the background (see Figure 3.3 panel (E)). In the case where the probe propagates through the amorphous layer first, the reduction in visibility of the crystal structure becomes apparent when the sample is reduced to 20% crystalline (see Figure 3.3 panel (I)). For quantitative analysis of the visibility of atomic columns in the images, the contrast ξ was calculated using a simple formula:

$$\xi = \frac{I_{max} - I_{min}}{I_{mean}}, \tag{3.1}$$

where I_{max} is the intensity at the position of the atomic column, I_{min} is the intensity between the dumbbells and I_{mean} is the mean intensity of the entire ADF image. This definition of the contrast allows comparison with experimental contrast data which can be deduced from Fourier analysis of the images (the zero spot in the power spectrum of an image corresponds to its mean value). It should be noted that contrast defined in (3.1) describes the visibility of the atomic columns and should not be confused with a more general definition of contrast applicable to any given image. For further discussion of the contrast definition used in this and following chapters, refer to the Appendix in Chaper 3.4.

The contrast values corresponding to the results in Figure 3.3 and calculated for different proportions of crystal and amorphous layers are presented in Figure 3.4. For noise reduction in the data, the values of I_{max} and I_{min} were averaged over many identical locations on the image. It should be noted that since the

contrast of the atomic columns in amorphous material can not be defined, we used the definition of the contrast for crystalline specimens (3.1) and extended it to amorphous material; i.e., the intensities of the same points in the images used to calculate the contrast in the crystal are also used to calculate contrast in amorphous (or partially amorphous) material.

According to the simulations, for STEM with a 2Å probe the crystal structure should be visible in ADF images even when 90% of the specimen is amorphous (see Figure 3.4(b)). The second critical observation is that the visibility of the dumbbells is always higher when the beam propagates through the crystal first.

3.3.2 Aberration-corrected probe

Simulations were also calculated for a STEM with an aberration-corrected 0.8Å probe. While a new probe was generated for these calculations, all other parameters were kept the same as those in the simulations presented in Figure 3.3. The resulting ADF images are presented in Figure 3.5. As expected, for a pure crystalline specimen the 0.8Å STEM probe clearly resolves individual atomic columns of the dumbbell (1.36Å separation). However, unlike the 2Å probe, simulations with the 0.8Å probe show significantly lower visibility of the atomic columns when the beam propagates through the amorphous layer first. Further analysis shows that if the STEM probe is focused not at the sample entry surface but defocused so that the focal point is at the top surface of the crystal layer in the middle of the sample, high-resolution ADF images can still be obtained. Figure 3.5(J-M) shows high-resolution ADF images of the specimen with the amorphous layer at the entry surface when the beam is focused

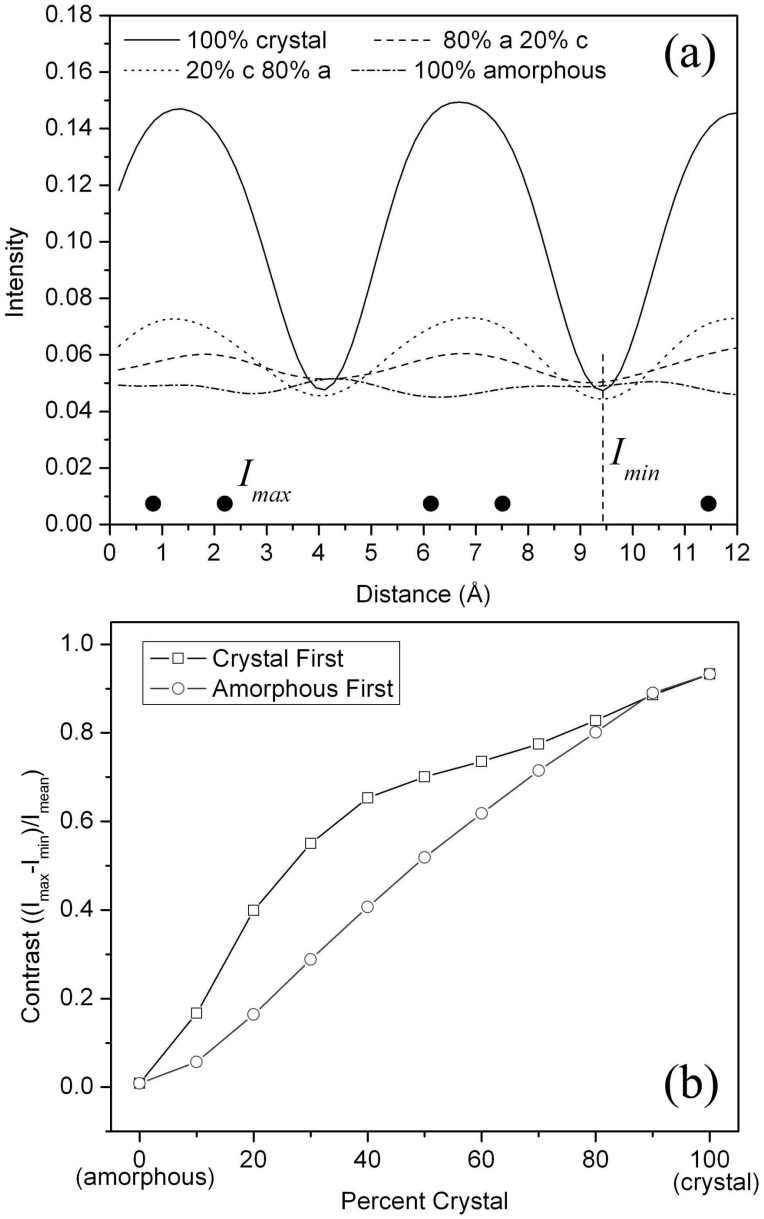

Figure 3.4: Calculated visibility (contrast) of the atomic columns in ADF-STEM images for 300Å-thick silicon specimens using a 2Å probe. The crystalline portion is along the [110] direction. (a) Series of line scans taken from the images presented in panels (A), (E), (I) and (J) of Figure 3.3 along the dumbbells. (b) Calculated contrast as a function of the percentage of amorphous layers for two cases: the beam propagates through the crystal first and the beam propagates through amorphous layers first. The positions of the points whose intensities were used in the calculation of the contrast are indicated in (a).

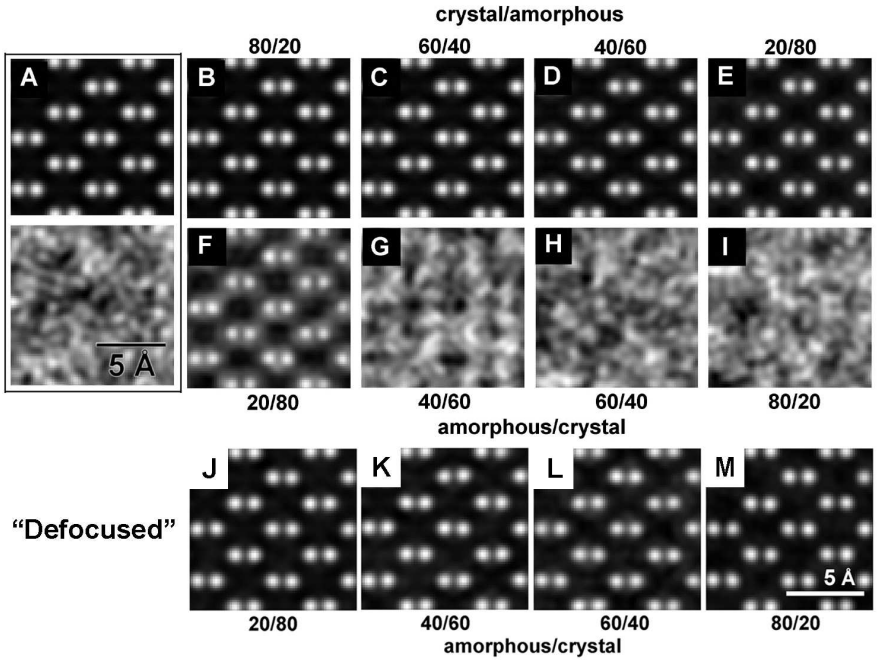

Figure 3.5: Simulated ADF-STEM images of 300Å silicon specimens with different percentages of crystalline and amorphous layers using an aberration-corrected probe. The 0.8Å probe was oriented along the [110] crystallographic direction. Images in (A) are pure crystal (top) and amorphous (bottom) silicon. Images (B-E) were calculated for 80% crystal and 20% amorphous, then 60% and 40%, 40% and 60%, 20% and 80% specimens. Here the probe propagates through the crystal first and then through the amorphous material. Images (F-I) are calculated as in the previous images but the probe enters the amorphous layer first and then the crystalline layers. Images (J-M) are from the same samples as (F-I) correspondingly but now the beam is focused (or "defocused" from the top surface) into the center of the specimen onto the top surface of the crystal layer. All images are individually scaled to fill available grayscale.

on the surface of the crystal layer.

Quantitative analysis of the contrast for this case is presented in Figure 3.6. It shows that when the beam propagates through the crystal first the atomic colums are clearly resolved even for specimens with only 10% crystal. However, when the 0.8Å probe propagates through the amorphous layer first, the contrast is practically zero until the crystal layer is greater than 60% of the total

thickness. This suggests that stronger beam spreading in the amorphous layer takes place when the probe is aberration-corrected. The visibility of the atomic columns in ADF-STEM images using an aberration-corrected probe is expected to have significant gain compared to the conventional 2Å probe: for 60% crystalline specimens $\xi_{0.8} \simeq 2.0$ and $\xi_2 \simeq 0.7$. ADF-STEM images calculated using the 0.8Å probe show that a significant reduction or complete loss of visibility of the atomic columns becomes an issue for concern only in cases where the probe propagates through the amorphous layer first. Experimentally, however, it is unlikely that a microscope operator would choose the top layer of the sample to focus upon, but will instead twiddle the defocus until an optimum image contrast is achieved. This condition is closer to that simulated with the defocus of the probe changed until the beam is focused upon the top of the crystal layer.

For Figures 3.4(b) and 3.6(b), contrast was defined using I_{min} as the intensity between the dumbbells, In Figure 3.6(c), however, I_{min} is redefined as the intensity between the individual columns in the dumbbell itself. This shows that the contrast curves representing the visibility of the columns in the dumbbell closely follow the trend of the general contrast.

Different crystallographic orientations

Since the electron beam is expected to channel along atomic columns differently for different crystallographic directions, a new set of ADF-STEM images was calculated for the same silicon specimen in new orientations. Here specimens with 50% amorphous and 50% crystalline layers were considered. The new Si specimens were modeled with the crystalline portion oriented along the [100] or [111] direction. As before, the total thickness of the specimen was kept at 300Å.

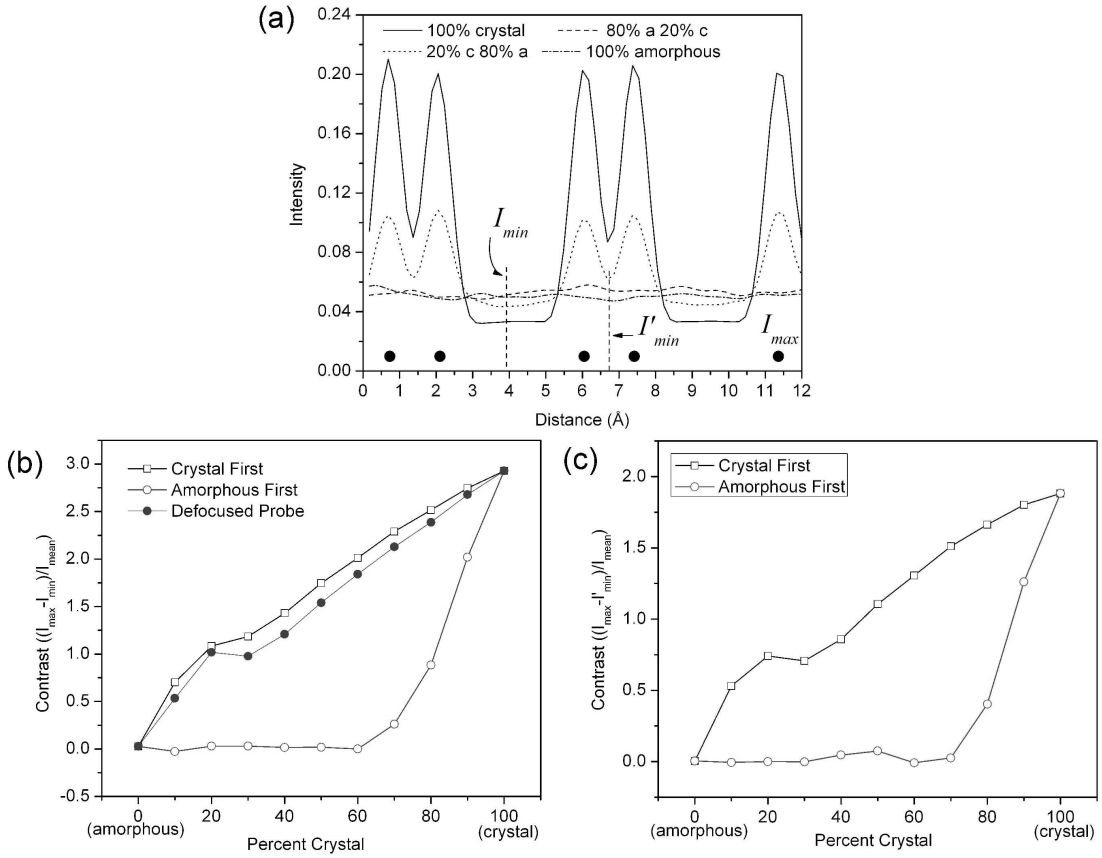

Figure 3.6: Calculated visibility (contrast) of the atomic columns in ADF-STEM images for 300Å-thick silicon specimens using a 0.8Å probe. The crystalline portion is oriented along the [110] direction. (a) Series of line scans along the dumbbells taken from the the images presented in panels (A), (E), (I) and (J) of Figure 3.5. (b) Calculated contrast as a function of percentage of amorphous layers for two cases: the beam propagates through the crystal first and through the amorphous layer first. The values of contrast when the beam is focused (or "defocused" from surface) at the top surface of the crystal layer are also presented. (c) Contrast of atomic column dumbbells calculated using I'_{min} instead of I_{min} in Equation (3.1). The positions of the points whose intensities were used in the calculation of the contrast are indicated in (a).

The results of these simulations are presented in Figure 3.7. It appears that for all three major orientations in Si the general results are the same: the atomic columns are invisible when the beam propagates through the amorphous layer first and is focused on the top of the amorphous layer, and the columns are clearly identifiable when the beam propagates through the crystal first or when the amorphous layer is first and the beam is focused on the top of the crystal surface. The actual numbers for the contrast indicate that for the latter case the visibility of columns grows depending on orientation, from [100] to [111] to [110]. Over a 100% increase in contrast is observed going from a [100] direction to a [110]. Note that the structures of the amorphous Si layers are independent of orientation. As can be seen from Figure 3.7(a) with the amorphous layer first and the beam focused at the top of the crystal layer, the contrast in high-resolution ADF images follows the trend of the crystal-first sample.

Different atomic species

Hillyard and Silcox [26] showed that when the electron beam propagates through two crystals with the same crystal structure and lattice constants but different atom species the beam may channel considerably differently. To study the effects of the atomic number on the visibility of the columns in the presence of an amorphous layer, ADF images were calculated using hypothetical crystals of carbon (C), germanium (Ge), and tin (Sn) using an 0.8Å probe. In these calculations the Si crystal with a =5.42Å was used except all atoms of Si were replaced with atoms of C, Ge and Sn respectively. In the first calculations the probe was focused on the top of the specimen and propagated through the amorphous layer first and then through the crystal since this is the case when

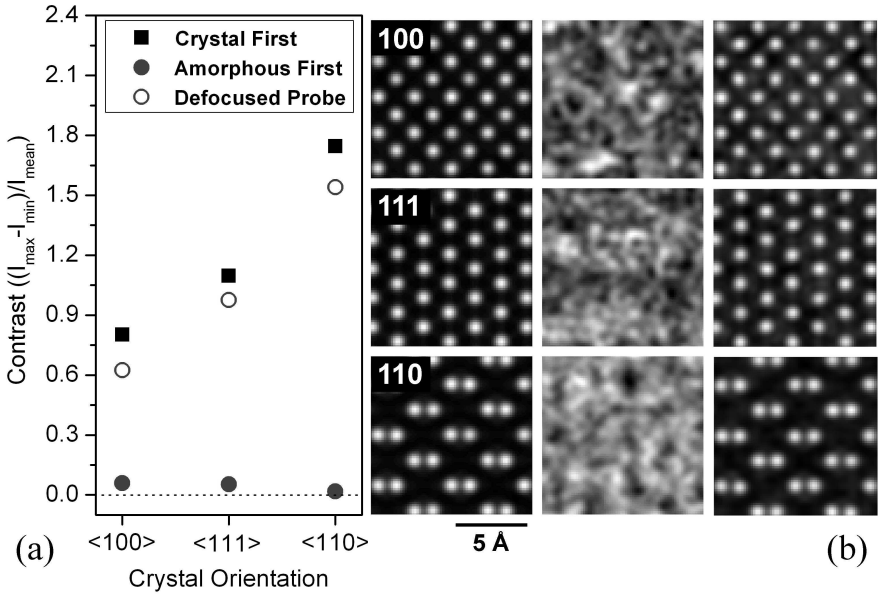

Figure 3.7: Contrast (with simulated ADF images) of amorphous and crystal layers for different crystallographic orientations using an aberration-corrected probe. (a) Calculated contrast in ADF-STEM images of atomic columns in Si specimens with 50% amorphous and 50% crystalline layers for three major crystallographic orientations using a 0.8Å probe. (b) The actual calculated ADF images: left panel - the beam propagates through the crystal first, middle panel - the beam propagates through the amorphous layer first and right panel - the same samples as left panel but now the beam is focused (or ”defocused” from surface) at the top surface of the crystal layer. Orientations of the crystalline layers are indicated in top left corners. All images are individually scaled to fill available grayscale.

imaging the columns appears to be the most challenging. Reference linescans from ADF images of pure crystals of silicon (300Å thick)and the three hypothetical samples are shown in Figure 3.8 (a). As can be seen, I_{min} and I_{max} increase with increasing atomic number with the exception of I_{max} for Sn. The contrast, however, changes in the opposite direction - it decreases with increasing atomic number with C being an exception (see Figure 3.8(b)).

The variations of contrast for atomic columns when calculated with different proportions of crystalline and amorphous layers are presented in Figure 3.8 (b).

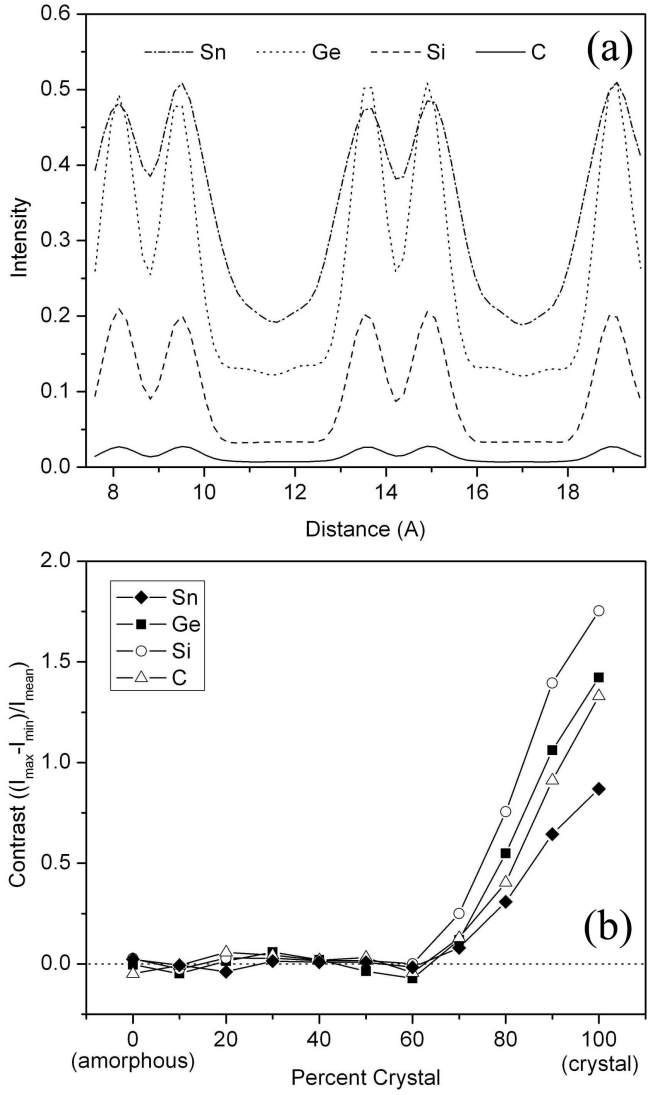

Figure 3.8: Contrast of, and linescans from, simulated ADF images for Si and three different hypothetical crystals of varying Z value. (a) Line scans from ADF images calculated for Si and for three hypothetical crystals constructed by using the lattice structure of Si and lattice sites occupied with C, Ge or Sn. In all cases the line scans are taken across the dumbbells. (b) Calculated contrast for the four 300Å specimens when the beam propagates through the amorphous layer first and the beam is focused on the top of the amorphous layer. Contrast is lost when the amorphous layer is >40% of the total sample, or >120Å. This corresponds to the focal depth of the simulated electron probe and not with any feature of the sample.

Here simulations indicate three critical results: (i) the contrast starts to appear (and the column becomes visible) only when the thickness of the amorphous layer is less than 40% of the total thickness (<120Å) independent of the type of atom, (ii) starting from Si, the contrast of the columns becomes weaker with increasing Z and, finally, (iii) when comparing the results for carbon atoms to those of Si, not only does the entire ADF intensity for carbon drop more dramatically, but also the contrast.

Further calculations were done for the three hypothetical materials when the sample was oriented with the crystal first and also with the amorphous layer first and using a defocused probe so that the probe's focal point was at the top of the crystal layer in the center of the sample. The contrast values for 300Å of sample with 50% crystal and 50% amorphous for both of these arrangements is shown in Figure 3.9. It can be seen that the contrast values for samples in the crsytal-first orientation do not change with increasing Z, but the contrast values go down sharply as Z increases when the amorphous layer is first. This increasing contrast gap between the crystal-first and amorphous-first (defocused probe) orientations is a function of the increased scattering that would occur with heavier atoms, and will be discussed further.

Different specimen thickness

The visibility of the atomic columns in ADF images as a function of the thickness of the specimen is studied by calculating ADF images for Si specimens using the 0.8Å electron probe. Here, specimens with 50% amorphous and 50% crystalline layers were considered. The electron beam was oriented along the [110] crystallographic direction. Specimens were chosen to have a thickness ranging from 50

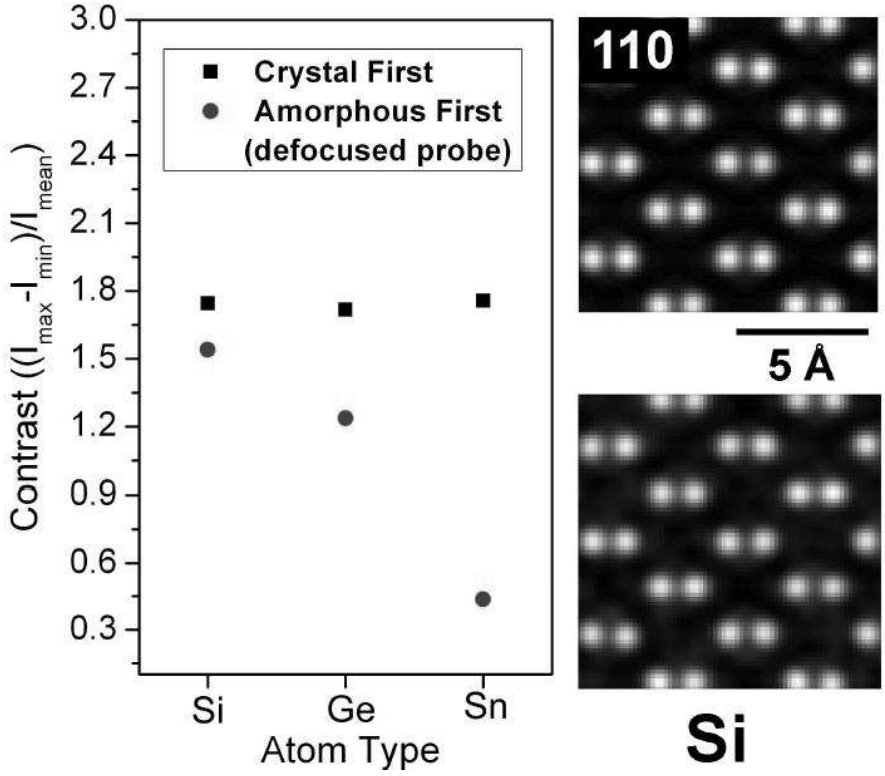

Figure 3.9: (Left) The ADF image contrast values for three different hypothetical materials: Si, Ge and Sn. The crystal structure and lattice constants were those used for Si [110], with only the atomic type changed for each input file. The thickness of each sample is 300Å, with half the sample crystal and half amorphous material. (Right) Simulated ADF images of the Si samples from which contrast values were obtained and presented in the plot: crystal first (top) and amorphous first (bottom).

to 500Å. Simulated images for five different thicknesses are presented in Figure 3.10.

When the electron beam propagates through the crystal first, the visibility of the columns is strong and almost unaffected by an increase in thickness (see Figure 3.10 (a) top row), whereas in cases when the beam propagates through the amorphous layer first the changes are quite significant. Here the columns are visible when the specimen is only 50Å but become completely unresolveable when the thickness is over 150Å (see Figure 3.10 (a) middle row). However, the

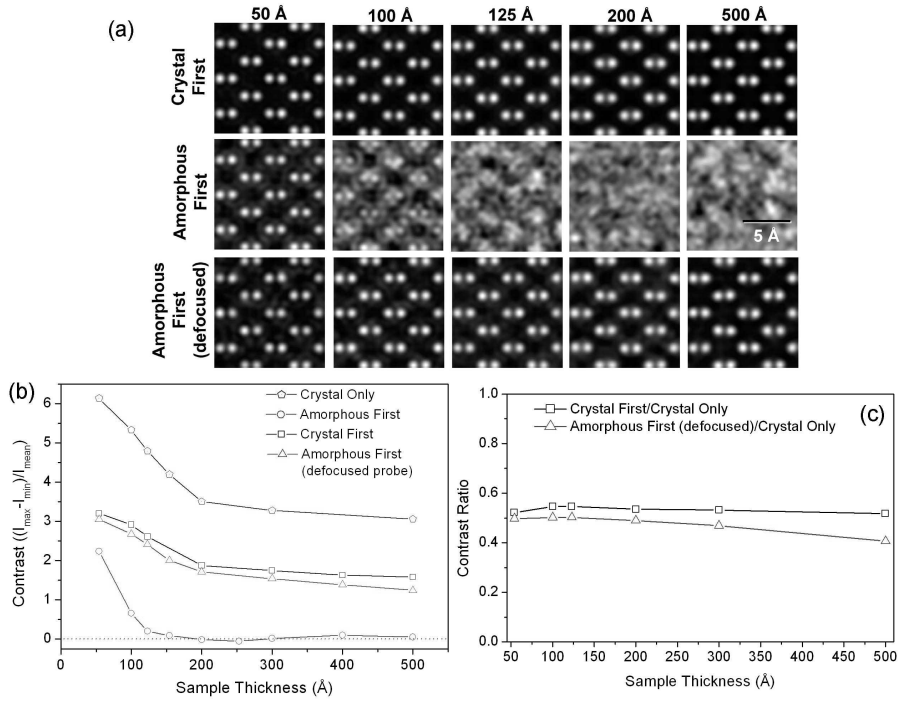

Figure 3.10: Simulated ADF-STEM images of silicon specimens of varying thickness consisting of 50% amorphous and 50% crystalline layers calculated with 0.8Å probe. (a) AF-STEM images where crystals were oriented along the [110] crystallographic direction. Images in the top row were calculated for 50, 100, 150, 200 and 500Å thick specimens when the probe is propagating through the crystalline layer first. Images in the middle row were calculated when probe was propagating through the amorphous layer first, and the images in the bottom row were calculated from the same samples as in middle row correspondingly but with the beam focused (or "defocused" from the sample surface) at the top surface of the crystal layer. All images are individually scaled to fill available grayscale. (b) Calculated contrast of the atomic columns corresponding to the images in (a).

visibility of the atomic columns are restored when incident beam is focused not at the sample entry surface but defocused to a depth inside the specimen where the crystal layer starts (see Figure 3.10 (a) bottom row). The contrast of these images as a function of thickness is calculated using Equation (3.1) and is shown in Figure 3.10 (b).

The contrast of the columns for the situation when the probe propagates

through the crystal first reduces, going from $\xi = 3.2$ for 50 Å specimen to $\xi = 1.80$ for 500 Å. When the beam is focused on the specimen entry surface and propagates through the amorphous layer first the contrast practically disappears for specimens with thicknesses greater than 150 Å. However, when the beam is defocused from the amorphous entry surface and instead focused inside the specimen where crystal layer starts, the contrast is recovered but it is still lower than when beam enters the crystal first.

To see how much contrast is lost by having an amorphous layer on the sample, images of a crystal sample with no amorphous layers were simulated and the contrast of these images as a function of thickness is shown also in Figure 3.10 (b). In this case, the thickness of the crystal sample is consistent with the thickness of the crystal portion only as calculated in the previous three data sets, and therefore is half the value shown on the x-axis of the plot. It can be seen from this data that for a sample with 50% amorphous material, the contrast will always be reduced, and Figure 3.10 (c) shows that the ratio of the contrast reduction is around 50% for all thicknesses.

A more ”practical” study of the contrast reduction due to amorphous layers was done where the thickness of the crystal layer remained constant and an additional amorphous layer of varying thickness was added to the exit surface. This simulation was inspired by the real-life question of how much amorphous material becomes too much amorphous material, where ”too much” is defined as when the contrast value of the ADF images decreases to a level where the lattice becomes indistinguishable or so low of a contrast as to be unusable for material study. Figure 3.11 shows the plots of the contrast of three different crystal layer thicknesses plotted as a function of increasing amorphous layer

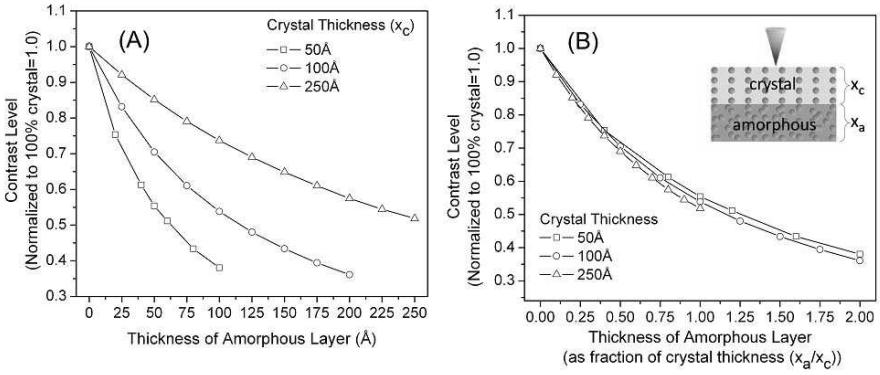

Figure 3.11: The ADF image contrast reduction in Si samples as a function of thickness is shown in two ways in these graphs. (A) shows the contrast level for three set thicknesses of crystal as an amorphous layer is placed on the exit surface and increased in thickness. (B) shows the same data plotted as a fraction of the amorphous thickness, x_a, to the crystal thickness, x_c. The inset in (B) demonstrates the arrangement of the sample with the beam.

thickness. It can be seen that when the contrast is plotted as a function of the ratio of amorphous to crystal amounts the behavior of the contrast decrease is the same for all crystal thicknesses. This particular study was done for the Si crystal only. This kind of plot is a useful one for sample preparers to simulate for their particular sample material in order to discover how sensitive the electron probe will be in their particular case.

3.4 Discussion

The study of amorphous material on crystalline samples has shown that the contrast (visibility) of the atomic columns in ADF-STEM images is always greater when the beam propagates through a crystalline layer first. This holds for both corrected and uncorrected probes. When, however, the probe is focused on an amorphous layer at the probe entry surface, ADF images lose contrast with in-

creasing thickness more quickly with a corrected (0.8 Å) probe than with a uncorrected (2Å) probe.

It was also found that the contrast of the atomic columns in crystalline or partially crystalline specimen is highly sensitive to the crystal structure and the types of the atoms present in the crystal. Finally, the contrast was also found to be strongly dependent on the total specimen thickness.

Before discussing these results in detail the ambiguities arising from the choice of contrast definition should be addressed. At least three different definitions of contrast can be considered. The analysis presented in the Appendix shows that the actual values for the contrast vary from one definition to the next. However, the behavior of the contrast as a function of the amount of amorphous and crystalline layer present in the specimens, or relative contrast, is qualitatively the same.

To understand the poor visibility of the atomic columns in ADF-STEM images due to specimens with an amorphous layer at the surfaces it is essential first to study changes in the incident probe during its propagation through an amorphous layer.

3.4.1 Beam propagation in a-Ge

The effects of the amorphous layer on the STEM probe were studied and calculations for the study were performed on a-Ge samples where a relatively high Z-number ensures strong scattering of the incident beam electrons from the specimen. The parameters of the simulations were kept the same as in the previous

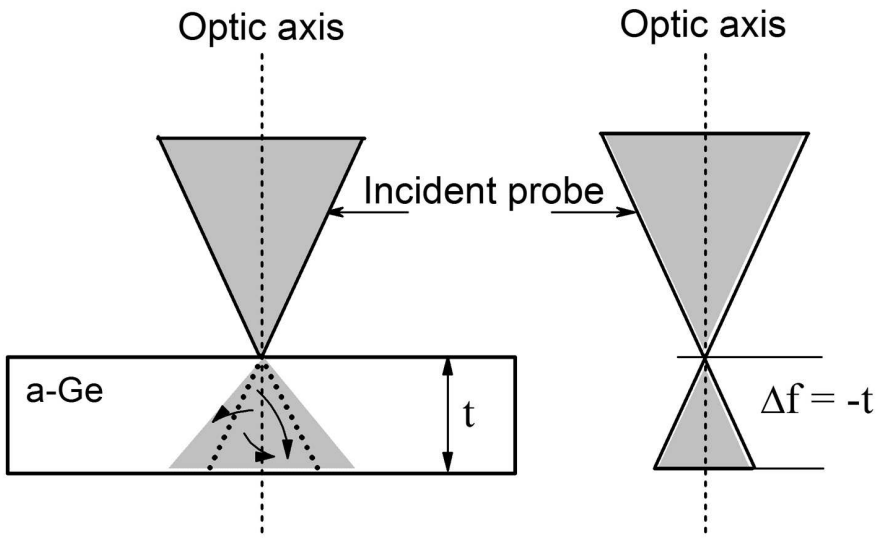

Figure 3.12: A ray diagram of the aberration corrected probe that propagates through a layer of a-Ge of thickness *t* (left), and the same probe that travels the same distance *t* through empty space (right).

simulations carried out for silicon in this chapter. First an aberration-corrected probe of 0.8Å for a 100 kV STEM was generated (see Figure 3.1). This probe was then propagated through a-Ge of different thicknesses. The distribution of the electrons exiting the specimens was obtained in each case in real and reciprocal space. The distribution in real space shows the actual shape of the beam after passing through the amorphous layer. The distribution in reciprocal space (the CBED pattern) describes the angular spread. Simple ray diagrams showing differences between beam propagation through the amorphous layer and through empty space are presented in Figure 3.12.

Figure 3.13(a) shows the shape of the probe after propagating through 150Å of a-Ge, wherein strong broadening of the probe is clear. The corresponding changes in the distribution of probe electrons in reciprocal space is presented in Figure 3.13(b). When the beam passes through the amorphous material a portion of the incident probe electrons do not scatter at all and, after leaving the

material, behave in exactly the same way as the probe electrons that have "additional" defocus equal to the thickness of the specimen (see Figure 3.12). To demonstrate this, a probe with a defocus corresponding to 150Å of amorphous material, $\Delta f_{new} = \Delta f_{old} - 150$Å=-180Å, was also calculated and the resulting intensity destribution is presented in Figure 3.13(c). Similarities between Figure 3.13(a) and Figure 3.13(c) are apparent. To estimate the contributions of the unscattered and scattered electrons to the probe after passing through a thickness, t, of amorphous material, the real and reciprocal space distributions of the probe were examined.

As can be seen from Figure 3.13(b) (see insert) some of the probe electrons during propagation through the a-Ge scatter into large angles and, therefore, cannot be part of the unaltered probe that has traveled a distance t. Other electrons scatter but still stay in the 0-25 mrad angular range of the incident probe. These low-angle-scattered electrons cannot be distinguished from electrons in the original probe and, therefore, they should be considered as part of the unscattered probe.

The number of probe electrons scattered to high angles was calculated by integrating the azimuthally averaged distribution of the intensities in reciprocal space from 0 to 25 mrads before and after the beam is propagated through 150Å of a-Ge and subtracting one from other (see shaded region in Figure 3.13(b) (inset)). Now removing this amount from a new simulated probe with extra defocus, $\Delta f_{new} = -180$Å, the two results were compared in Figure 3.13(d). The difference between the probe propagated through a-Ge and the new, extra-defocused probe (reduced) is a Gaussian-like background. The existence of a Gaussian-like background in the probe, after propagating through an amorphous layer,

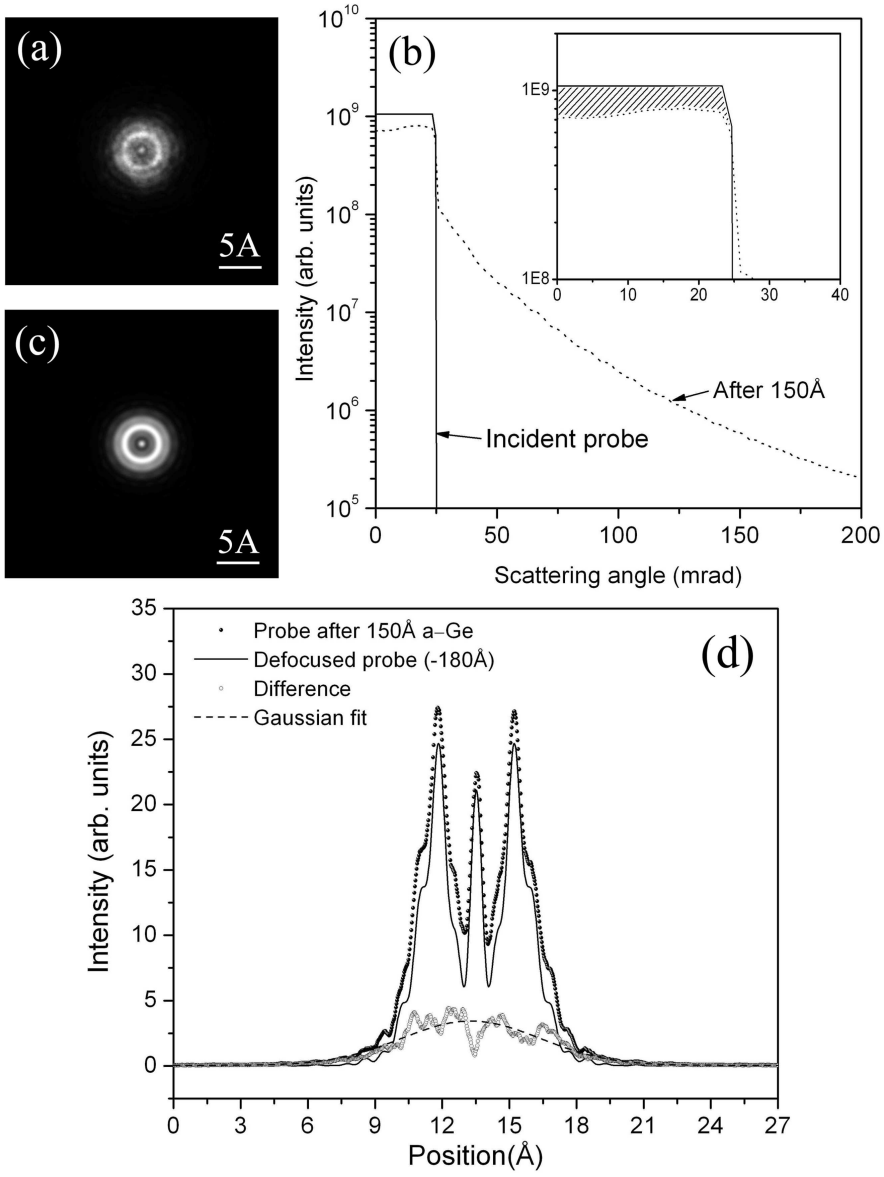

Figure 3.13: Comparison, in real and reciprocal space, of the incident, aberration-corrected probe after traveling through 150Å of a-Ge with that of an identical probe defocused by 150Å. (a) Intensity distribution of 0.8Å incident probe after passing through 150Å of a-Ge. (b) Intensity distribution of the same probe in reciprocal space (azimuthally averaged) together with incident probe. Inset is a close-up of the 0-40 mrad region. (c) New probe calculated using initial probe with additional defocus of $\Delta f = -150$Å. (d) Line-scan of the intensities from (a) and (c) with appropriate reduction and the difference between these two fitted with a Gaussian function.

has been reported previously in the example of InP [11]. Rez [12], using the Boltzmann transport equation to calculate multiple elastic scattering, also predicted Gaussian-like spatial distributions at the exit surface of thin films. The calculation showed the probe changing from a sharply peaked probe (initially a delta function) to a Gaussian-like distribution after scattering through 400nm of Si, 100nm of Fe, and 50nm of Au.

The effect of this Gaussian-like background is best visualized when the probe is propagated through 150Å of a-Ge and is then fitted with a sum of the Gaussian background and the new defocused probe with appropriately reduced intensity. This is presented in Figure 3.14(a). Analysis conducted for the probes propagating through different thicknesses of a-Ge shows a similar result. However, with an increase in the thickness of the amorphous Ge layer the Gausssian background becomes broader. These backgrounds calculated for a probe after 77, 150 and 300Å of a-Ge are presented in Figure 3.14(b). Despite broadening of the peak, the intensity under the Gaussian-like background is higher when thicker amorphous layers are considered. These Gaussian-like backgrounds were analyzed in an attempt to understand the beam broadening inside amorphous materials due to scattering (see inset in Figure 3.14(b)) and plotting the FWHM as a function of amorphous thickness is seen to closely follow the empirical $t^{3/2}$ thickness dependence suggested by Goldstein et al. [27].

The broadening of the Gaussian-like background occurs not only with thickening layers of amorphous material, but also with increasing Z of the amorphous material. As the Z-value becomes higher, the scattering of the beam in the amorphous material increases and the Gaussian-like peak broadens and increases in intensity as more electrons become included in the background and

less in the focused probe. This essentially demonstrates an increased signal-to-noise (SNR) ratio. This increased scattering and SNR is seen in the decreased contrast values of the ADF images as a function of higher Z as shown in Figure 3.9. The contrast values for the amorphous-first orientation (with defocused probe) decrease drastically with higher Z-values, which is exactly what is predicted by the appearance of the Gaussian-like background. When the crystal layer is first, however, no contrast reduction is seen even with higher Z-values. This can be explained by the fact that the images of the crystal lattice are formed before encountering the amorphous layer and, therefore, the probe is unaltered in all three cases of varying Z. The only effect the amorphous layer has when positioned after the crystal layer is to give an overall ”smear” to the image that would be similar in all cases. On the other hand, the probe that forms the crystal lattice image is starkly changed when it encounters the amorphous layer first, and the amount of change to the probe is dependent upon thickness and, as seen in this section, Z value.

The effect of the beam propagation through an amorphous layer of thickness t can be considered as a sum of the partial original probe that has now traveled an extra distance, t, and a Gaussian-like background centered at the position of the incident probe.

3.4.2 Effect of Amorphous Layers on Imaging

The results presented in the previous section showed that after the beam propagates through an amorphous material some of the initial intensity transforms into a Gaussian-like background and the remaining intensity experiences an ad-

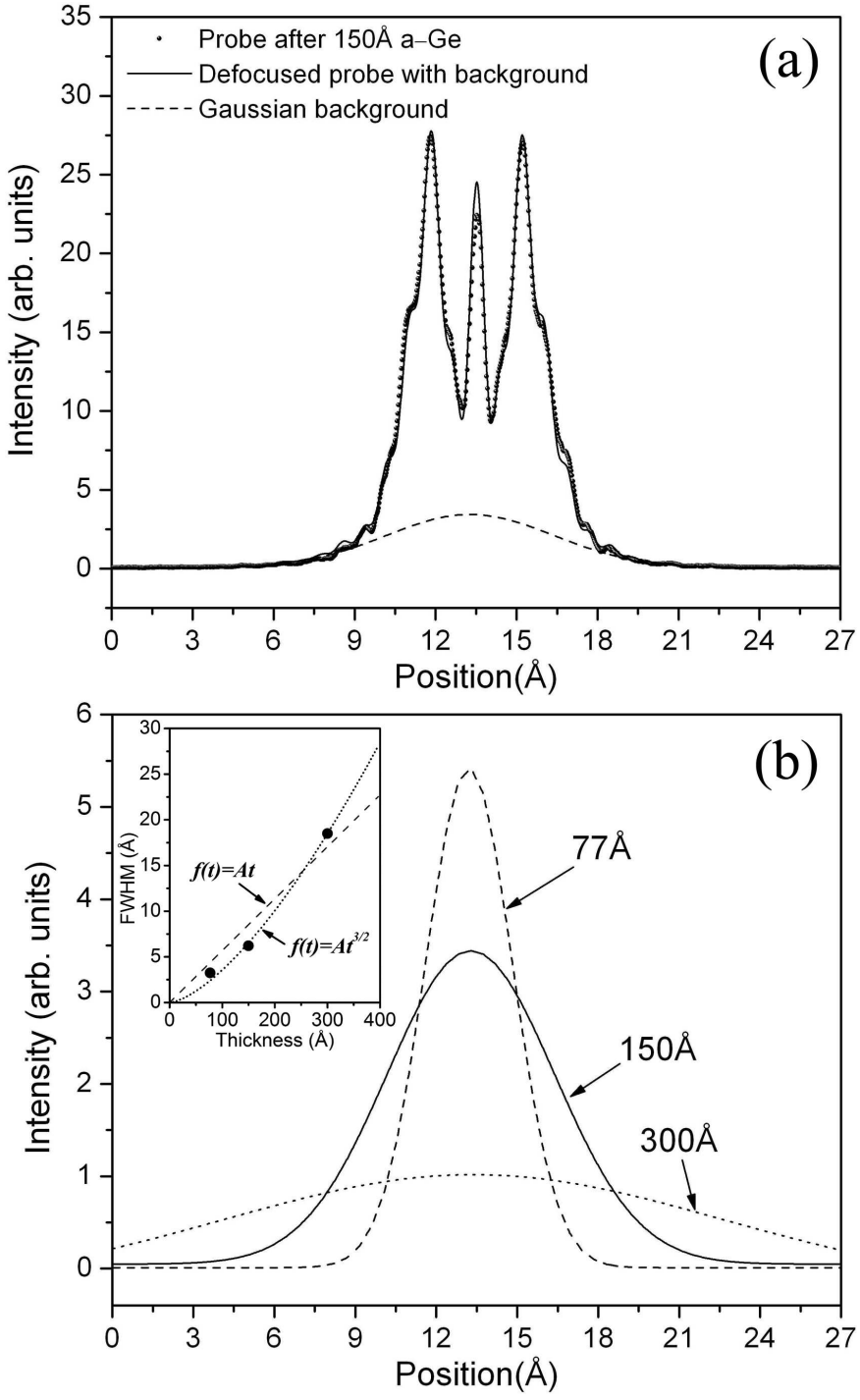

Figure 3.14: (a) Line-scan of the probe after passing through 150Å of a-Ge fit with the sum of a Gaussian background and unscattered probe (reduced probe with extra Δf). The corresponding Gaussian-like background is also plotted. (b) Gaussian-fit backgrounds obtained from a probe propagated through 77, 150 and 300Å a-Ge. The inset shows that FWHM of these Gaussian-fit backgrounds closely follows $t^{3/2}$ thickness dependence.

ditional change of defocus corresponding to a distance t equal to the thickness of the amorphous material. This suggests that the primary reason for the low visibility of the atomic columns with an amorphous layer at the entry surface is the loss of the spatial resolution due to significant beam traveling. This effect, as shown in Figure 3.8 is independent of material in the amorphous layer. Probes with different defocus values corresponding to a beam traveling through different thicknesses of amorphous layers are presented in Figure 3.15. As can be seen, the probe shape degrades dramatically even with changes in Δf value as small as 60Å. The changes in the ADF transfer function corresponding to such variation in defocus are presented in Figure 3.1(b). These results are consistent with observations by Borisevich et al. [28] suggesting a possibility for depth sectioning of amorphous specimens by obtaining through-focal series ADF images using an aberration-corrected STEM.

Calculations of the uncorrected probe with similar changes in defocus (not presented here) show that the shape of the probe changes only very slightly. This weak sensitivity of the 2Å STEM probe to defocus value (visible changes in the probe shape occur only when Δf is changed by $\gtrsim$250Å) explains why, in cases when a 2Å probe is used, changes in the visibility of atomic columns in ADF images are small (see Figure 3.3).

The amounts of the initial probe intensity transformed to a Gaussian-like background are different for different amorphous materials with the same thickness in that heavier atoms in the amorphous layer create a stronger background. However, since the primary alteration of the probe resolution is due to the extra distance traveled (i.e., thickness of the amorphous layer) it is not surprising that complete loss of visibility in C, Si, Ge and Sn samples occurs when the speci-

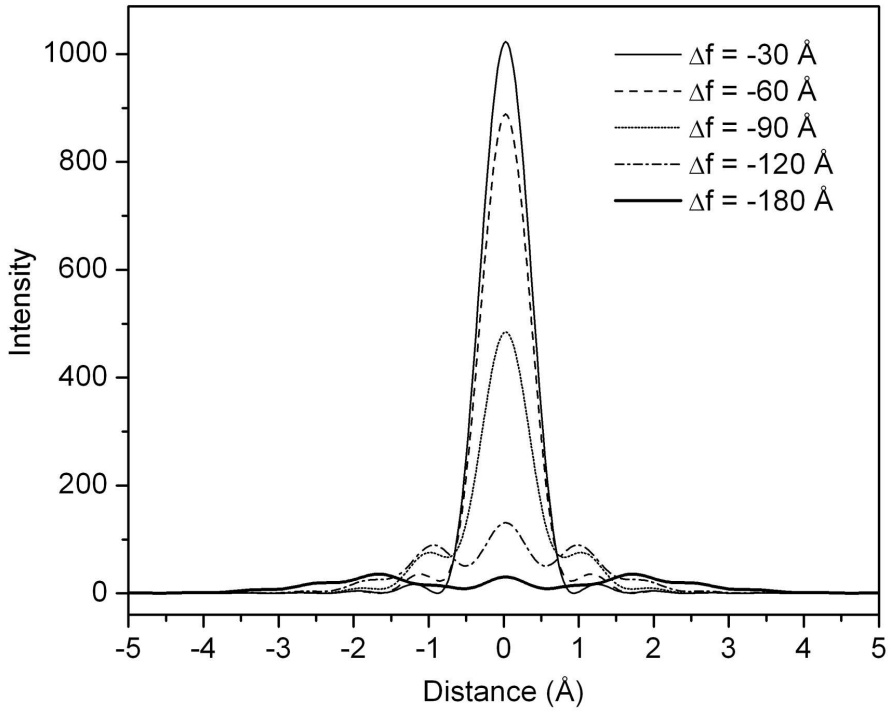

Figure 3.15: Line profiles of the aberration-corrected STEM probe with varying defocus values. These probes are normalized to the same total intensity. The optical parameters used in the calculations were: E_0=100 kV, $C_{s(3)}$=-0.015 mm, C_5=10 mm, α_{obj}=25 mrad, and defocus values are as indicated.

mens have exactly the same thickness of the amorphous layer, t =120Å, at the beam entry surface (see Figure 3.8(b)).

3.4.3 Improving visibility in ADF images in the presence of amorphous layers

The results of section A also provide a solution for improving the visibility of the atomic columns in high-resolution ADF-STEM images. For thin layers of amorphous material only a small portion of the incident beam scatters and becomes background. Therefore, it is possible to defocus the incident probe ini-

tially by such an amount that after it propagates through the amorphous layer it will be properly focused at the desired depth (with a small background from beam scattering). For example, if the beam propagates through 50Å of amorphous material, it is necessary to change the initial defocus value of the probe to $\Delta f_{new} = \Delta f_{old}$+50Å. This kind of adjustment of defocus for optimum imaging is done instinctively by microscope operators who continually twiddle the defocus knob until the image is at its sharpest. There is a limitation in how sharp the image will become, however, because the more amorphous material the beam travels through the more it will scatter, removing electrons from the "signal" of the propagating probe and creating the "noise" of the background. As the signal-to-noise ratio decreases, so does the ability to resolve atom columns in the crystal sample situated beyond the amorphous layers.

The previous calculations of ADF images of Si consisted of 150Å amorphous and 150Å crystalline layers with the 0.8Å STEM probe, and these showed that the ADF images have contrast of $\xi = 0$ (see Figure 3.7). However, when a new incident probe is generated with a defocus value of $\Delta f_{new} = f_{old}$+150Å =120Å, the result is a clear image of the atomic columns. This is illustrated in Figure 3.16. To confirm that a Gaussian-like background is also generated during the process of the probe passing through the amorphous layer, the results are compared with a simulated ADF image of 150Å pure crystalline silicon. As was expected, the contrast of the latter image, $\xi = 3.2$, is more than twice that of the first, $\xi = 1.5$.

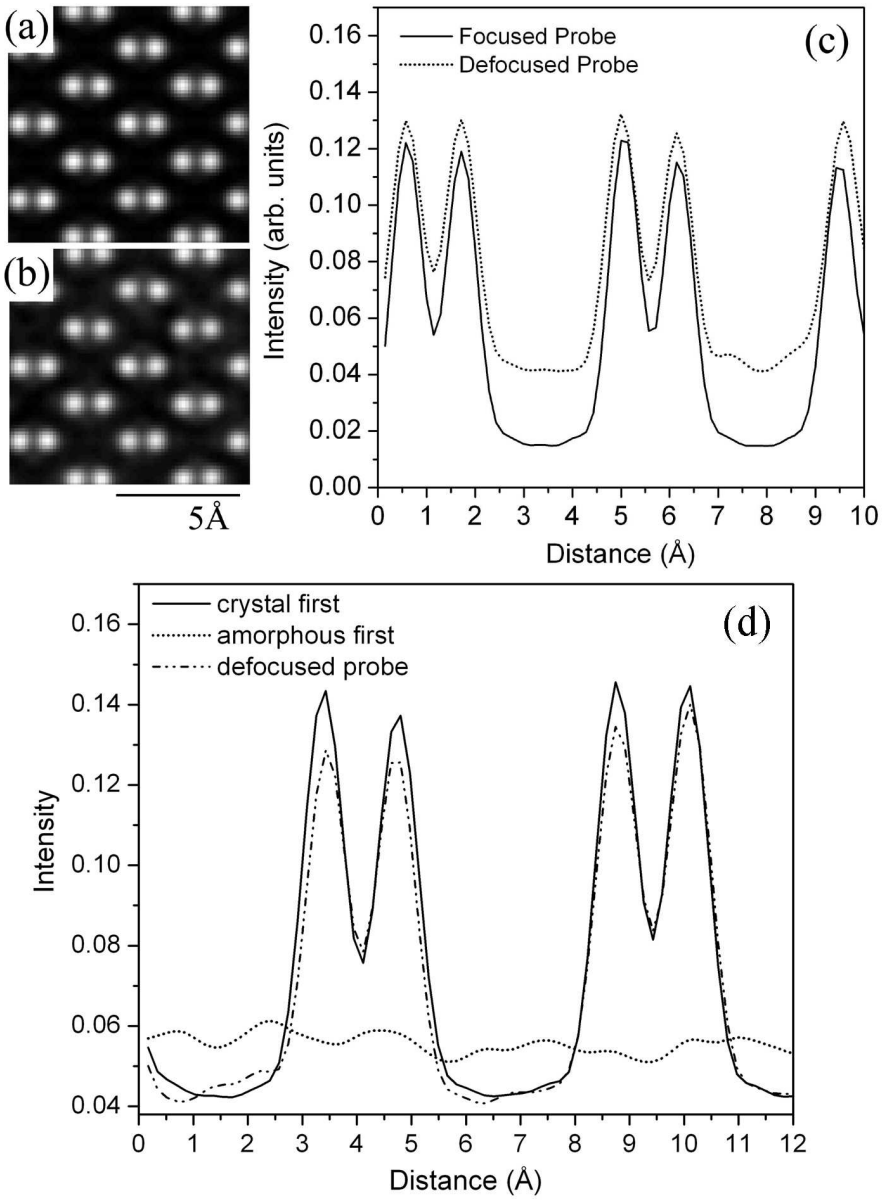

Figure 3.16: Comparison of the distribution of intensity in ADF-STEM images for a purely crystal Si sample and one with amorphous material on top of the crystal layer where the aberration-corrected probe is defocused so that the focal point is located on the top of the crystal layer. (a) ADF image of 150Å of a pure crystalline silicon sample imaged using a 0.8Å probe. (b) ADF image of the silicon specimen consisting of an initial layer of 150Å amorphous and a bottom layer of 150Å crystalline layers, and imaged using a probe with defocus of Δf_{new} =120Å. The images are individually scaled to fill available grayscale. (c) Linescans from the ADF images in (a) and (b). The contrast of the atomic columns in (a) is ξ = 3.2 and in (b) ξ = 1.5. (d) Comparison between linescans from ADF images in (b) and one from specimen with 150Å crystalline and 150Å amorphous layers.

3.5 Conclusions

Study of high-resolution ADF imaging in uncorrected and aberration-corrected STEMs by multislice image simulations shows that the presence of an amorphous layer at the surface of the specimen can significantly alter the visibility of the atomic columns. To achieve the best possible contrast in ADF-STEM imaging it is essential to remove the amorphous layers from both surfaces of the specimen. The reduction in contrast due to the presence of the amorphous layer is strongly dependent upon the thickness of the layer. For aberration-corrected 0.8Å probes, an approximately linear reduction of the contrast (with a slope of 1) is expected with an increase in the thickness of the amorphous layer. Also, an amorphous layer at the beam entry surface effects the image contrast more than a layer at the exit surface. The simulations also show dependence of the image contrast on the crystal structure and orientation and the types of atoms present in the specimen.

Detailed analysis indicates that after propagating through the amorphous layer a portion of the beam passes without any alteration while the rest scatters to larger angles, creating a Gaussian-like background. The portion of the beam that passes without scattering loses spatial resolution due to the additional distance traveled by the beam which ultimately broadens the beam. For an aberration-corrected 0.8Å probe focused on the top surface of the specimen, traveling through 60Å of amorphous material or even empty space is sufficient to lose resolution. After passing through 120Å of amorphous material the beam transforms so dramatically that no atomic columns can be resolved in the crystal layer below. On the other hand, due to the fact that the 2Å uncorrected probe is not very sensitive to the defocus value the presence of the thin ($\lesssim$200Å) layer

of amorphous material should not significantly affect the visibility of the atomic columns. However, lower contrast should be expected.

These results also suggest that, with appropriate changes in defocus value, specimens with amorphous layers can be imaged and high-resolution ADF images with substantial contrast of atomic columns can be obtained. However, compared with a clean (amorphous-free) specimen an additional increase of the background should be expected.

3.6 Appendix

3.6.1 Contrast in ADF-STEM images

The definition of the contrast (or visibility) of atomic columns in images (including ADF-STEM images) has some ambiguity. It can be defined in three different ways:

$$\xi_1 = \frac{I_{max} - I_{min}}{I_{min}}, \tag{3.2}$$

$$\xi_2 = \frac{I_{max} - I_{min}}{I_{mean}}, \tag{3.3}$$

$$\xi_3 = \frac{I_{max} - I_{min}}{(I_{max} + I_{min})/2}. \tag{3.4}$$

Here I_{max} is the intensity of the image at the position of the atomic column, I_{min} is the intensity in between the columns and I_{mean} is the mean intensity of the entire image. All three definitions represent the visibility of the features, in this case the atomic columns, relative to the background. The difference, however, is in the description of the background. Depending upon which definition is used a different value of the contrast can be obtained from the same image.

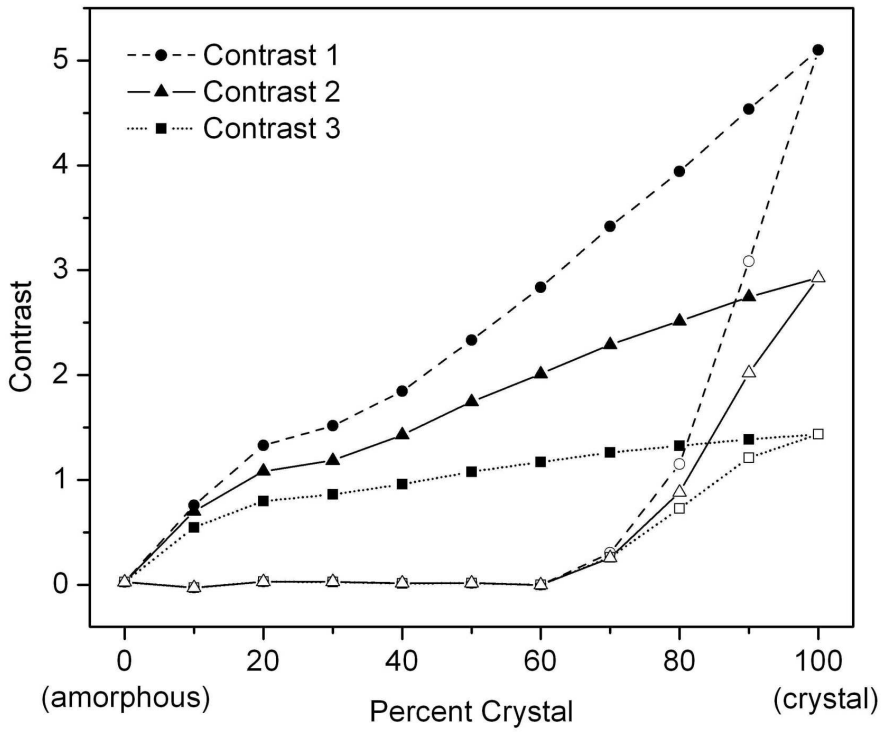

Figure 3.17: Contrast variation of the atomic columns in ADF-STEM images calculated for 300Å thick silicon specimens with a 0.8Å probe using three different definitions of the contrast. The contrast is shown as a function of percentage of amorphous layers for two cases - the beam propagates through the crystal first and through the amorphous layer first. For comparison see Figure 3.6. The crystalline portion is in the [110] orientation.

To show the differences in the values of the contrast for the three definitions (3) - (5), the contrast of the atomic columns in ADF-STEM images was calculated from simulated images generated using an aberration-corrected probe (see Figure 3.5). The results are shown in Figure 3.17. As was expected, the values for the contrast are different with the highest values when the minimum values in the image are considered as the background, as in ξ_1. The difference between contrast definitions ξ_2 and ξ_3, however, depends on the two-dimensional density of the atoms in the imaging plane and on the STEM probe size: as the probe size increases and atomic columns become closer, the values of ξ_2 and ξ_3 approach

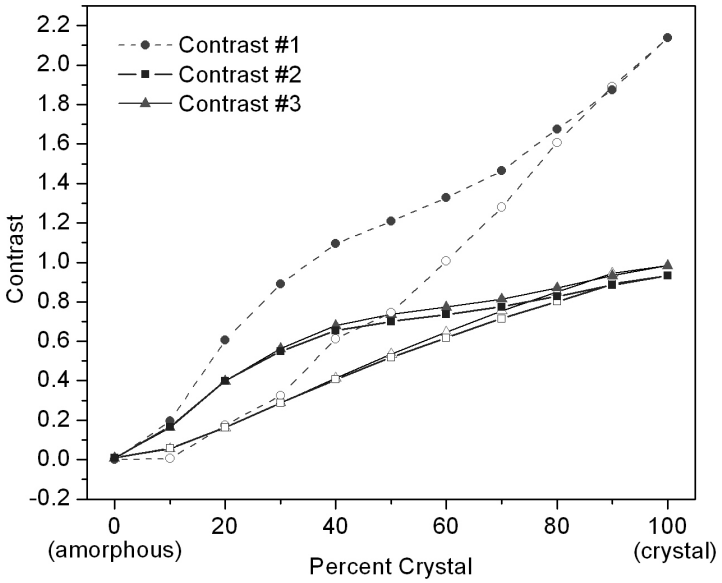

Figure 3.18: Contrast variation of the atomic columns in ADF-STEM images calculated for 300Å thick silicon specimens with a 2Å probe using three different definitions of the contrast. The contrast is shown as a function of percentage of amorphous layers for two cases - the beam propagating through the crystal first and the beam propagating through the amorphous layer first. The crystalline portion is in the [110] orientation.

each other.

As can be seen from Figure 3.17, all three definitions show similar behavior in that the contrast is significantly higher in ADF images created when the beam propagates through the crystal layer first than when the amorphous layer is first. Calculations performed with a 2Å STEM probe shown in Figure 3.18 also show similar results. It appears that for understanding changes in the visibility of the atoms in the ADF-STEM images it is not critical which definition is used.

BIBLIOGRAPHY

[1] J.P. Benedict, R. Anderson, S.J. Klepeis and M. Chaker, Mat. Res. Soc. Symp. Proc. **199**, 189 (1990).

[2] J.P. Benedict, R. Anderson, S.J. Klepeis, in: R. Anderson, B. Tracy, J. Bravman (Eds.), *Specimen Preparation for Transmission Electron Microscopy of Materials II*, Mat. Res. Soc. Vol. 254, Boston, MA, p. 121 (1992).

[3] S.J. Klepeis, J.P. Benedict and R.M. Anderson. In: J.C. Bravman, Editor, *Specimen Preparation for Transmission Electron Microscopy of Materials*, Mat. Res. Soc. Vol. 115, Pittsburgh, PA, p. 179 (1988).

[4] P.J. Goodhew, *Thin Film Preparation for Electron Microscopy,* in Practical Methods in Electron Microscopy, Vol. 11 (Elsevier, 1985).

[5] A. Barna, Mat. Res. Soc. Symp. Proc. **254**, 3 (1992).

[6] D.A. Muller and J. Silcox, Phil. Mag. A. **71**, 1375 (1995).

[7] K.A. Mkhoyan and J. Silcox, Appl. Phys. Lett. **82**, 859 (2003).

[8] P.E. Batson, O.L. Krivanek, N. Dellby, Nature **418**, 617 (2002).

[9] P.D. Nellist, M.F. Chisholm, N. Dellby, O.L. Krivanek, M.F. Murffit, Z.S. Szilagyi, A.R. Lupini, A. Borisevich, W.H. Sides, and S.J. Pennycook, Science **305**, 1741 (2004).

[10] K.A. Mkhoyan, P.E. Batson, J. Cha, W.J. Schaff and J. Silcox, Science **312**, 1354 (2006).

[11] S. Hillyard, Ph.D. Thesis, Cornell University, Ithaca, NY (1995).

[12] P. Rez, Ultramicroscopy **2**, 29-38 (1983).

[13] T. Yamazaki, K. Watanabe, N. Nakanishi and I. Hashimoto, Ultramicroscopy **99**, 125 (2004).

[14] K.A. Mkhoyan, S.E. Maccagnano-Zacher, E.J. Kirkland and J. Silcox, Ultramicroscopy **108**, 791-803 (2008).

[15] S.E. Maccagnano-Zacher, K.A. Mkhoyan and J. Silcox, Quantitative Electron Microscopy for Materials Science, edited by E. Snoeck, R. Dunin-Borkowski, J. Verbeeck, and U. Dahmen (Mater. Res. Soc. Symp. Proc. Volume 1026E, Warrendale, PA, 2007), 1026-C16-02.

[16] J.M. Cowley, A.F. Moodie, Acta. Cryst. **10**, 609 (1957).

[17] R.F. Loane, P. Xu, J. Silcox, Acta. Cryst. **A47**, 267 (1991).

[18] P.E. Batson, Ultramicroscopy **106**, 1104 (2006).

[19] J. Silcox, P. Xu and R.F. Loane, Ultramicroscopy **47**, 173 (1992).

[20] S. Hillyard, R.F. Loane and J. Silcox, Ultramicroscopy **49**, 14 (1993).

[21] D.O. Klenov and S. Stemmer, Ultramicroscopy **106**, 889 (2006).

[22] R.F. Loane, E.J. Kirkland and J. Silcox, Acta. Cryst. **A44**, 912 (1988).

[23] D.A. Muller, B. Edward, E.J. Kirkland, J. Silcox, Ultramicroscopy **86**, 371 (2001).

[24] K.A. Mkhoyan, E.J. Kirkland, J. Silcox and E.S. Alldredge, J. Appl. Phys. **96**, 738 (2004).

[25] E. J. Kirkland, *Advanced Computing in Electron Microscopy* (Plenum Press, 1998).

[26] S. Hillyard and J. Silcox, Mat. Res. Soc. Symp. Proc. **332**, 361 (1994).

[27] J.I. Goldstein, J.L. Costley and C.W. Lorimer, Scanning Electron Microscopy, O. Jahari (Ed), p. 315 (1977).

[28] A. Y. Borisevich, A.R. Lupini and S.J. Pennycook, Proc. Natl. Acad. Sci. **103**, 3044 (2006).

CHAPTER 4

EFFECT OF INELASTIC SCATTERING IN QUANTITATIVE ELECTRON MICROSCOPY

4.1 Introduction

Careful comparisons of experimental transmission electron microscopy (TEM) images with simulated images led Hytch and Stobbs [1] to the conclusion that a problem exists "either in the modeling of the structure or in the electron scattering". This problem manifests itself as reductions of the image contrast by factors of three to five as estimated in that paper and in succeeding work, and this discrepancy between theoretical and experimental contrast has become known as the "Stobbs factor". Since theoretical calculations are very successful in predicting image detail this observation suggests that the coherent electron image intensity is a good deal smaller than anticipated, i.e., the balance between the coherent intensity and the incoherent background in electron scattering processes in thin films is not fully understood. Since then other papers have explored various possibilities that could account for such a large discrepancy without much success [2]. These include the role of amorphous surface layers [3], phonon scattering [4], flexural modes particular to thin films [5], the lack of a "Stobbs factor" in electron interferograms [6] and a search for coherence among inelastically scattered electrons [7]. The origin of the Stobbs factor is an irksome issue, drawing wide attention as a question that must be addressed before electron scattering in these contexts can be considered fully understood. A useful step towards such a goal would be a demonstration of a reasonable accounting of absolute electron intensities in any scattering geometry. Such a benchmark could

provide a basis for further progress with the problem.

Incoherence in electron scattering arises from a wide variety of origins and is typically diffuse in character. In imaging experiments, incoherence is expected to contribute to the background intensity and thus, if omitted in the calculation, to be responsible for the Stobbs factor. The Stobbs factor must be present not only in the images but also in diffraction patterns. Electron diffraction is often carried out using relative intensities [8] to analyze patterns rather than by absolute intensity measurements [9]. In this chapter we report a quantitative comparison of experimental convergent beam electron diffraction (CBED) patterns and associated calculations based on *both* elastic and inelastic scattering of the incident beam electrons in scanning transmission electron microscope (STEM).

4.2 Experimental Measurements

All STEM measurements were done on amorphous silicon specimens prepared by standard cross-sectional tripod polishing and using a commercially available Si [100] wafer with a-Si deposited on the surface. The CBED patterns were recorded using a single-electron-counting yttrium aluminum perovskite (YAP) scintillator-photomultiplier (PMT) system and the dark counts were minimized by appropriately setting the discriminator level. It has been pointed out that saturation of the detector is a problem that could cause spurious results [10]. This has long been recognized by this group as an issue with the detectors and precautions were taken, as are taken whenever CBED patterns are acquired, to avoid saturation. These include taking an image of the zero-disc CBED on the detector when the electron beam is going through a hole and is not hitting the

sample. This intensity level of the beam is reduced with the extraction voltage of the gun until the highest level of intensity seen on the detector is well below the saturation point of 256 counts/pixel. It is easy to tell on these CBED images if such precautions were taken because the linescan of a saturated CBED disc would show a flat top with no noise at all, whereas one that was carefully measured to prevent saturation will have noise all through the measurement and the counts/pixel will be lower than 256. A more pernicious problem than saturation which is not as easily detectable by examining the images is the problem of clipping the lower intensities of the image by injudicious use of the discriminator level, or gain, which was studied by Yu, et al. [11]. This clipping was also carefully avoided in this study.

Figure 4.1 shows several CBED patterns recorded from a-Si at different thicknesses. To emphasize the differences between the patterns they are presented in logarithmic scale. The changes in the actual intensities of the patterns can be measured by taking linescans through the center of these patterns at different thicknesses as presented in Figure 4.1(d). As can be observed from Figure 4.1, as the specimen thickness increases, more and more electrons of the incident probe (central disc) scatter outside the disc thereby reducing the number of the electrons in the original 9-mrad central disc.

For quantitative analysis, the integrated intensities in the original 9 mrad discs were calculated from experimentally measured CBED patterns of the a-Si specimen at various thicknesses. The results were normalized to the incident electron probe, i.e. to the CBED pattern measured with no specimen (see Figure 4.1(a)). This determines the relative reductions of the original intensity. The thickness for each area was estimated from recorded EELS using the ratios of

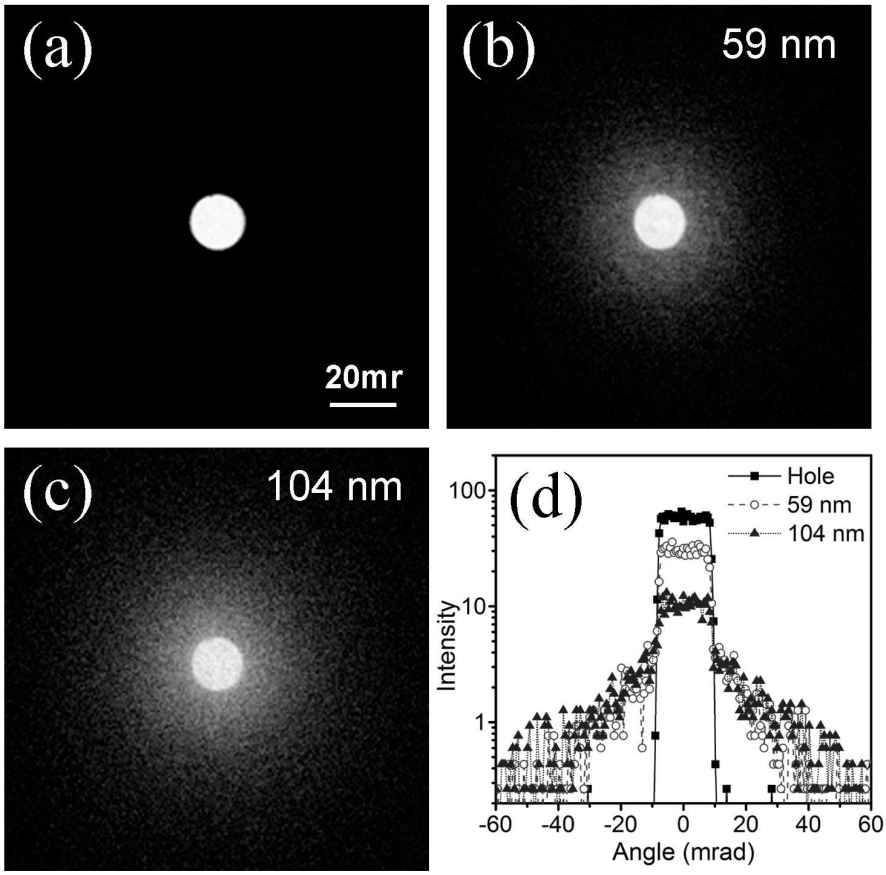

Figure 4.1: CBED patterns measured from a-Si specimen using a 2.1Å STEM probe with a 9 mrad convergent angle: (a) without a specimen, (b) after passing through 59 nm a-Si, and (c) after 104 nm (all in log-scale). The images are in 0(min) - 255(max) grayscale. (d) The actual intensities shown by line-scans taken across the center of the CBED patterns.

the intensities of the single plasmon-loss to the zero-loss: $t=\lambda_{pl}\left[I_{pl}/I_0\right]$, where λ_{pl} is the mean-free path of plasmon generation [12]. The mean-free path of the plasmon generation in a-Si was measured separately using crystalline Si as a reference [13], resulting in $\lambda_{pl}=1.07\lambda_{pl}^{c}=128$nm (for crystalline Si $\lambda_{pl}^{c}=120$nm [14]).

4.3 Theoretical Calculation and Simulation Results

While the formation of these CBED patterns can be described by elastic and inelastic scattering of the fast electrons of the incident beam, in crystalline specimens with periodic arrangements of the atoms and strong diffraction, tracing the history of the incident electrons becomes a complex problem. The set of experiments presented here provides some critical simplifications of the theoretical description of the problem. The first simplification is the use of amorphous material, which allows the assumption of (i) a uniform scattering potential throughout the specimen and (ii) minimal coherent elastic scattering of the electrons following inelastic collisions. The other simplification is (iii) using CBED patterns which allows the analysis to be carried out in reciprocal space. If the thickness of a slice of the specimen, t=Δt, is so small that only the probability of single scattering is significant, the intensity distribution of the beam in reciprocal space after passing through the specimen can be approximated as:

$$\begin{aligned} I(\vec{k}) &= I_0(\vec{k})P_{el}(t,\vec{k})P_{in}(t,\vec{k}) \\ &= I_{el}(\vec{k})P_{in}(t,\vec{k}) \end{aligned} \tag{4.1}$$

where $I_0(\vec{k})$ is the incident beam intensity distribution, $P_{el}(t,\vec{k})$ and $P_{in}(t,\vec{k})$ are the probabilities of elastic and inelastic scattering and $I_{el}(\vec{k})$ is the intensity distribution of elastically scattered electrons. In the present study the CBED patterns produced by multislice simulation are used for $I_{el}(\vec{k})$.

For the final intensity including both elastically and inelastically scattered electrons, the probability for inelastically scattered electrons can be broken into two parts: those electrons in $I(\vec{k})$ that are not scattered inelastically and those

that are. These two situations are shown in the following equation:

$$I(\vec{k}) = I_{el}(\vec{k})\left[(1-\beta) + \otimes B(\vec{k})\beta\right] \tag{4.2}$$

where $\otimes$ denotes convolution, $B(\vec{k})$ (or $B(\vec{\theta})$ using $\lambda\vec{k}=\vec{\theta}$) is the angular cross-section of the single inelastic scattering and β is the probability of a single plasmon generation in the specimen with thickness $t=\Delta t$. The first term in the square brackets of Equation (4.2), $(1-\beta)$, represents the probability of an electron not scattering inelastically where β can described by Poisson statistics [12]:

$$\beta = \frac{\Delta t}{\lambda_{pl}} e^{-\Delta t/\lambda_{pl}}. \tag{4.3}$$

The second term in the square brackets of Equation (4.2) represents the probability of an electron scattering inelastically and the angular distribution of such a scatter calculated using the total cross-section $B(\vec{\theta})=\int_0^\infty dE \frac{\partial^2\sigma}{\partial E \partial \Omega}$. This angular distribution of inelastically scattered electrons is convolved with the angular distribution of intensity of elastically scattered electrons as produced in the multislice CBED images.

For specimens whose thickness is a multiple of Δt, i.e. $t=n\Delta t$, the expression (4.2) modifies to

$$\begin{aligned} I(\vec{k}) &= I_0(\vec{k}) P_{el}(t,\vec{k}) P_{in}(t,\vec{k}) P_{el}(t,\vec{k}) P_{in}(t,\vec{k})... \\ &= I_0(\vec{k})\left[P_{el}(t,\vec{k})\right]^n \left[P_{in}(t,\vec{k})\right]^n \\ &= I_{el}(\vec{k})\left[(1-\beta) + \otimes B(\vec{k})\beta\right]^n . \end{aligned} \tag{4.4}$$

Approximations (i) and (ii) above ensure that once an electron is scattered inelastically, further elastic scattering will be incoherent. Thus, the effects of elastic scattering can be considered independently from the multiple inelastic scattering given by the last factor in Equation (4.4).

The intensity distribution of an incident beam that scatters only elastically while passing through the specimen, $I_{el}(\vec{k})$, can be calculated using the multislice method. The multislice codes of Kirkland [15] have had several successful experimental checks (see e.g. Reference [14]) and serve as the basis for the calculations. In this computational routine, a focused STEM probe is first generated using optical parameters from the experimental set up: 100 kV acceleration voltage, spherical aberration coefficent of C_s=1.3 mm, objective angle of 9 mrad, and defocus of 850Å [16]. The wave function of the STEM probe located at point $\vec{x}_p$ is approximated as:

$$\psi_p(\vec{x}, \vec{x}_p) = A_p \int_0^{k_{max}} e^{-i\chi(\vec{k})-2\pi i\vec{k}\cdot(\vec{x}-\vec{x}_p)} d^2\vec{k}, \tag{4.5}$$

where $\lambda k_{max}=\alpha_{max}$ is the maximum angle allowed by the objective aperture, $\chi(\vec{k})$ is the aberration function and A_p is a normalization constant. In the multislice code the incident electron beam is then propagated through the entire thickness of the specimen by alternately passing through thin layers of the specimen and propagating between the layers. The effects of thermal vibrations of the atoms are included in the calculation by randomly displacing atoms from their sites using a Gaussian distribution with the corresponding Debye-Waller factors [14] and thus also contribute an incoherent component in the diffraction patterns. The CBED pattern is then generated by calculating the intensities of outgoing waves in reciprocal space. An example of a simulated CBED for 109 nm a-Si is shown in Figure 4.2(a).

The amorphous layers of Si for multislice computations were constructed using a model of crystalline Si as a starting point and then displacing atoms randomly from their lattice site until the layers lose all possible periodicities. Amorphousness is confirmed by taking an FFT of the image and checking for

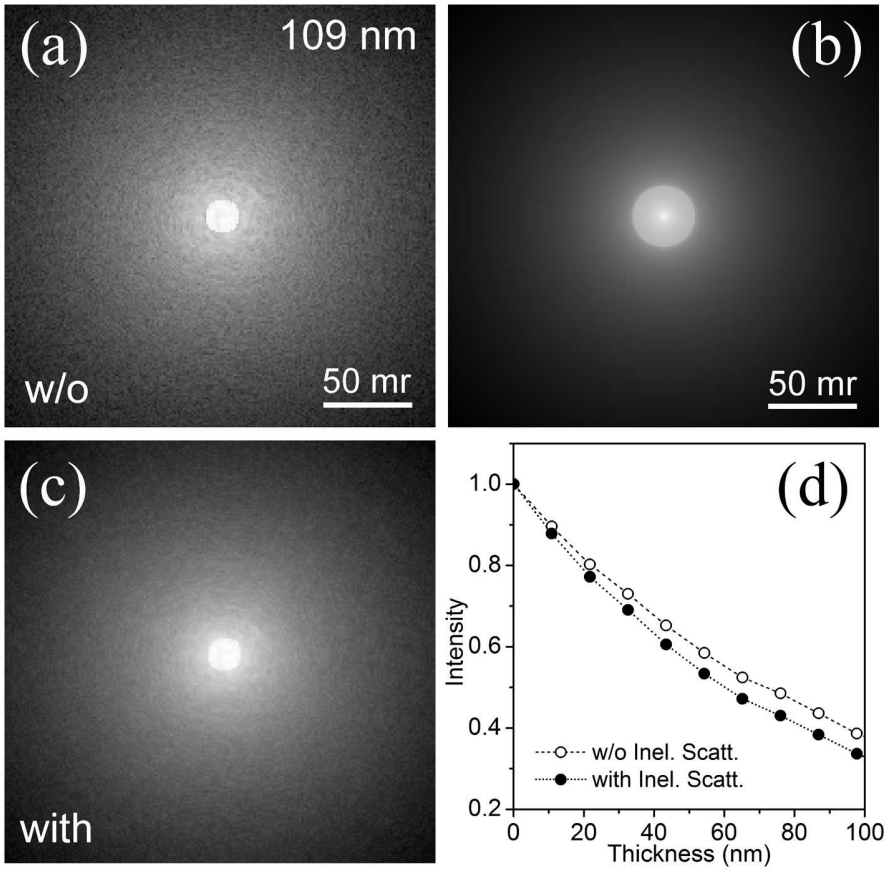

Figure 4.2: CBED patterns calculated for a-Si specimen using a 2.1Å STEM probe with a 9 mrad convergent angle. (a) Intensity distribution of the incident beam, $I_{el}(\vec{\theta})$, after passing through 109 nm thick a-Si calculated using the multislice method where only elastic scattering of the electrons is taken into consideration (including phonons), (b) calculated cross-section of the plasmon generation, $B(\vec{\theta})$, using expression (4.6) with $E_{P,0}$=16.9 eV, ΔE_P=4.0 eV and γ=3.0, (c) the result in (a) after including inelastic scattering, $I(\vec{\theta})$. The images are in log-scale and in 0(min) - 255(max) grayscale. (d) The decrease of the intensity of the beam in the original 9 mrad disc as a function of specimen thickness calculated with and without incorporation of the inelastic scattering.

periodic intensity. The resulting amorphous layers of Si have the same density as the crystal.

To provide a first approximation to the inelastic scattering of the probe electrons the most dominant inelastic scatterer, the plasmon, is considered [17]. The cross-section of single-bulk-plasmon generation by a fast electron that loses energy E and scatters to the angle θ can be expressed as [18, 19]:

$$\frac{\partial^2\sigma}{\partial E\partial\Omega} = \frac{D}{2\pi^2 n a_0}\frac{1}{E_0}\frac{1}{\theta^2+\theta_E^2}\times \frac{E\Delta E_P E_{P,0}^2}{\left[E^2-E_{P,0}^2-4\gamma E_{P,0}E_0(\theta^2+\theta_E^2)\right]^2+E^2\Delta E_P^2} \tag{4.6}$$

where D is the normalization constant, n is the atomic density of the specimen, a_0 is the Bohr radius, E_0 is the incident electron energy, θ_E is the characteristic angle with relativistic correction, $E_{P,0}$ is the plasmon energy at θ=0, ΔE_P is the damping coefficient, and γ is the dispersion coefficient. Also, the plasmon dispersion relation E_P=$E_{P,0}$+$2\gamma E_0(\theta^2+\theta_E^2)$ was taken into consideration. Note that Equation (4.6) also includes single-electron valence excitations [18]. A significant drop of the cross-section with increasing scattering angle is observed. It should be noted that for very thin specimens, typically <10nm, where the bulk plasmon scattering is not the dominant mechanism, the inelastic scattering caused by surface plasmon excitations must be included.

The reduction of the intensities in the 9 mrad zero-discs of the original incident beam at different thicknesses of the a-Si specimen were calculated as follows: first, the elastic scattering of the incident probe electrons for the entire thickness of the specimen was calculated using the multislice method with 1.92Å slices. Next, the inelastic scattering was added via the expression (4.4) with the values for the probabilities of scattering calculated using expressions

(4.6) and (4.3). The separation of elastic and inelastic scattering allows the use of different critical thicknesses for each type of scattering. The thickness of each slice for inelastic scattering was chosen to be $\Delta t = \lambda_{pl}/16 = 8$nm ensuring primarily single inelastic scattering in each layer [20]. This also allows for a more accurate accounting of multiple scattering for the entire thickness of the specimen. These calculations calculate the rate at which the coherent incident electron waves in the probe become incoherent by *both* elastic and inelastic scattering. The only coherent intensity remaining in the problem is that which remains in the incident probe itself. The calculations for 109 nm of a-Si is presented in Figure 4.2(a-c). Some parameters for a-Si were taken from [21]. The reductions of the integrated intensities of the central disc calculated with and without plasmon scattering are presented in Figure 4.2(d). Stronger reduction is observed when inelastic scattering is taken into account. As is to be expected, the effect of incorporating inelastic scattering becomes more and more substantial as the specimen thickens.

4.4 Comparison of Experiment and Theory

When the intensities of the central disc are normalized to the intensity of the original beam outside of the specimen (in vacuum), the reduction of intensity as a function of thickness is readily seen to be independent of the incident beam current. This method, therefore, allows direct comparison of experimentally measured values with theoretical predictions. The results of two independent experiments measured with an 8 mrad convergence angle and 9 mrad convergence angle conducted on different a-Si specimens are presented in Figure 4.3 (a) and (b). The convergent angle of the incident beam was 9 mrad in the first

experiment and 8 mrad in the second, and all other parameters were identical for both experiments. With the smaller convergence angle, a sharper decrease of intensity with thickness is expected since more elastically and/or inelastically scattered probe electrons will scatter outside of the central disc. The results of the corresponding calculations matching both experimental conditions are presented in Figure 4.3 (a) and (b). The discrepancies between experimental data and numerical simulations are analyzed by calculating the divergence of the theoretical results from measured values. The discrepancies for the curves calculated with and without incorporation of inelastic scattering are presented in Figure 4.3 (c). Omitting inelastic scattering from the calculations results in a discrepancy between the model and experiment of about 30%. This discrepancy is the Stobbs factor for the diffraction experiment and is markedly less than that reported for imaging experiments. With incorporation of the inelastic scattering a good correlation is observed with a difference between experiment and theory of $\lesssim$10%. The remaining small discrepancies can be attributed to a combination of factors: not all electronic excitations are considered in the calculations, the inevitable presence of SiO_x on the surfaces of the a-Si and limitations in the calculations due to finite pixelation of the diffraction pattern.

4.5 Conclusions

It is shown that the simplicity of the experimental arrangement of recording CBED patterns through amorphous material combined with single-electron-detection sensitivity of the measurements carried out in STEM provide a direct comparison of experimental data with theory. The results of the comparison identify the critical role of multiple inelastic scattering, approximated by bulk

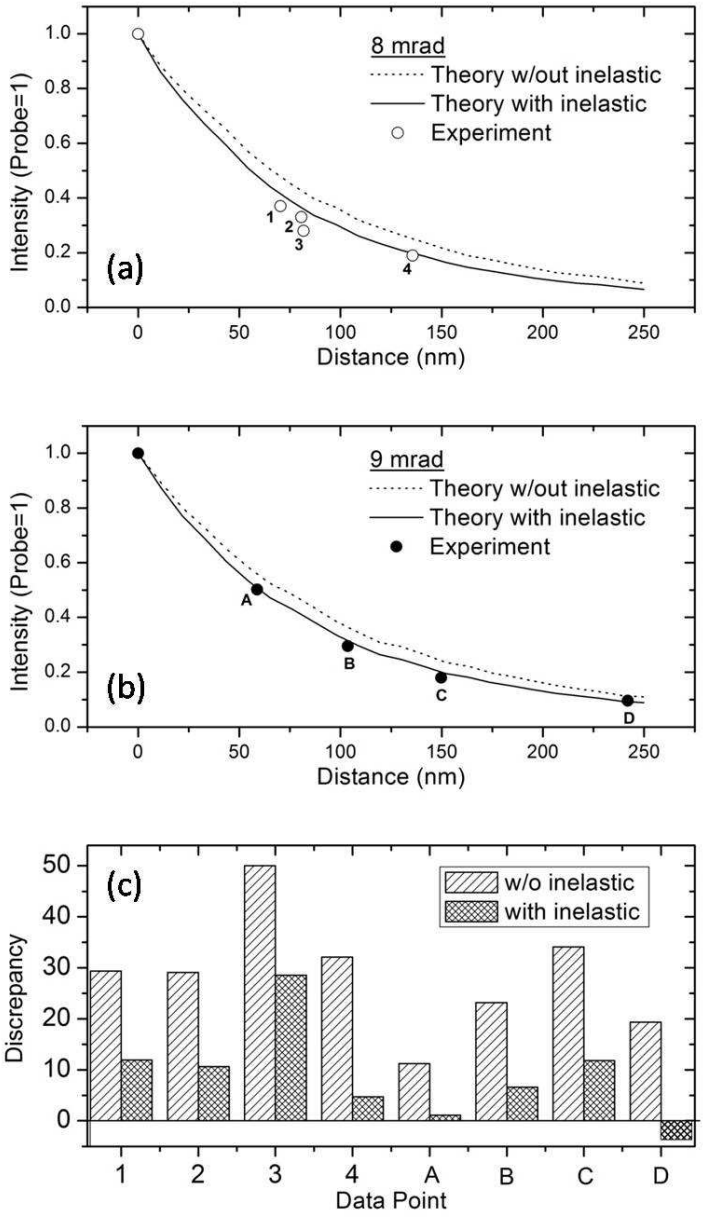

Figure 4.3: (a) and (b) Plots showing the reduction of the intensity in the 8 mrad and 9 mrad central discs of the incident beam with increasing specimen thickness and the theoretical predictions without inelastic scattering (dotted line) and with inelastic scattering (solid line). The results of the two experiments of 8 mrad and 9 mrad were conducted on different a-Si specimens. (c) Analysis of the discrepancies between measurements and theory with and without incorporation of inelastic scattering for both the 8 mrad convergence angle (numbered data points) and the 9 mrad convergence angle (lettered data points).

plasmon scattering, in a quantitative description of the incident beam propagation through electron transparent specimens. Any theoretical diffraction patterns and, therefore, high-resolution images also must contain inelastic scattering for an absolute intensity comparison with experiment.

BIBLIOGRAPHY

[1] M.J. Hytch and W.M. Stobbs, Ultramicroscopy **53**, 191 (1994).

[2] C.B. Boothroyd, J. Microsc. **190**, 99 (1998).

[3] C.B. Boothroyd, R.E. Dunin-Borkowski, W.M. Stobbs, and C J. Humphreys, Mat. Res. Soc. Symp. Proc., **354**, 495 (1995).

[4] C.B. Boothroyd and M. Yeadon, Ultramicroscopy **96**, 361 (2003).

[5] A. Howie, Ultramicroscopy **98**, 73 (2004).

[6] H. Lichte, Phil. Trans. R. Soc. Lond. A **360**, 897 (2002).

[7] R.A. Herring, Ultramicroscopy **106**, 960 (2006).

[8] For example, in a recent paper (J.M. Zuo et al., Science, **300**, 1419 (2003).) the central beam of the electron beam was "obtained from the amplitude of the Fourier transform of a low resolution image".

[9] J.C.H. Spence and J.M. Zuo, *Electron Microdiffraction* (Plenum Press, 1992).

[10] J.M. LeBeau and S. Stemmer, Ultramicroscopy **108**, 1653-1658 (2008).

[11] Z. Yu, P.E. Batson and J. Silcox, Ultramicroscopy **96**, 275-84 (2003).

[12] R. Egerton, *Electron Energy Loss Spectroscopy in the Electron Microscope* (Plenum Press, 1996).

[13] A cross-sectional specimen with side-by-side crystalline and amorphous layers of Si is used. Low-loss EEL spectra were measured in both materials at the same thickness. The mean-free path of plasmon generation can be calculated as $\lambda^a_{pl}=\lambda^c_{pl}\left[I_{pl}/I_0\right]_c\left[I_0/I_{pl}\right]_a$. Several experiments were conducted at different thicknesses to ensure reproducibility of the results.

[14] R.F. Loane, P. Xu and J. Silcox, Acta. Cryst. **A47**, 267 (1991).

[15] E.J. Kirkland, *Advanced Computing in Electron Microscopy* (Plenum Press, 1998).

[16] The electron optical conditions of the STEM were measured on the adjacent crystalline Si sample.

[17] P. Hirsch, A. Howie, R. Nicholson, D.W. Pashley and M.J. Whelan, *Electron Microscopy of Thin Crystals* (Krieger Publishing, 1977).

[18] R.H. Ritchie and A. Howie, Philos. Mag. **36**, 463 (1977).

[19] K.A. Mkhoyan, T. Babinec, S.E. Maccagnano, E.J. Kirkland and J. Silcox, Ultramicroscopy **107**, 345 (2007).

[20] In specimens with thickness $\Delta t=\lambda_{pl}/16$, the ratio of probabilities for single to double plasmon generation, described by Poisson statistics, is $\beta_1/\beta_2=2\left\lfloor\lambda_{pl}/\Delta t\right\rfloor=32$.

[21] H. Raether, in Vol 88 of *Springer Tracts in Modern Physics*, edited by G. Höhler (Springer-Verlag, 1980).

CHAPTER 5

EFFECT OF TILT IN ADF-STEM IMAGES

5.1 Introduction

In (S)TEM experiments a misalignment of the specimens of several milliradians from the targeted zone axis orientation can be present and could go unnoticed. In cases of thin specimens where the tilt is not large (less than a few degrees) high-resolution imaging of the atomic columns is still possible. However, with tilt the channeling of the incident electron beam will be affected and, therefore, some reduction in contrast is expected. Some discussions of the tilt effects on ADF-STEM imaging have been reported previously by a Cornell group [1, 2], Plamann and Hytch [3], Yamazaki et al. [4] and Wang et al. [5].

In an earlier paper Yu et al. [2] reported experimentally recorded ADF images of Si specimens at high-angle tilt using 200 kV, uncorrected STEM and compared them with multislice simulations. The primary point of that paper was to record the serious drop in intensity within a couple of degrees or so away from zone axis. In this chapter we explore the effects of even smaller specimen tilts on high-resolution ADF-STEM imaging with an emphasis on the visibility of the atomic columns, i.e., contrast, also using a computational multislice method described in Chapter 3.1.1 of this thesis and also previously in literature [6].

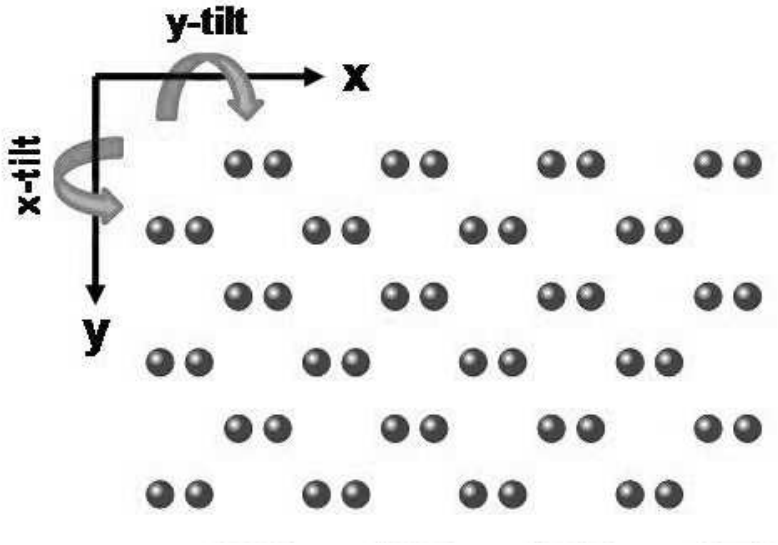

Figure 5.1: Schematic diagram describing tilt axes and directions used here relative to a Si crystal oriented along the [110] crystallographic direction.

5.2 Multislice ADF-STEM Simulations

All of the ADF-STEM image simulations presented in this paper used Si crystal test specimens. The sizes of the Si supercells and the slice thicknesses used in the calculations were the same as those used and reported in Chapter 3.1. The images were obtained by scanning the probe over an 11×8Å^2 area in the center of the supercell with 65×47 pixels. In simulations the x and y tilts of the crystal were introduced by rotating the crystal around the y and x axes respectively. The diagram of the x-y geometry of the Si crystal when it is oriented along the [110] orientation is presented in Figure 5.1. The details of the introduction of the tilt in multislice can be found in Reference [7].

The two STEM probes considered in this study were the same as used and reported in Chapter 3.1, and the probe profiles are shown therein. In all simulations the beam was focused on the entry surface of the specimen [8].

Though in some standard definitions of contrast an ADF image of amorphous material would have a contrast value, the image would not have any lattice fringes or periodic intensity indicating the presence of a crystalline structure. Since this study is concerned with quantifying the visibility of the crystal lattice in an image, the following definition for contrast was chosen so that its value will be near zero when there is no visibility of atomic columns in the image [8]:

$$C = \frac{I_{max} - I_{min}}{I_{mean}}, \tag{5.1}$$

where I_{max} is the intensity at the position of the atomic column, I_{min} is the intensity between the dumbbells and I_{mean} is the mean intensity of the entire ADF image. This is the same definition as used in Chapter 3, and for a discussion of various contrast definitions and their plots, see the Appendix in Chapter 3.5.1.

5.3 Results

First, images of the crystal lattice of Si tilted about the [110] crystallographic orientation were simulated using a 2Å probe. The crystal was tilted in 3 mrad steps around the x- and the y-axes (see Figure 5.1). The crystal thickness in these calculations was 250Å. An array of these images is shown in Figure 5.2(a). Each image in the array is normalized to the incident beam, so the decrease in intensity of the atomic columns is more readily perceived. This decrease of intensity of Si atomic columns in high-angle ADF (HAADF) detectors for a ≃2Å probe has been also noted by Yu et al. [2]. Figure 5.2(a) is similar to what a microscope operator would observe if they were lucky enough to find a variation of tilt of one degree within the microscope field-of-view and reflects the intensity mea-

surements found experimentally by Yu et al. [2]. In comparison, Figure 5.2(b) shows the same simulated data reflected in Figure 5.2(a), but now the images in this figure are individually rescaled to available the grayscale internal to each image. This illustrates the change in appearance of the crystal lattice viewed by the microscope operator as they move about and image the sample at different locations. In this case, for lattice images, changes in appearance of the lattice images and not intensity will be the first indication that the sample has tilted from on-axis orientation. It is interesting to note from Figure 5.2(b) that even with a relatively large tilt of 15 mrad in x and y, the crystal lattice is still visible. In Figure 5.2(b) the images with large single-axis tilt show an increase in the separation of the bright spots which may seem to indicate increased resolution but in reality it is a degradation in the imaging the dumbbell columns due to distortion from the tilt. At a more conservative tilt of 12 mrad in x and y, the crystal lattice image is one that appears to be "on axis" even though it is actually over 2/3 of a degree off the [110] axis in both the x- and y-axes As mentioned previously, the images in Figure 5.2(b) are scaled to fill the available grayscale and, therefore, for quantitative analysis the actual values of the ADF intensities are required. Figure 5.3 shows the line scans across the simulated images whose intensities have not been rescaled. These line scans show a decrease of the highest intensity on the atom columns with increased tilt of the crystal, and very little change of the low intensity between the columns.

The values of the contrast (5.1) are also calculated for each image and the results are plotted in Figure 5.4. The graph shows that the contrast decreases by about 60% and 30% when the crystal is tilted 15 mrad along the y-axis and x-axis. The maximum contrast reduction for a 15 mrad tilt angle occurs when only the y-axis is tilted. The contrast reduction seems to have some unexpected

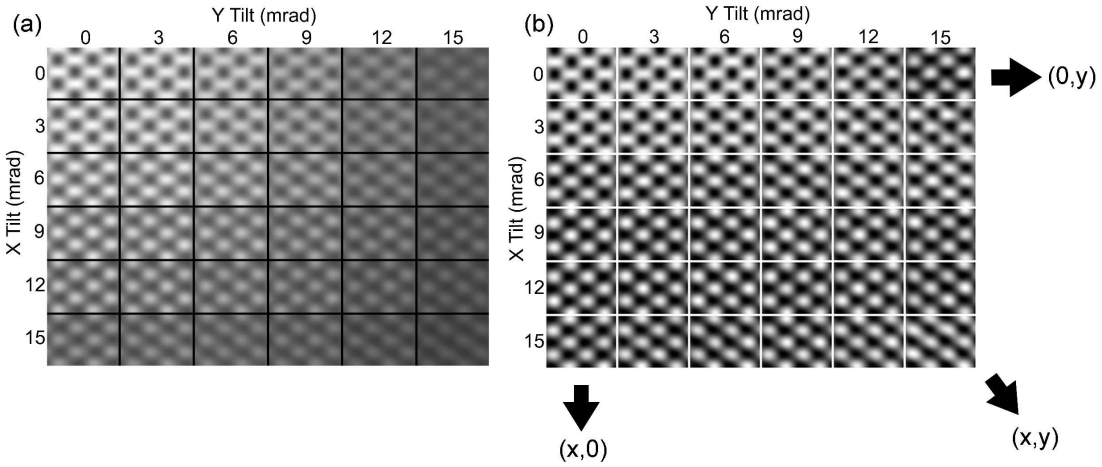

Figure 5.2: Simulated ADF-STEM images of 250Å thick crystal silicon specimens at different tilts using a probe uncorrected for aberrations. A 2Å probe was used and the crystal was tilted around the [110] crystallographic orientation.The specimen tilt angles along x- and y-axes are indicated. (a) All images are normalized to the incident beam. (b) All images are scaled to fill the available grayscale. Arrows alongside the array in (b) demonstrate the direction for each tilt in the array, with images in rows increasing in y-tilt, (0,y), images in columns increasing in x-tilt, (x,0), and the diagonal having equal tilt in x and y, (x,y). This scheme is used for all tilt image arrays in this chapter. For both image (a) and (b), spots of bright intensity indicate location of atomic dumbbells and scale bars are 5Å.

oscillatory behavior as the tilt increases. Figure 5.4 shows that as the sample is tilted from the [110] orientation the contrast of the image reduces by a factor of two despite visibility of the atomic columns in the image.

ADF images of the same Si crystal were also simulated using an aberration-corrected 0.8Å probe. Here again 3 mrad tilt steps were used around the x- and y-axes. The resulting array of the ADF images is shown in Figure 5.5. Similar to the case with 2Å probe, the crystal lattice is visible throughout the tilt series. With the smaller probe there is very little discernible difference between the on-axis case and the largest tilt case. This was also observed experimentally by Wang et al. [5]. Linescans from several of these images showing the actual

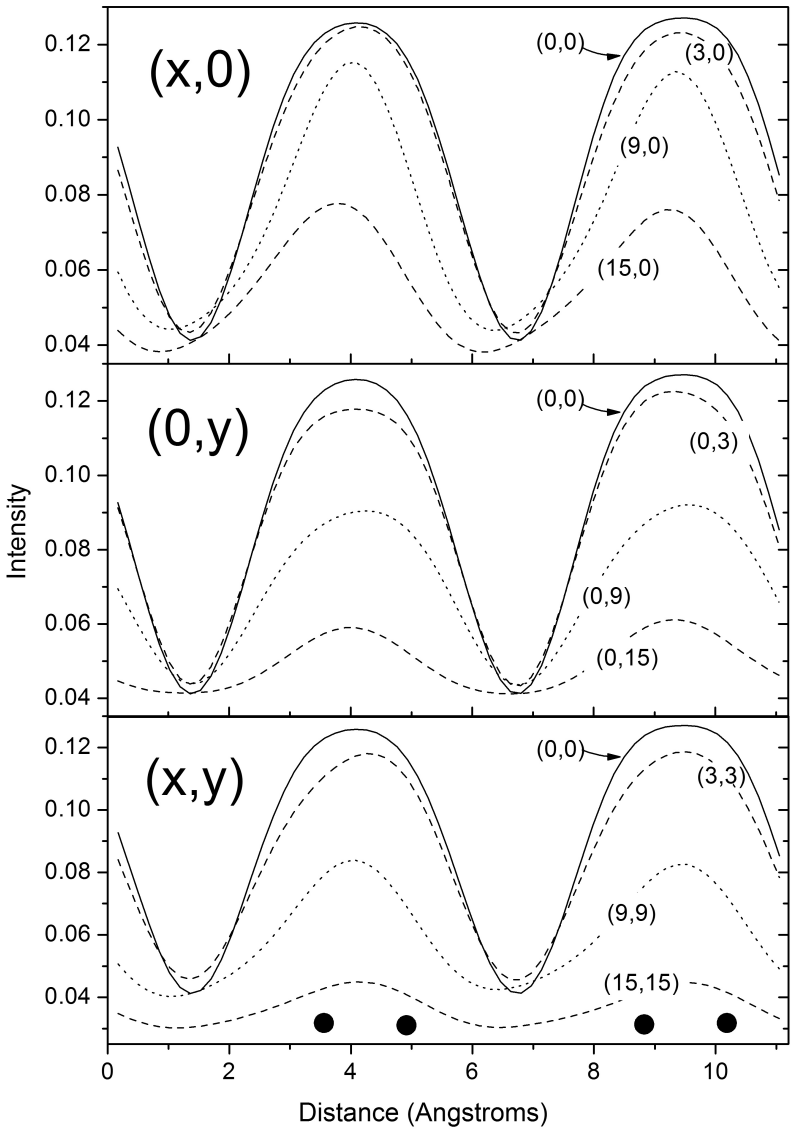

Figure 5.3: Line scans from simulated ADF-STEM images of Si oriented along the [110] direction at different tilt angles calculated using a 2Å probe and taken across the dumbbells. The tilt angles are given in brackets (x,y). The upper plots show tilts in x, (x,0), the middle plot shows tilts in y, (0,y), and the lower plot shows equal tilts in both x and y, (x,y). The positions of atomic columns are indicated with black dots.

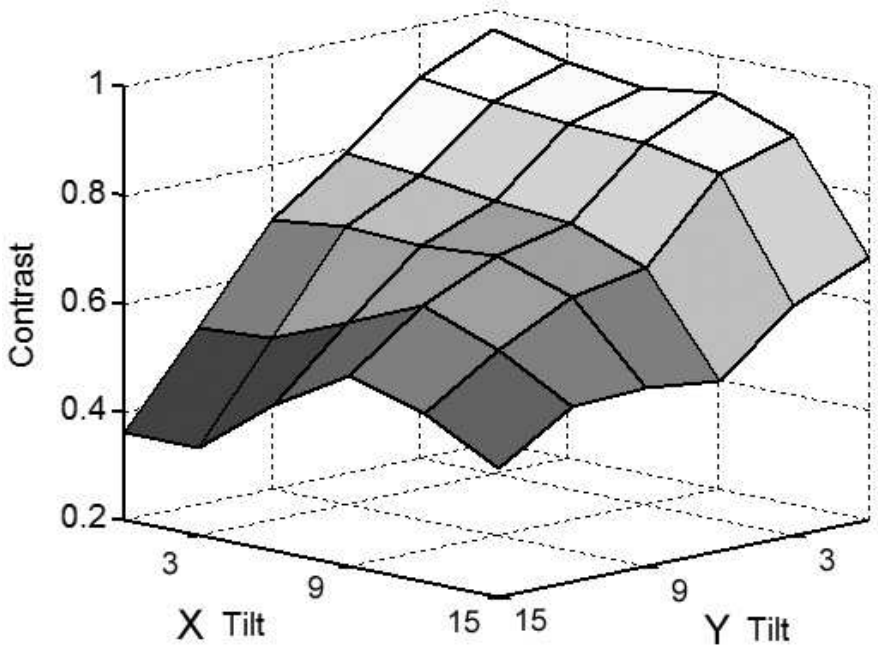

Figure 5.4: The values of the contrast calculated from ADF-STEM images of a Si specimen simulated at different tilt angles around the [110] crystallographic orientation with a 2Å probe.

values of the ADF intensities are presented in Figure 5.6. The intensity of the bright spots, whose locations correspond to the positions of the atomic columns in an untilted crystal, is seen to decrease significantly as the tilt increases, decreasing to over half its value with a 15 mrad tilt in both axes. And again, as in the uncorrected probe case, the low intensity between the atomic columns does not change discernibly. The contrast values for all tilts are also calculated and the results are plotted in Figure 5.7. This graph shows a much more regular reduction of contrast with an increase of tilt than the uncorrected probe, exhibiting no oscillations in contrast but instead reducing monotonically as the tilt increases. The highest tilt (15,15) creates an image with contrast almost half that of the untilted image.

The visibility of the atomic columns in the ADF images is sensitive to the

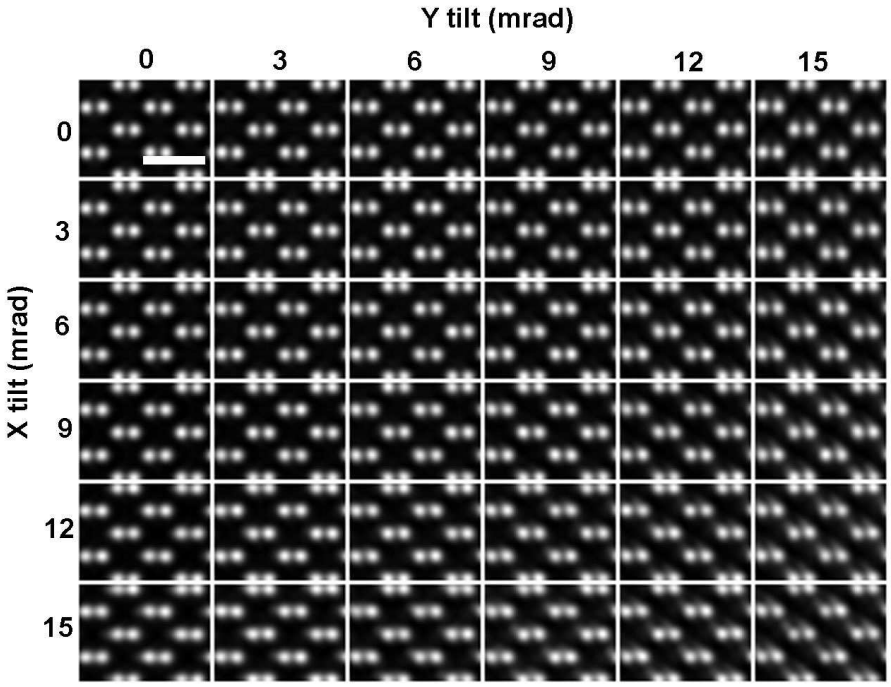

Figure 5.5: Simulated ADF-STEM images of 250Å thick crystal silicon specimens at different tilts using an aberration-corrected probe. Using the 0.8Å probe, the crystal was tilted around the [110] crystallographic orientation. The specimen tilt angles along x- and y-axes are marked and the white spots of highest intensity in the image indicate atomic columns. All images are scaled to fill the available grayscale. The scale bar is 5Å.

channeling of the incident electron beam that propagates through the specimen along the atomic columns. The crystal orientation, specimen thickness and types of atomic species present in the sample are known to be critical factors that can significantly alter the beam channeling. The next sections discuss the effects of some of these factors that might occur in combination with and in the presence of tilt.

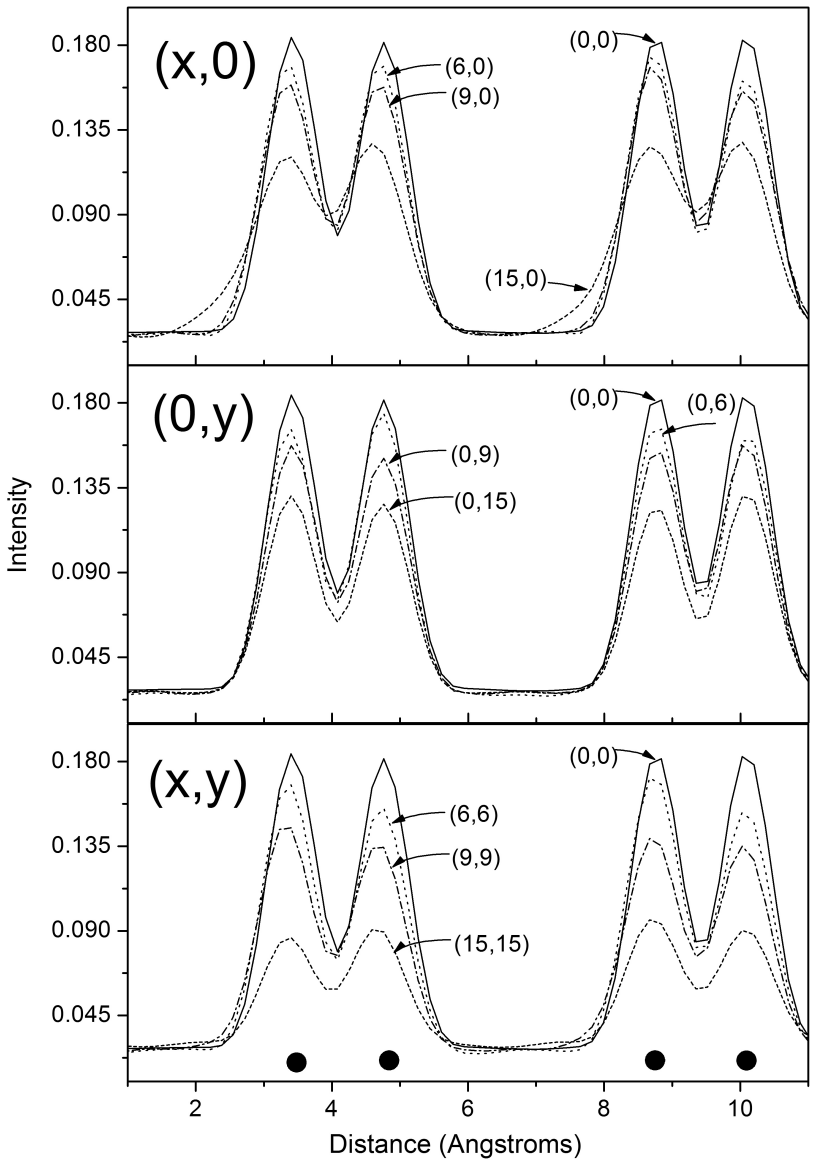

Figure 5.6: Line scans from simulated ADF-STEM images of Si oriented along the [110] direction at different tilt angles calculated using a 0.8Å probe. The linescans are taken across the dumbbells, and the tilt angles for each image are given in brackets (x,y). The upper plots show tilts in x, (x,0), the middle plot shows tilts in y, (0,y), and the lower plot shows equal tilts in both x and y, (x,y). The positions of atomic columns are indicated with black dots.

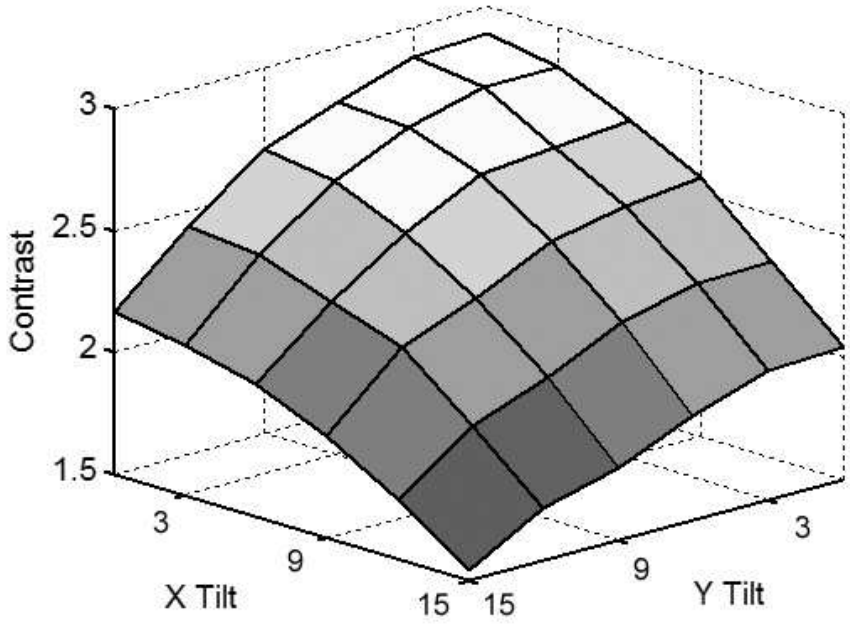

Figure 5.7: Image contrast calculated from ADF-STEM images of a Si specimen simulated at different tilt angles around the [110] crystallographic orientation with a 0.8Å probe.

5.3.1 Different crystallographic orientations

A set of high-resolution ADF images of the Si specimens were calculated with the crystal oriented along the two other major crystallographic orientations: [100] and [111]. Images for 250Å thick specimens were calculated for the aberration-corrected 0.8Å probe while the crystal was on-axis and tilted off-axis in increments of 6 mrad around the x- and y-axis. Figure 5.8 shows two arrays of images of these tilt series around [110] and [111] orientations. In both cases the crystal lattice is clearly visible even at the tilt of about 12 mrad. The values of the contrast calculated for both orientations are summarized in Table I. As in the case near the [110] orientation, significant reduction of contrast is observed when the crystal is tilted off-axis from the [100] and [111] orientations. For example, at a 12 mrad tilt in both x and y the atomic contrast of the high-resolution

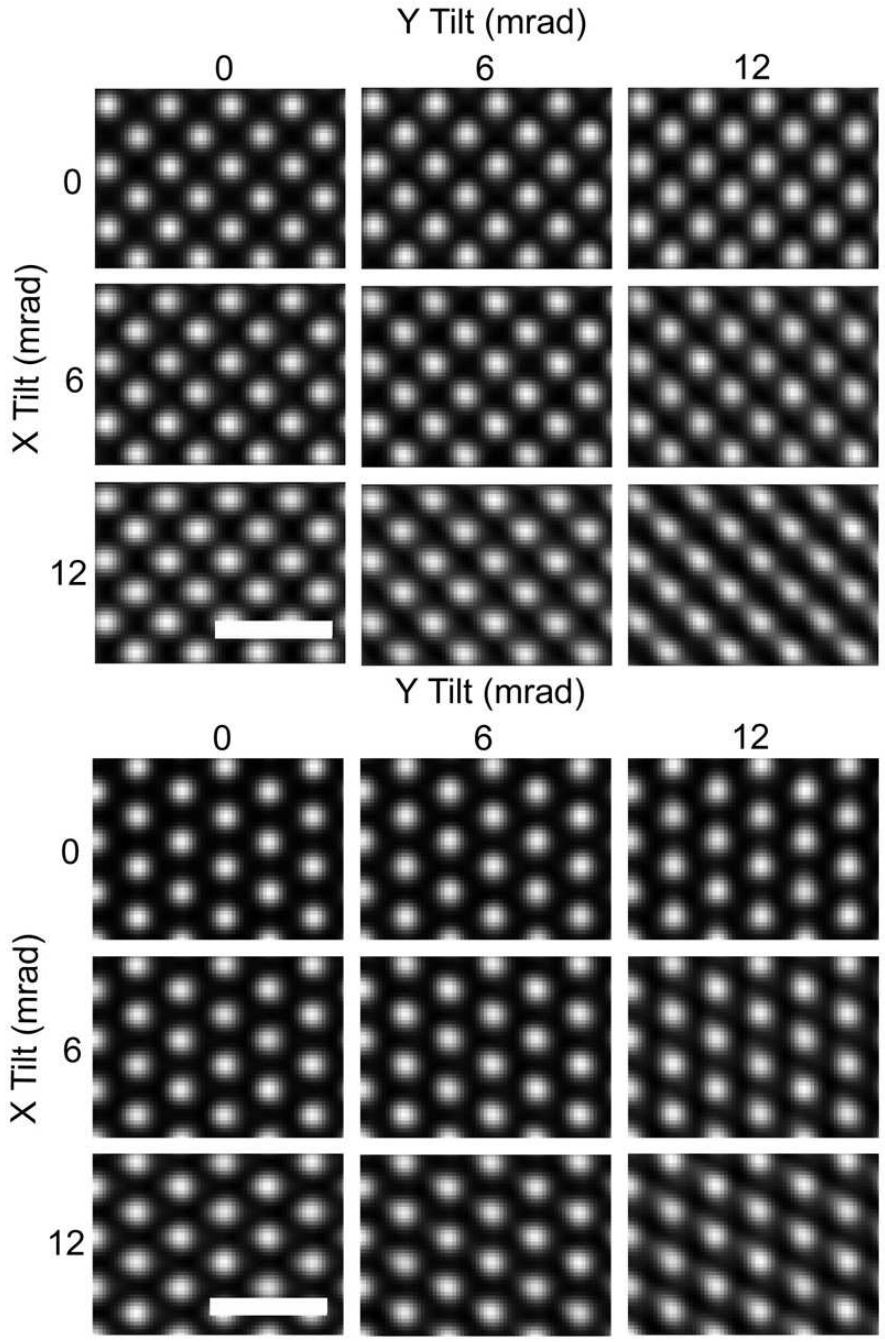

Figure 5.8: Simulated ADF-STEM images of 250Å thick crystal silicon specimens at different tilts for various crystallographic orientations. A 0.8Å probe was used and the crystal was tilted around the [100] (top) and [111] (bottom) crystallographic orientations. The specimen tilt angles along x- and y-axes are marked and the white spots of highest intensity in the image indicate atomic columns. All images are scaled to fill the available grayscale. The scale bar is 5Å.

Table 5.1: Contrast values for a 250Å thick Si specimen calculated from simulated ADF-STEM images created with a 0.8Å probe. Tilts are around the [100]/[111] orientations.

	Y Tilt (mrad)		
X Tilt (mrad)	0	6	12
0	1.536/1.896	1.435/1.816	1.243/1.458
6	1.429/1.753	1.348/1.649	1.165/1.365
12	1.219/1.488	1.166/1.383	0.890/1.105

ADF images decreases by a factor of 0.6.

5.3.2 Different specimen thicknesses

A series of ADF-STEM images of Si crystals was simulated for thicknesses from 50 to 750Å with 50Å steps. For enhancement of the effects the specimen was tilted to 15 mrad (or $\approx 1^{\circ}$) off of the [110] orientation around both the x- and y-axis. For a 750Å-thick sample under these tilt conditions the top and bottom atoms of atomic columns in Si are shifted with respect to one another in the x-y plane by 11.2Å, leading one to expect dramatic changes in the tilted ADF images. As before, two STEM probes were considered here: the 2Å probe and the aberration-corrected 0.8Å probe. Eight of these simulated ADF images for both probes are presented in Figure 5.9. Surprisingly, as can be seen from Figure 5.9, even for a 750Å thick specimen, atomic columns are still visible. The positions of the bright spots correspond to the positions of the top atoms in the columns.

For detailed analysis the contrast of all simulated ADF images was calculated and the values of C are plotted as a function of thickness in Figure 5.10(a). In addition, the values of the ADF intensities of the bright spots corresponding to the position of the atomic columns and dim spots (the spots in between

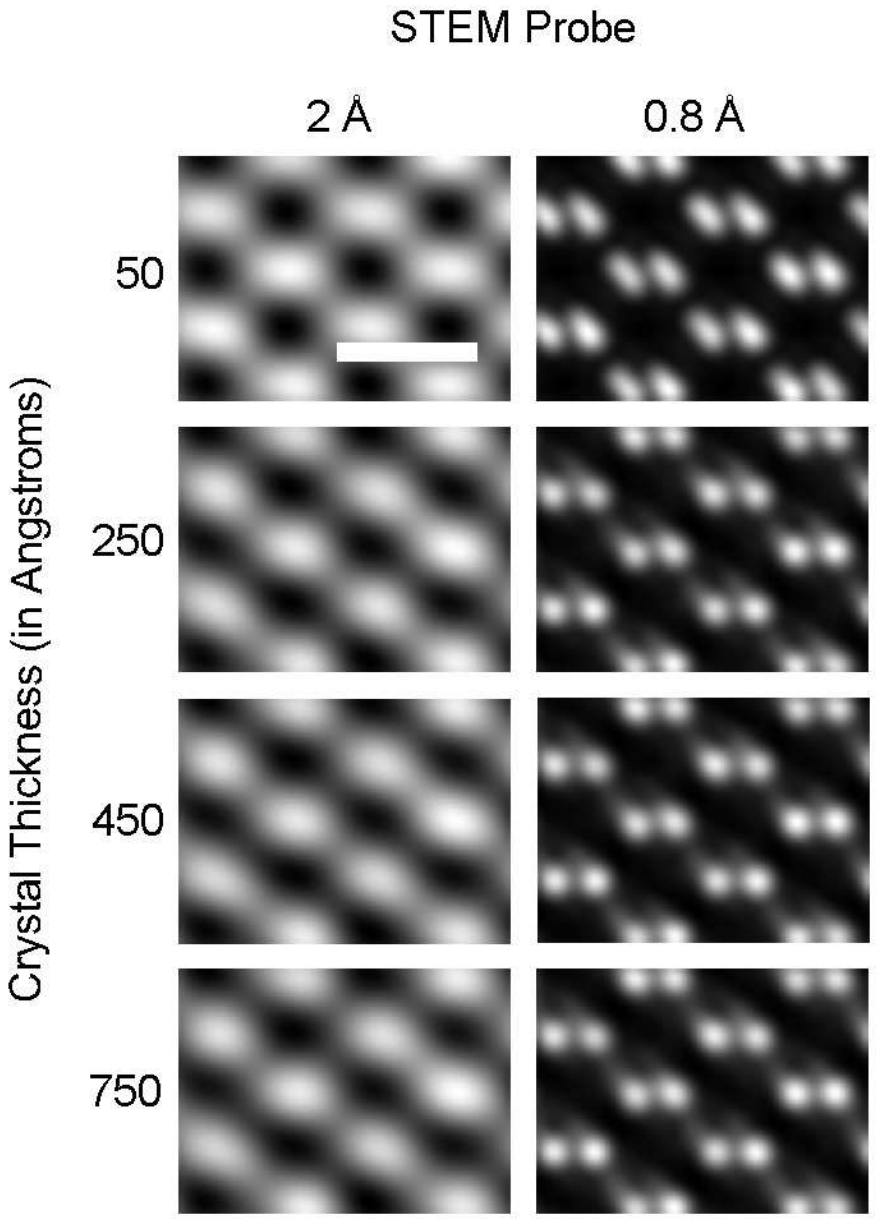

Figure 5.9: Simulated ADF-STEM images of crystal silicon specimens at different thicknesses with (15,15) mrad tilt off of the [110] crystallographic orientation. Left column is calculated with a 2Å probe and right column with a 0.8Å probe. All images are scaled to fill the available grayscale. The scale bar is 5Å.

the columns with the smallest intensity) as well as the mean intensity values of the images are presented in Figure 5.10(b). The intensities of the bright spots increase with thickness as does the mean intensity of the image. However, the contrast drops as the thickness increases. The contrast reduces fairly quickly for specimens with thicknesses from 50 to 150Å and then decreases at a slower rate up to the final thickness of 750Å. This type of dependence of the contrast to the thickness was observed for both probe sizes.

5.3.3 Different ADF detectors

All of the ADF-STEM simulated images presented to this point have been calculated using an ADF detector with 54-330 mrad inner-outer angles. The sensitivity of the ADF signal to the detector geometry and in particular to the inner angle has already been studied in detail and as a result some STEMs are now equipped with double ADF detectors which record simultaneous images. The nested detectors consist of a low-angle ADF (LAADF) detector that typically has 25-50 mrad inner-outer angles and a high-angle ADF (HAADF) detector that collects electrons scattered into 50-250 mrad conical solid angle [9]. HAADF images are expected to form images of the specimen with primarily incoherently scattered electrons while the LAADF images tend to have a combination of incoherently and coherently scattered electrons. To study the effects these different collection angles can have upon tilted samples, ADF images with three different ADF collector configurations were simulated. In addition to the ADF detector geometry used earlier in the paper (54-330 mrad inner-outer angles), which will be labeled ADF1 in this section, two other ADF detector geometries, ADF2 and ADF3, were simulated as well. ADF2 corresponds to 35-220 mrad inner-

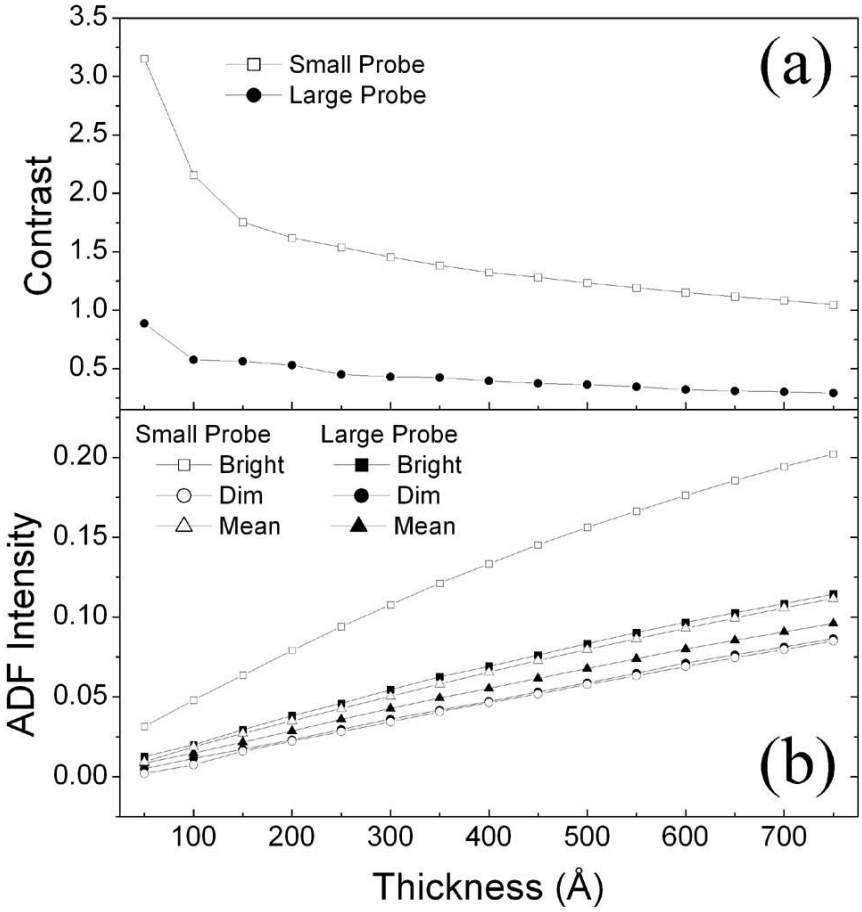

Figure 5.10: Contrast and intensity of ADF-STEM images on specimen thickness as calculated for a Si specimen tilted 15 mrads off of the [110] crystallographic orientation in both the x and y axes using corrected and uncorrected probes. (a) Dependence of the ADF image contrast on specimen thickness. (b) The actual intensities from the brightest and dimmest spots and mean intensities of the ADF images as a function of thickness.

outer angles and ADF3 corresponds to 27-165 mrad inner-outer angles. Figure 5.11 shows a calculated CBED pattern from a Si specimen aligned with the incident beam along the [110] orientation using an aberration-corrected 0.8Å probe whose convergence angle is α_{obj} = 25mrad. The positions of the inner angles of all three ADF detectors used in this paper are also marked as white circles.

To maximize the visibility of the effects of tilt, 6 and 15 mrad tilts (in both

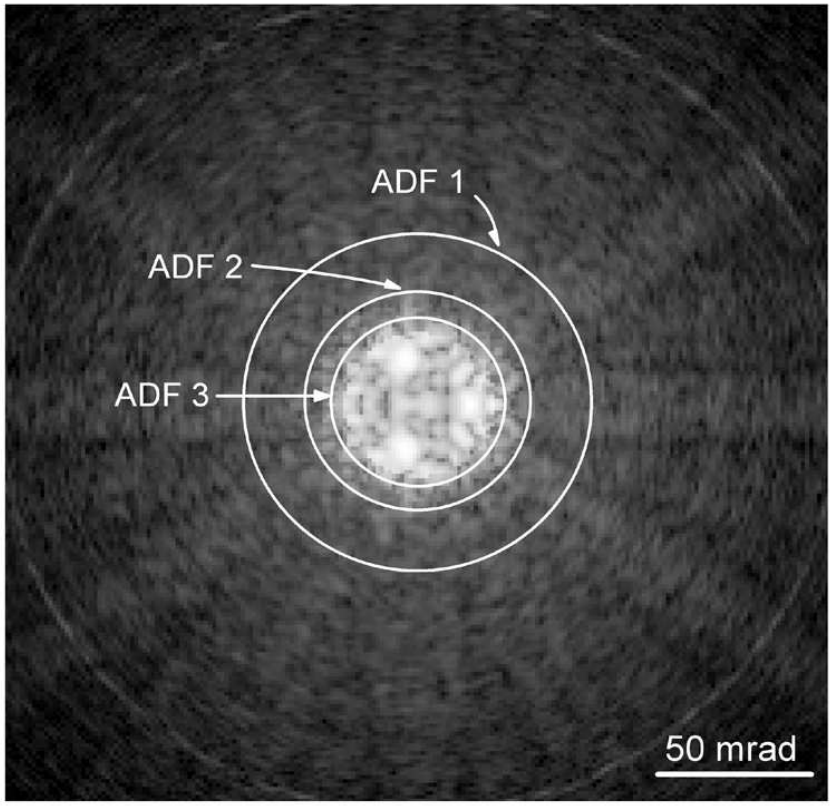

Figure 5.11: Calculated CBED pattern for a 250Å-thick Si specimen along the [110] orientation using an aberration-corrected 0.8Å STEM probe with a 25 mrad convergence angle. The inner angles of all three ADF detector geometries are indicated on the image with white circles. The values of the detector inner angles are 54 mrad (ADF1), 35 mrad (ADF2) and 27 mrad (ADF3).

the x- and y-directions) were considered. A 250Å thick Si crystal in the [110] orientation was used in these calculations. Here the images were simulated only for the aberration-corrected 0.8Å STEM probe, and are presented in Figure 5.12. As can be seen from this set of images, at zero-tilt the differences between different detectors are not significant. However, for a tilt of 15 mrad the images recorded with the two ADF detectors with smaller inner angles show quite visible differences in the images as compared to those calculated for the ADF1 detector. A noticeable brightening of the area between the columns is observed.

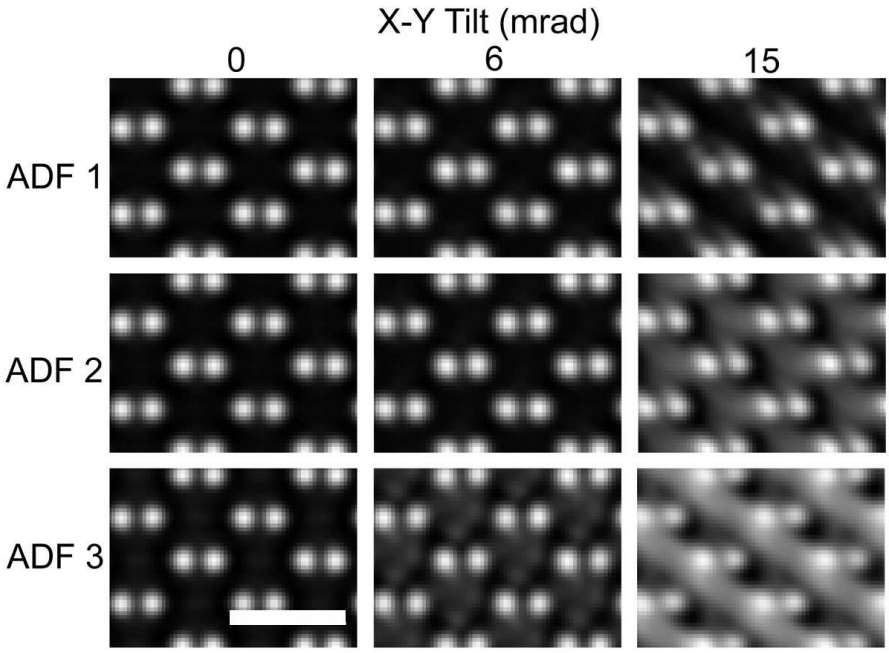

Figure 5.12: Simulated ADF-STEM images of 250Å-thick crystal silicon specimens with different tilt angles and ADF detector geometries: 54-330 (ADF 1), 34-220 (ADF 2) and 27-160 mrad (ADF 3) inner and outer detector angles. The 0.8Å probe was used and the crystal was tilted around the [110] crystallographic orientation. The specimen tilt angles along the x- and y-axis are indicated. All images are scaled to fill the available grayscale. The scale bar is 5Å.

Indeed, the smaller the detector inner angle the more intensity appears between the columns as the sample is tilted off-axis. This likely is caused by redistribution of the intensities in the diffracted beams and the geometry of the overlap of the CBED discs inside a particular ADF detector.

5.4 Discussion

The results of the multislice simulations on crystalline Si presented in the previous sections show that high-resolution ADF-STEM imaging is still possible when the sample is slightly tilted. The effects were the same for both the un-

corrected 2Å STEM probe and the aberration-corrected 0.8Å probe. The atomic columns of Si were quite visible up to the maximum simulated tilt of 15 mrad (or $\approx 1°$) regardless of crystal orientation or ADF detector geometry, and remained visible for specimens as thick as 750Å. However, the results also suggest that despite the visibility of the atomic columns the contrast in these images is expected to be reduced significantly with tilt. In the case of a 15 mrad tilt a factor of two reduction in contrast is predicted for all three major orientations of the crystal. Dramatic reduction of the contrast was also observed with an increase of the thickness of the specimen; from $C \simeq 4.3$ for t =50Å-thick samples to $C \simeq 2$ for t =450Å-thick samples when imaged with an aberration-corrected 0.8Å probe.

Since the tilt of the specimen affects the strength of the channeling of the incident electrons along the atomic columns, as discussed by Loane et al. [1], the number of electrons that scatter into the ADF detector will be reduced for a tilted sample relative to the zone-axis oriented sample. Therefore, the intensity of the ADF signal at the position of the atomic columns is expected to be lower for a tilted specimen than in the non-tilted case and this is exactly what was observed in the calculations presented here. In Figure 5.13 the intensity of the incident beam is calculated as a function of depth when the beam is positioned on one of the columns of the Si dumbbell along the [110] orientation. Two cases were considered: untilted and a (15,0) mrad tilt using a 0.8Å aberration-corrected probe.

In the case of the untilted specimen strong channeling is observed (see Figure 5.13(a)), which is consistent with earlier results by Hillyard et al., [10, 11] Allen et al. [12] and Voyles et al. [13]. However, a significant reduction of channeling takes place when the sample is tilted off the zone axis (see Figure 5.13(b)). It is

interesting to note that in the case of a tilted specimen the dynamic of dechanneling of the incident probe to the neighboring column is different than in the untilted case. Less intensity is immediately channelled down the atomic column, with the remaining intensity continuing on at an angle of approx 25 mrads to the atomic column as is seen in Figure 5.13(b) (along the dashed line). The reason the remaining intensity is deflected to an angle larger than the tilt angle of 15 mrad from the atomic column is most likely due to a combination of factors which include channeling effects and the relatively large incident angles of the convergent probe. When the probe is located between the columns the ADF intensity is not expected to be strongly affected by the specimen tilt, since channeling is not significant at these points. This agrees with the observed relatively small changes in ADF signal for points between the columns in the simulations (see Figures 5.3 and 5.6).

The observed dependence of the ADF signal upon the thickness of the sample is quite interesting. An early report by Hillyard and Silcox [14] based on multislice simulations performed on untilted crystals indicates that the intensity of the ADF signal from the atomic columns should increase with thicker specimens. Similar dependence is also observed in this study, even in the presence of a 15 mrad tilt. However, despite the increase of the intensities in the ADF images on-column and off-column, as can be seen in Figure 5.10, the overall contrast of the image reduces corresponding to the reduction of beam channeling [1].

ADF-STEM image calculations performed for different ADF detectors indicate that the appearance of images recorded with smaller detector inner angles are more sensitive to tilt than HAADF images. In a previous study done with

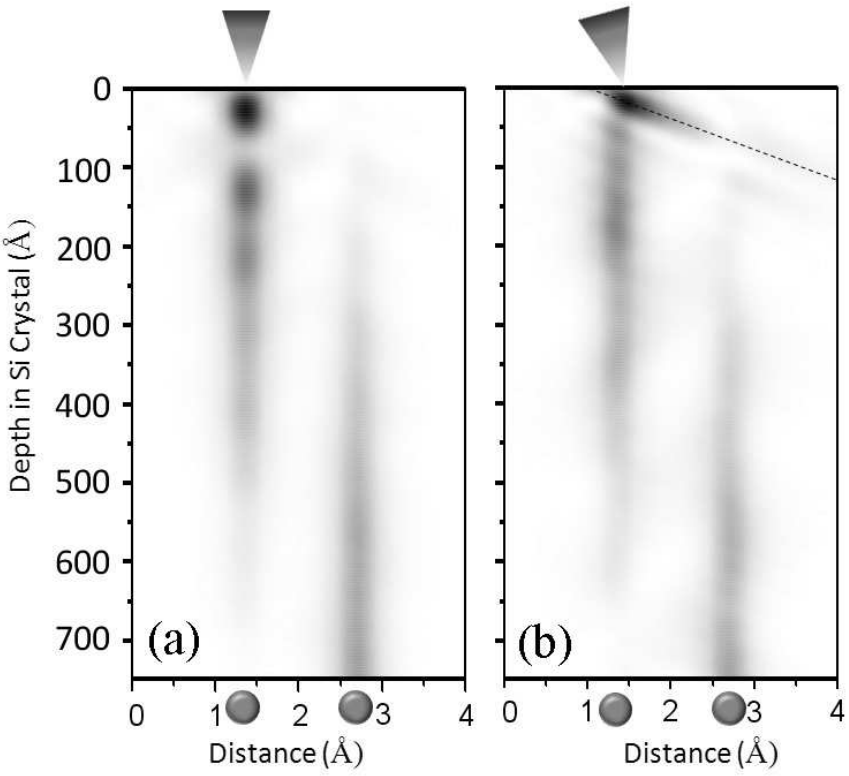

Figure 5.13: Depth section of the calculated intensity of the incident beam as it propagates through 750Å of Si with the beam aligned along the [110] orientation. An aberration-corrected 0.8Å probe was used. The probe was located on the left-hand column of the dumbbell and the linescans are taken along the length of the dumbbell. The positions of the columns are indicated as dots below the graph. (a) for untilted and (b) for (15,0) mrad tilted specimens. Highest electron intensity is black.

tilted silicon samples Yu et al. [2] showed that multislice simulations predicted that the intensity from a column of atoms in the ADF image decreases more rapidly in HAADF detectors than LAADF detectors. This is consistent with the results of the intensity values from the columns in ADF simulated images presented here. This present study is also able to observe the intensity changes in every location in the crystal as a sample is tilted. What is observed in these images is an increased level of intensity between the columns as the angle of the ADF detector decreases. With smaller inner angles of the ADF detector the

contributions of the diffracted beams become more influential in the formation of the image. When the sample is tilted, the distribution of intensities between the central disc and the diffracted discs changes, directly affecting the number of electrons collected by each ADF detector and, therefore, the intensity distribution of the ADF image. This is exactly what was observed in the simulated images presented in the previous section.

5.5 Conclusions

By being able to use multislice to simulate images with highly-controlled specimen tilts, the effect of tilting on the contrast of ADF images of on-axis crystals can be observed. Even small tilts, on the order of 10-15 mrad, have been found to reduce the contrast of ADF-STEM images of crystalline Si by as much as a factor of two. The contrast reduction in ADF-STEM images was found to be similar in simulations of both aberration-corrected and uncorrected probes, and a factor of two reduction in contrast is found in high-resolution simulated images for a Si crystal tilted off-axis by 15 mrad in both the x- and y-axes This strong reduction in contrast has been seen to hold for simulations of different orientations of the Si crystal. Also, the reduction in contrast is seen to increase with increasing thickness, though the rate of contrast reduction is not linear with thickness.

Finally, it was observed that ADF detectors with smaller inner angles are more sensitive to the effects of tilt than HAADF because of the collection of an increasing amount of coherently scattered electrons. This effect could possibly be used to check for small, otherwise undetectable shifts in tilt during imaging if an operator has a microscope with both HAADF and LAADF detectors, saving

the necessity of changing the optical conditions of the microscope from imaging to diffraction with every move to a new spot on the specimen.

BIBLIOGRAPHY

[1] R.F. Loane, E.J. Kirkland and J. Silcox, Acta. Cryst. **A44**, 912 (1988).

[2] Z. Yu, D.A. Muller, and J. Silcox, Ultramicroscopy **108**, 494-501 (2007).

[3] T. Plamann and M.J. Hytch, Ultramicroscopy **78**, 153 (1999).

[4] T. Yamazaki, M. Kawasaki, K. Watanabe, I. Hashimoto, and M. Shiojiri, Ultramicroscopy **92**, 181 (2002).

[5] P. Wang, A.L. Bleloch, U. Falke, and P.J. Goodhew, Ultramicroscopy **106**, 277 (2006).

[6] J.M. Cowley, A.F. Moodie, Acta. Cryst. **10**, 609 (1957).

[7] E.J. Kirkland, *Advanced Computing in Electron Microscopy* (Plenum Press, 1998).

[8] K.A. Mkhoyan, S.E. Maccagnano-Zacher, E.J. Kirkland and J. Silcox, Ultramicroscopy **108**, 791 (2008).

[9] D.A. Muller, N. Nakagawa, A. Ohtomo, G.L. Grazul and H.Y. Hwang, Nature **430**, 657 (2004).

[10] S. Hillyard, R.F. Loane and J. Silcox, Ultramicroscopy **49**, 6 (1995).

[11] S. Hillyard and J. Silcox, Ultramicroscopy **58**, 14 (1993).

[12] L.J. Allen, S.D. Findlay, M.P. Oxley, and C.J. Rossouw, Ultramicroscopy **96**, 47 (2003).

[13] P.M. Voyles, D.A. Muller, and E.J. Kirkland, Microsc. Microanal. **10**, 291 (2004).

[14] S. Hillyard and J. Silcox, Mat. Res. Soc. Symp. Proc. **332**, 361 (1994).

CHAPTER 6

NANODIFFRACTION AND DAMAGE MEASUREMENT OF CDSE NANOPARTICLES

6.1 Nanodiffraction of CdSe Quantum Rods

Nanodiffraction is the process of collecting diffraction patterns from a nanometer-sized spot on a specimen, and is a powerful tool for the ongoing nano-revolution [1]. The nanodiffraction patterns are obtained by reducing the objective angle of the probe by inserting a smaller objective aperture. This reduces the size of the diffraction spots from the large, overlapping diffraction spots found with CBED using a 10 mrad objective aperture, to smaller diffraction discs that do not overlap using a 2-4 mrad objective aperture. Just changing the aperture from a large to a small one is not adequate, however, as the beam current gets reduced to a prohibitively low level and the diffraction patterns are undetectable. The optical conditions are changed in the Cornell VG STEM, therefore, by powering up the C1 lens and using this lens to send the electrons more tightly focused into the C2 lens, which focuses the beam onto the SAD aperture and then into the objective lens. This produces a larger beam (1.5-0.7nm) with a smaller convergence angle and with a beam current equal to that of the beam used for imaging. Though the nanodiffraction beam is larger than the ~0.2 nm one used for imaging, it is sufficiently small to localize the diffraction pattern to a portion of a quantum nanorod (QR).

The study of diffraction patterns taken along the length of CdSe QRs was done very thoroughly by Yu et al. [1, 2]. It was shown in that study that the crystal orientation changed along the length of the CdSe QRs by small and ran-

dom twists that could not be attributed to a screw dislocation or any other progressive strain effect. It can also be observed in the high-resolution ADF STEM images of on-axis QRs that the crystal structure has stacking faults and sections of crystal that apparently have a different crystal structure from that of the crystal around. An example of such a stacking fault is shown in Figure 6.1. The thick, white arrows point out sections of the QR that have multiple stacking faults that create an area of different-looking lattice fringes. It is possible that this different crystal lattice fringe could be the result of a zinc-blende section in a wurtzite crystal, but it is impossible to know for sure unless a diffraction pattern is obtained from the small sections of different lattice fringe. Therefore, nanodiffraction was attempted in order to determine if these sections of crystal could be characterized.

Diffraction patterns were obtained from the spots on the CdSe QR indicated by white circles in Figure 6.1. The diffraction patterns are shown in Figure 6.2 and are numbered to indicate approximately from where the pattern came. The first diffraction pattern was obtained from the foot of the rod, marked in Figure 6.1 with a ”1”. The diffraction patterns were taken progressively up the QR, ending at the top of the rod marked with an ”8”. The first five diffraction patterns are all different from one another, showing that the crystal orientation along the rod is not constant. Indeed, the first diffraction pattern shows an area that is likely amorphous. However, none of the diffraction patterns are what would be expected for a wurtzite crystal oriented exactly along the $[\bar{2}110]$ direction, as the high-resolution lattice fringes suggest for the orientation. In addition, it was observed that something in the image was changing in the QR during measurement, though the resolution of the images was very low due to the optical parameters of the microscope being optimized for diffraction. Therefore,

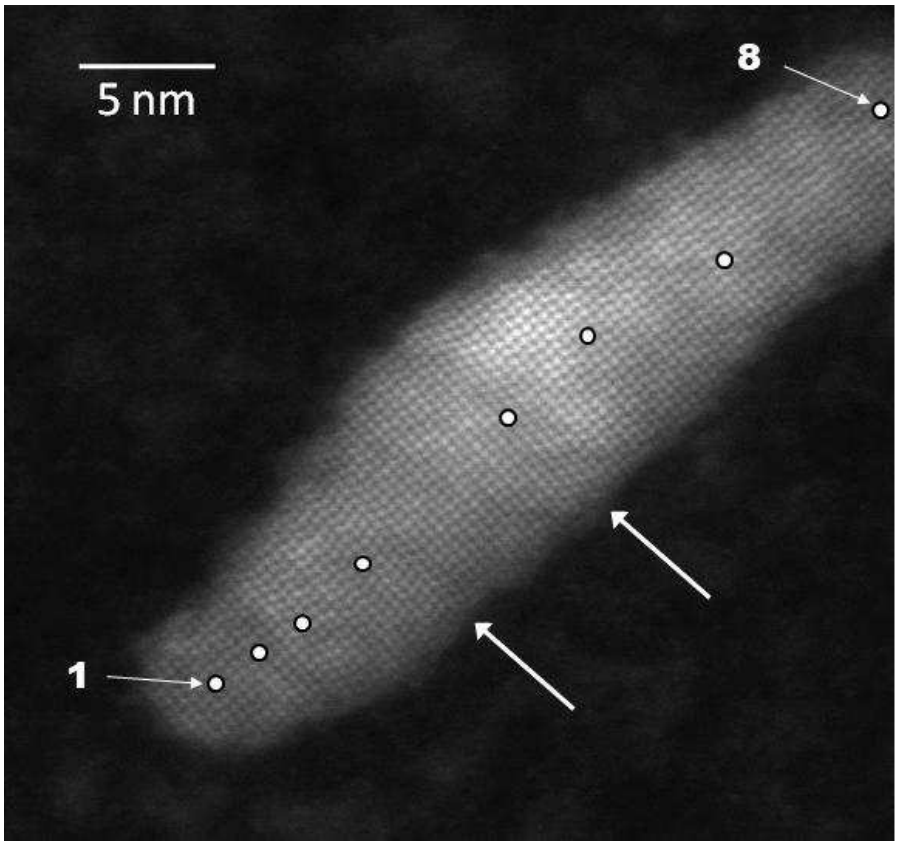

Figure 6.1: High-resolution ADF image of a CdSe QR. The thick, white arrows mark areas of stacking faults and possible crystal structure change in the rod. Eight diffraction patterns were obtained from the areas marked with the white circles, progressively acquired from the foot of the rod (marked ″1″) up to the top (marked ″8″).

the microscope was realigned for imaging optical conditions and a second image was taken of the same QR. Figure 6.3 shows another high-resolution ADF STEM image of the same QR after the diffraction patterns were obtained. The QR is so damaged that it is difficult to see the original shape. A white dotted line shows the original perimeter of the QR, and white circles mark the approximate acquisition areas from which the diffraction patterns were taken. The lattice fringes in the damaged QR are now appearing as a one-dimensional pattern, unlike the two-dimensional fringe appearance it had before acquiring the

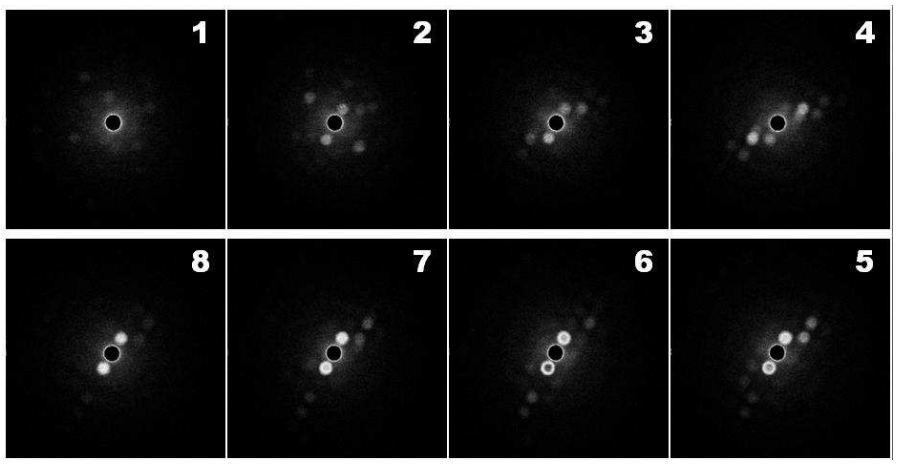

Figure 6.2: Diffraction patterns acquired from nanometer-sized areas on the CdSe QR. Patterns 1-5 are all different from one another, indicating the crystal tilt or structure is changing along the length of the rod shown in Figure 6.1.

diffraction patterns. It is likely, therefore, that the damage due to the electron beam also shifted the rod in relation to the beam and moved it from its on-axis tilt to something slightly off-axis which explains the diffraction patterns. It should be pointed out, however, that although QRs may infrequently shift under a sustained exposure to the STEM probe, high-resolution images taken before and after numerous measurements and exposures have shown that the shift of the QR happens early in the exposure and does not change after the initial shift. Therefore, the results that were observed by Yu, et al. [1] cannot be explained by a QR continually shifting and shimmying under the electron probe as it progresses up the rod. Could the results seen by Yu, et al. be explained by increasing damage under the beam causing the crystal structure, and therefore the diffraction pattern, to change as has been previously reported, e.g. in carbide nanoparticles [3]? To test the amount of crystal structure deformation and subsequent diffraction pattern change, the electron probe was held on a spot for 90 seconds and a diffraction pattern was taken at the beginning and the end of the prolonged exposure. Ninety seconds is much more exposure than is nor-

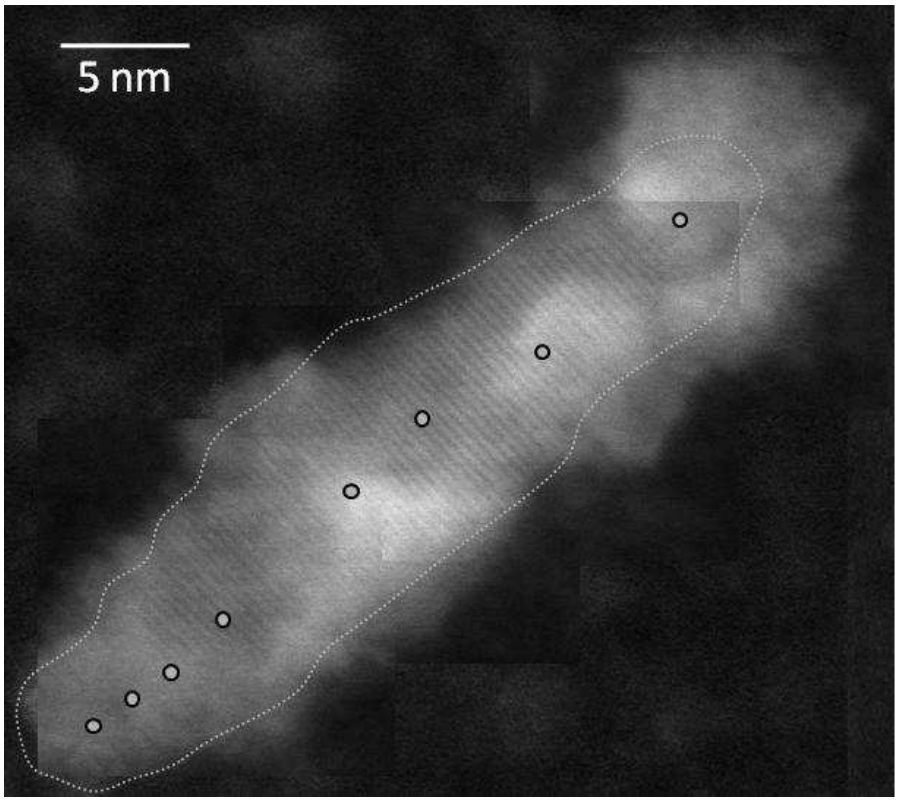

Figure 6.3: High-resolution ADF image taken of the same QR as in Figure 6.1 after being damaged by the electron beam. The image is formed by a collage of images taken within a few minutes of each other and with the same microscope conditions. The perimeter of the original, undamaged QR is shown with a white dashed line. The area from which diffraction patterns were taken are indicated with white circles.

mal when obtaining a single diffraction image and tests the limits of imaging a diffraction pattern with beam damage. Figure 6.4 (a) shows the initial diffraction pattern taken from the CdSe QR and Figure 6.4 (b) shows the diffraction pattern after 90 seconds of beam exposure. The diffraction patterns are not notably different, demonstrating that the crystal structure of the CdSe QRs remains constant under exposure and that any amorphous damaged material building up on the exposure spot does not profoundly alter the diffracting conditions.

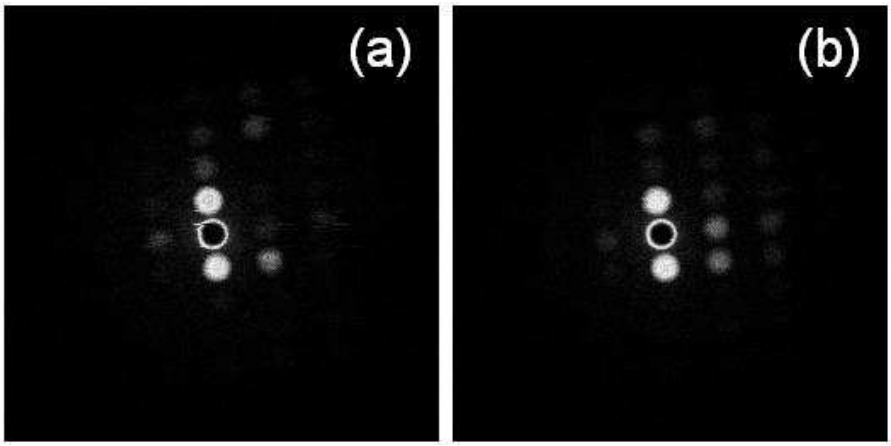

Figure 6.4: Diffraction patterns taken from a nanometer-sized area on a CdSe QR. (a) The initial diffraction pattern and (b) after 90 seconds of electron beam exposure.

6.2 Damage Measurement of CdSe Quantum Rods

As the previous section shows, high-energy electron beam damage to the specimen–especially small, thin specimens–is a ubiquitous problem that must be explored in order to be avoided or, at least, minimized. The measurement capabilities of the STEM also provide a good opportunity to understand and quantify the damage of materials heretofore unstudied. This study demonstrates how unusual and exceedingly small pieces of material can be studied individually in STEM to glean information about damage rate and cohesive energy.

The mass loss seen in the previous section has been observed and reported for 100 keV electron bombardment on various materials [4, 5, 6, 7] and various mechanisms for the damage has been explored. The loss of mass from the sample is ultimately caused by surface sputtering, where the energy transferred from the incident electron to a surface atom is enough to overcome the threshold

energy for removal. For transmission electron microscopy, surface sputtering occurs when the high-energy electrons travel through the thin film and sputter atoms at the exit surface. Bulk sputtering, where an atom buried in the bulk is removed, is much more unlikely than surface sputtering because of the increased amount of energy needed to remove the added bonds of a bulk atom compared to a surface atom.

In these damage studies, a 0.2 nm electron beam was held on a CdSe quantum rod as EELS data were acquired. Each Cd $M_{4,5}$ edge acquisition required 10 seconds, and images were taken intermittently during the total experiment time in order to measure drift and to manually place the beam back to the original damage spot. The amount of damage caused by the imaging is minimal because the beam is scanned during imaging, resulting in a total beam dose per pixel of five orders of magnitude less than that used in the spot-EELS acquisition. Therefore, almost all the damage during the total experiment time can be accounted for during the EELS acquisition. Figure 6.5 (c) shows an example of EELS data acquired during one experiment from 0 to 8 minutes of exposure. Though the spectra are quite noisy due to the lack of signal from the small specimen size, it is still easy to see the reduction in amount of Cd under the beam as shown by the loss of area under the Cd $M_{4,5}$ edge. Figure 6.5 (a)-(b) shows the mass loss in a different way–the reduction of ADF image intensity in the spot under the beam as the sample is exposed. This is the same quantum rod and the same spot from which the EELS data in Figure 6.5 (c) came.

Figure 6.6 shows a more quantitative measure of the ADF intensity mass loss so easily observed in the ADF images. For this plot the ADF intensity is measured at the same time each EEL spectra is measured, so at each time a

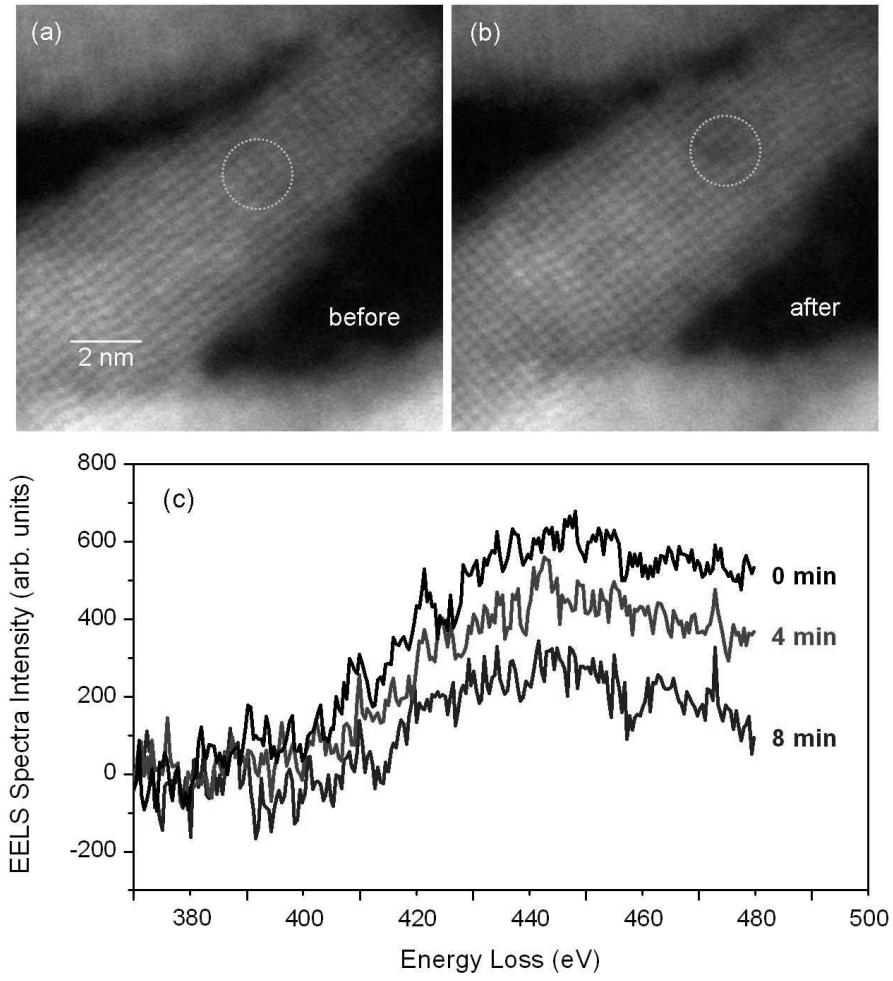

Figure 6.5: (a) Image of CdSe rod showing an area (white circle) before irradiation with the STEM beam. (b) Same area of the CdSe rod after eight minutes of irradiation with a fixed STEM beam. The reduced intensity in the area within the white circle represents a reduced amount of material. (c) Sample EEL spectra of the Cd M-edge taken from the QR at different exposure times with the exposure time under the beam noted to the right of each spectrum. The reduction in the area under the M-edge shows the reduction in the interaction of the electron beam with Cd atoms, and therefore is a good measurement of the relative abundance of Cd in the path of the beam.

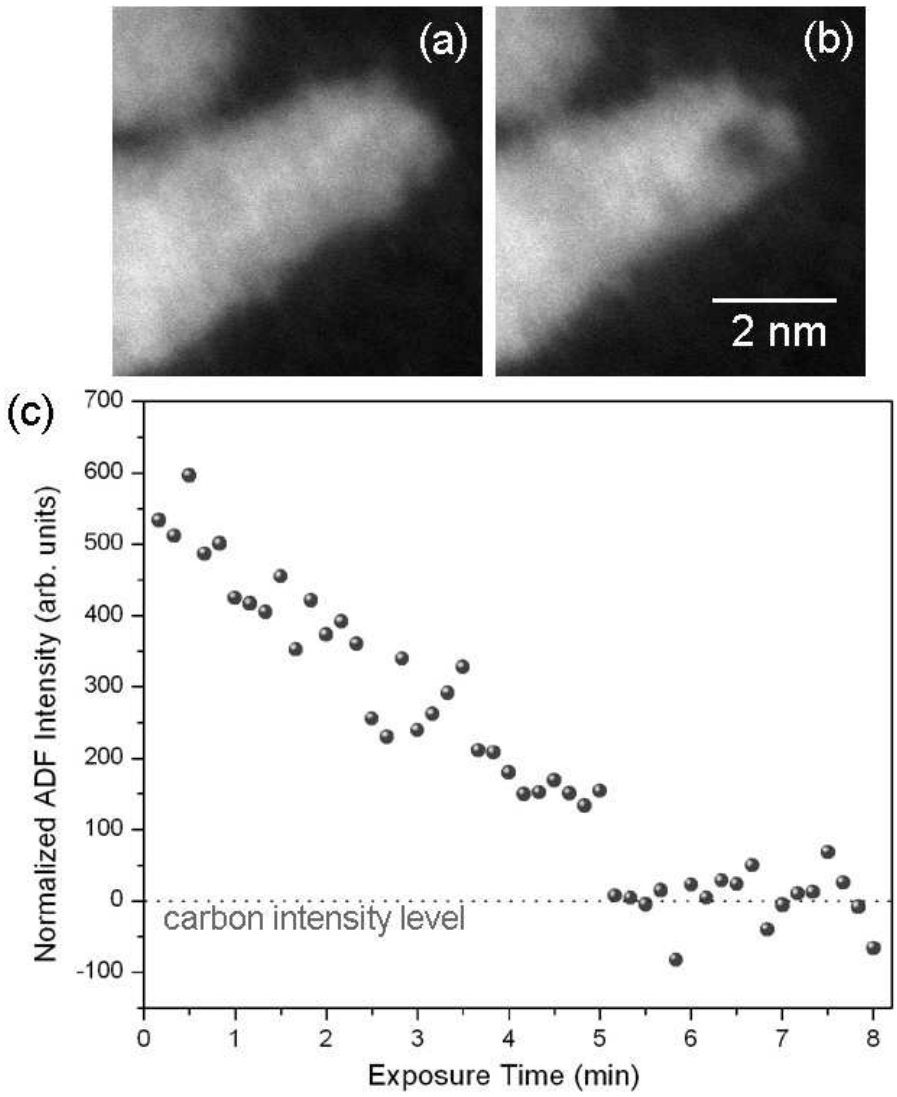

Figure 6.6: (a) Image of a CdSe rod before irradiation with the STEM beam. (b) Same rod after irradiation showing the dark spot in the ADF image representing the damaging loss of material from the irradiation. (c) Plot of ADF intensity taken as a function of time under the STEM beam. This data was taken during the damage that occurred in (a)-(b). After five minutes the intensity of the damaged rod flattens out at the level of the blue dotted line, which shows the intensity level of the carbon substrate. The substrate intensity was measured from the ADF image and subtracted from the data so that the carbon background intensity, I_c=0.

spectrum is taken and the rod is damaged a little further, the value of the ADF intensity is also measured. The plot (Figure 6.6 (a)) shows the rapid decrease of the intensity in this particular rod, which is shown before and after the damage experiment in Figure 6.6 (a) and (b). After about five minutes of damage on this particular rod, it can be seen that the ADF intensity reduces to the same level as the ultrathin carbon substrate, signifying that the electron beam has sputtered through the entire rod. This can be seen from the images as well.

Though the ADF intensity reduction can give us an idea of the total amount of thinning that goes on due to the electron beam sputtering, the EELS data can give much more quantitative information about what exactly is going on during the damage. Namely, by integrating under the Cd $M_{4,5}$ edge one can measure the loss of Cd in the sample. A plot showing the values of the integration under the Cd $M_{4,5}$ edge as a function of time for three different quantum rods is shown in Figure 6.7. Though the data points reflect the noisy nature of the EELS spectra from which they came, it is easy to see the linear reduction of Cd, with 80% loss after 8 minutes of damage!

It was reported by Bradley [8] that the introduction of a carbon coating on samples greatly reduces or eliminates the occurrence of electron beam mass-loss damage. This variation on the current experiment was easily created simply by flipping the sample upside-down and re-introducing it into the microscope. The STEM samples of quantum rods were all prepared by placing a drop of solution containing the quantum particles onto a TEM grid covered with an ultrathin carbon membrane. The drop is carefully placed so that none of the sample overflows to the underside of the grid, and is wicked off or allowed to evaporate without drawing the sample to the underside. This assures that most or all

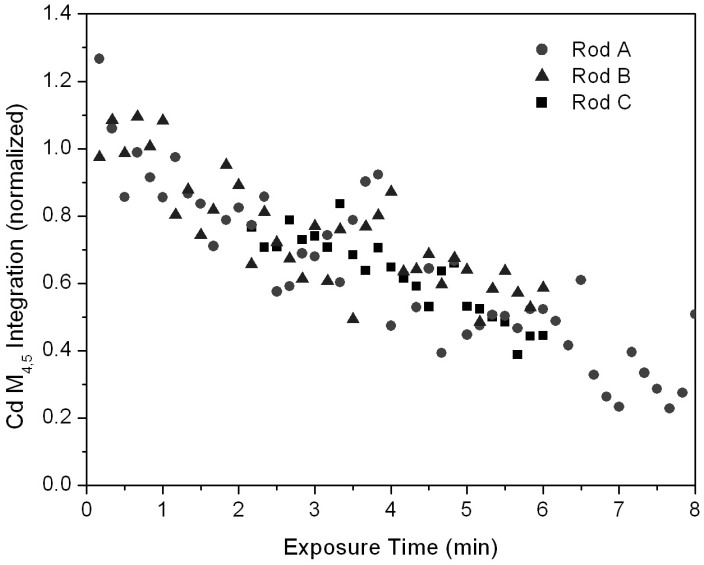

Figure 6.7: Plot of integrated EELS Cd core-loss signal during STEM beam bombardment as a function of time for three different CdSe rods. Rod A is the same rod as shown in Figure 6.5 and Rod C is shown previously in Figure 6.6. For all three rods the damage rate of Cd as reflected by the decrease of the M-edge intensity is similar.

of the quantum particles are located on one side of the sample, and by simply flipping the sample one way or another we can orient the sample such that the beam first encounters the sample before the carbon substrate, or encounters the carbon first before going through to the sample on the backside. The samples discussed previously in this section were all oriented so that the beam encountered the carbon substrate first and then the sample. This allowed all of the knock-on momentum of the electron beam to be used toward removing an atom from the surface and expelling it into the vacuum without the protective layer of a carbon coating creating a barrier. However, the protective nature of the carbon "coating" can be explored simply by flipping the sample so that the carbon substrate is now between the surface atoms of the quantum rod and the

vacuum.

Figure 6.8 shows ADF images of a CdSe rod before and after flipping the samples to the carbon-last orientation. It can be seen that no visible dark spot indicating mass loss can be seen, as was seen easily in the sample-last orientation shown before. In fact, as in this case, sometimes a bright spot appears in the area where the beam was held. For samples such as colloidally grown nanoparticles, a bright spot may perhaps be first assumed to be the appearance of contamination under the beam. However, the examples of bright spots after irradiation discussed in this chapter occurred on samples that otherwise showed no sign of contamination. Figure 6.9 shows the integration under the Cd $M_{4,5}$ edge as a function of exposure time for the carbon-protected orientation. It is plotted with the previous data to bring into contrast the lack of Cd loss in the "flipped" sample. It was not possible with the equipment used to measure the change of the amount of Se in the CdSe quantum rods because the weak signal of the Se $M_{4,5}$ edge was too small relative to the high background of the low-loss region at 57 eV. Therefore it was not possible to discover if Se was being removed despite the protective layer of carbon.

The bright spot that occasionally appeared during damage experiments while the sample was carbon protected is intriguing. Bright spots in damage areas have been seen before by Muller and Silcox [6] in Ni_3Al and by Mkhoyan and Silcox [7] in InN samples. In the former case, the spot directly under the beam was seen to decrease in ADF intensity, while a bright ring developed around. This bright ring was found to be from nickel enrichment around the damage area due to surface diffusion. In the latter case, the bright spot appeared directly under the beam spot and was most likely not due to any change

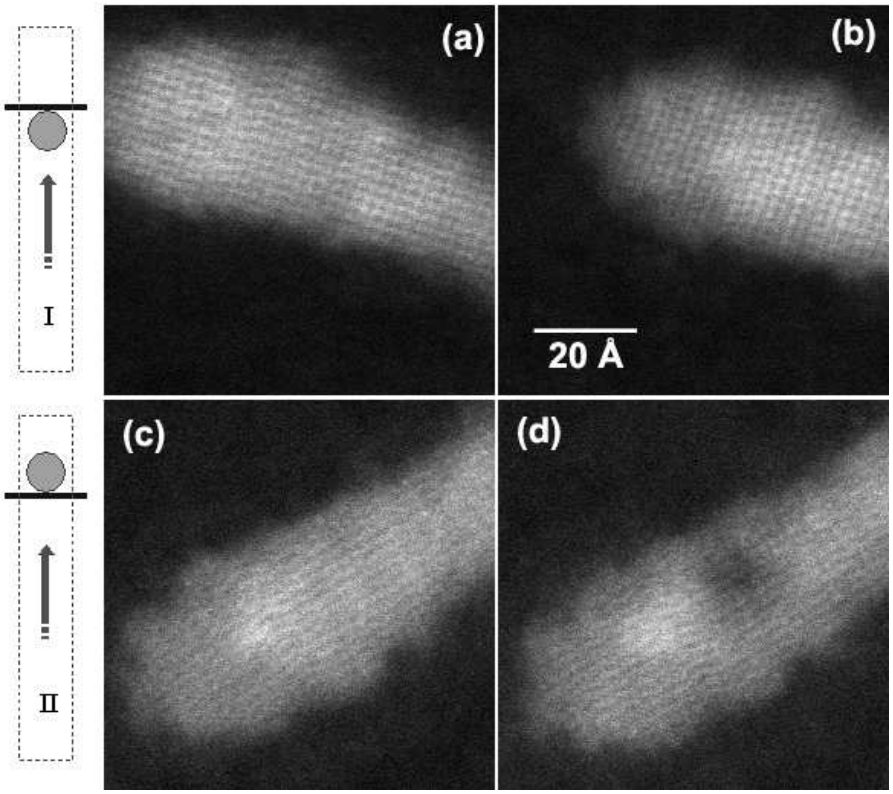

Figure 6.8: (a) Image of CdSe rod before irradiation by STEM beam when placed so that the beam hits the rod before going through the carbon substrate (schematic shown to the left–Case 1). (b) The same rod after irradiation by STEM beam with no obvious damage spot appearing. (c) The same rod after the sample was flipped so that the beam goes through the substrate before the rod (schematic shown to the left–Case 2). A bright spot is now apparent at the location the beam was held in (a)-(b). (d) After irradiating the same rod in the carbon-first orientation, a dark damage spot appears next to the bright damage spot from the previous experiment.

in average atomic number of the area, but from the difference of the beam scattering between the slightly mis-aligned surrounding crystal and that from the damaged area. This explanation for the bright spot in InN is also the most likely explanation to describe the presence of a bright spot in the CdSe samples when protected by the carbon substrate. There is no loss of Cd under the beam detected by EELS, and therefore no reason to believe that surface diffusion is creating an area of higher concentration of Cd, so the explanation must be that

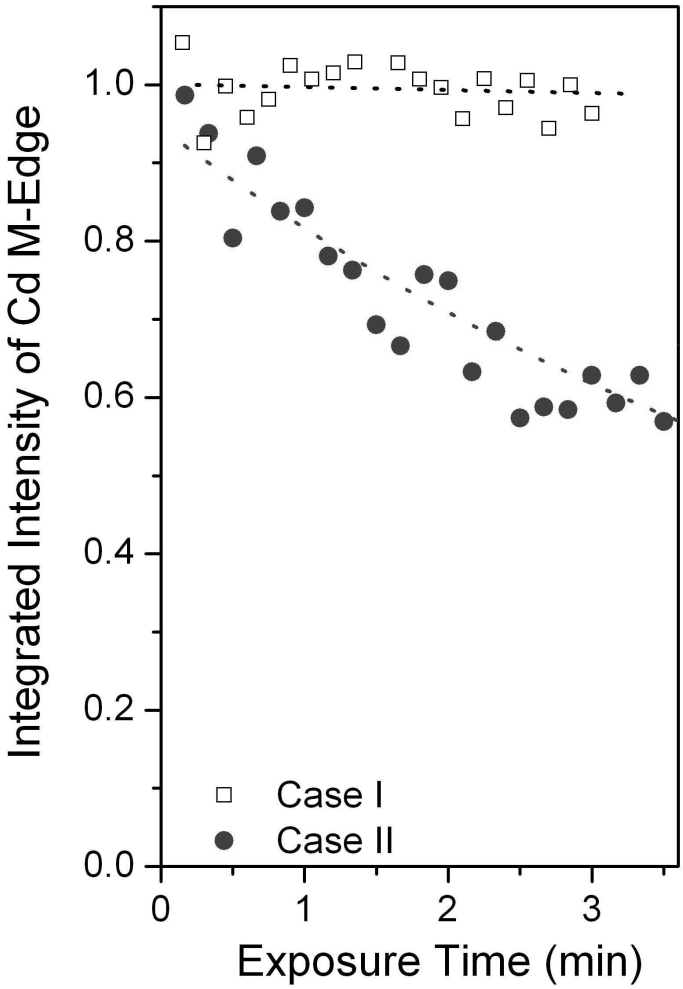

Figure 6.9: Plot showing integrated core-loss EELS of damage spots on a rod oriented in the carbon-last orientation (squares) and in the sample-last orientation (circles). The plot shows the increased loss of Cd in the sample-last orientation compared to the apparent lack of Cd loss when in the carbon-last orientation.

damage is occurring in the crystal lattice in the CdSe wurtzite structure, and the scattering of the beam will be different in the damaged area from the surrounding undamaged crystal.

6.3 Damage Theory

To more fully understand the process of damage in CdSe quantum rods, the Mott cross-section should be calculated for surface sputtering.

Consider an electron with rest mass, m_0, that is accelerated through a potential, V_0, thereby having the kinetic energy, $T_0 = eV_0$. This electron is scattered elastically with an atom whose nucleus has a rest mass of M. The amount of kinetic energy, T_n transferred to the atom nucleus by the incident electron is given by [9]

$$T_n = \frac{2T_0(T_0 + 2m_0c^2)}{Mc^2} cos^2\theta \tag{6.1}$$

where $cos^2\theta$ is the scattering angle of the nucleus with respect to the trajectory of the incident electron, and c is the speed of light. The maximum energy is transferred in a back-scattering event, creating an over-all forward motion to the scattered nuclei, and is given by

$$T_{max} = \frac{2T_0(T_0 + 2m_0c^2)}{Mc^2} \tag{6.2}$$

For 100keV electrons, this would give a maximum energy transfer of 2 eV for a Cd atom and 3 eV for a Se atom. To determine if this energy transfer is enough to sputter an atom from the CdSe crystal, the sputtering cross-section must be calculated.

To calculate the Mott cross-section of the Cd and Se atoms in CdSe, one first

needs to know the binding energy of the bulk and surface atoms. It is estimated that for bulk atoms, the binding energy can be approximated as 4 to 5 times the sublimation energy, while for surface atoms, between one and two times the sublimation energy is a good estimate of the binding energy [9]. For CdSe, the sublimation energy is 1.69 eV [10], thereby giving an estimated bulk binding energy between 6.8 and 8.4 eV and an estimated surface binding energy of 3.4 to 1.7 eV. Considering that the calculated maximum energy transfer to the Cd atom is 2 eV and the Se atom is 3 eV, the chances of sputtering a bulk atom would be very small to none, but a surface atom may possibly get enough energy to be removed.

Figure 6.10 shows the Mott cross-section for Cd and Se surface atoms as calculated by Bradley [9]. With the uncertainties surrounding the estimates for the value of the binding energy, it is still within reason to believe that surface atoms can be sputtered from the CdSe quantum rod, though the bulk sputtering cross-sections for both Cd and Se are still seen to be small or none.

In an attempt to find a more accurate value for the binding energy of the surface and bulk atoms in CdSe, the cohesive energy per bond of the crystal can be estimated and used to calculate a binding energy. One way to estimate the cohesive energy is to use the approximately linear relationship of the cohesive energy with covalency among the set of skew compound polar semiconductors. This is described in Harrison [11] and is shown to be empirically true for the homopolar semiconductor series of C, BN and BeO, and also for the isoelectronic series of Ge, GaAs and ZnSe as well as Sn, InSb and CdTe. The plots of cohesive energy as a function of covalency for these three series is shown in Figure 6.11 (a) and also that for three series of skew compounds are shown plotted in the

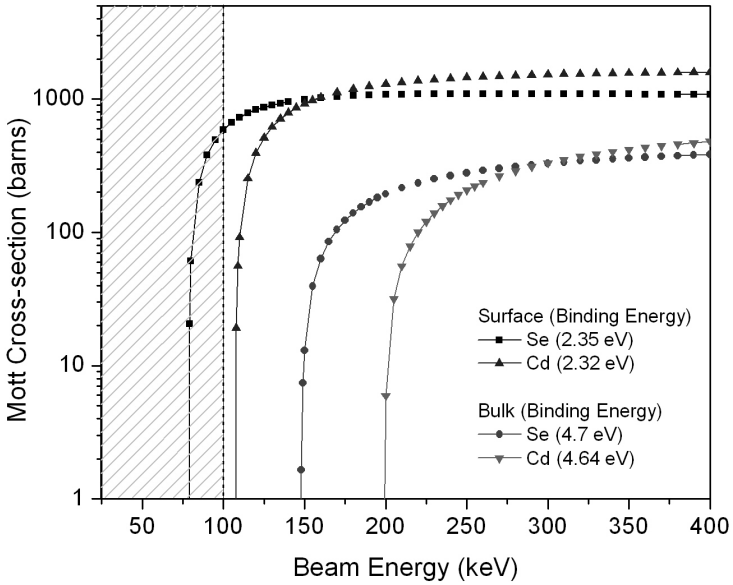

Figure 6.10: Mott cross-sections for surface Se (square) and Cd (up-triangle) atoms and bulk Se (circle) and Cd (down-triangle) atoms in CdSe. The hashed area denotes the electron energies provided by the 100 keV STEM and cross-sections in this area mean the possibility of sputtering by the beam. The Se surface atom is the only one whose threshold sputtering energy is unequivocally in this area. The cross-sections are calculated by Bradley [9].

same fashion in Figure 6.11 (b). The skew compound of CdSe belongs to the same series as GaSb, and using the straight line fit to the data points given for cohesive energy and covalency for the other three semiconductors in this series an estimate can be made of 1.16 ± 0.08 eV/bond for the cohesive energy of CdSe. Since there are four bonds in the bulk wurtzite crystal, and three bonds for every surface atom, this corresponds to a bulk binding energy of approximately 4.6 eV and a surface binding energy of 3.5 eV. This method gives a lower estimate for the bulk binding energy compared to that given by the sublimation energy, and matches the higher sublimation energy estimate for the surface binding energy. Still, however, this higher estimate is too large to allow for the kind of surface

sputtering that is seen in experiments from the CdSe quantum rods.

It has been observed by Medlin and Howitt [5] that there is not a single given value for a surface binding energy due to the fact that the energy depends upon the local atomic arrangement, and therefore the exact orientation of the crystal with respect to the beam. Also, contamination and surface ligands, common to colloidally grown nanoparticles, can create changes in the surface bonds and therefore the binding energy. Another factor that may contribute to a smaller binding energy for surface atoms in a quantum particle compared to a large, bulk crystal is the surface relaxation that has been found to occur in the incredibly small nanoparticle crystals [12]. This has been calculated theoretically for CdSe nanoparticles [13] predicting that the outer Se atoms would move outward by about 0.7 Å while the inner Cd atoms would relax inwards by about 0.5 Å. This "shell" of Se atoms in the outer layer created by such a relaxation was seen experimentally [14]. The subsequently longer bond would very likely correspond to a weaker surface sputtering energy, giving a possible explanation for the necessarily small value needed to see the amount of Cd loss that is observed in experiment. In addition, the surface binding energy has been shown to reduce as a crystal moves from bulk to nanoparticle size. [15, 16]. Qi and Wang [15] introduce the simple calculation for estimating the reduction of the surface binding energy in metallic samples as a function of particle size as

$$E_p = E_b(1 - \frac{d}{D}) \tag{6.3}$$

where E_P is the cohesive energy of the particle, E_b is the cohesive energy of the bulk, d is the diameter of the atom in the crystal and D is the particle diameter. This reduction of cohesive energy with decreased particle size was observed experimentally by Kim et al. [16] in the case of Mo and W nanoclusters. Therefore, it might be expected that as CdSe crystals decrease in size, the cohesive energy

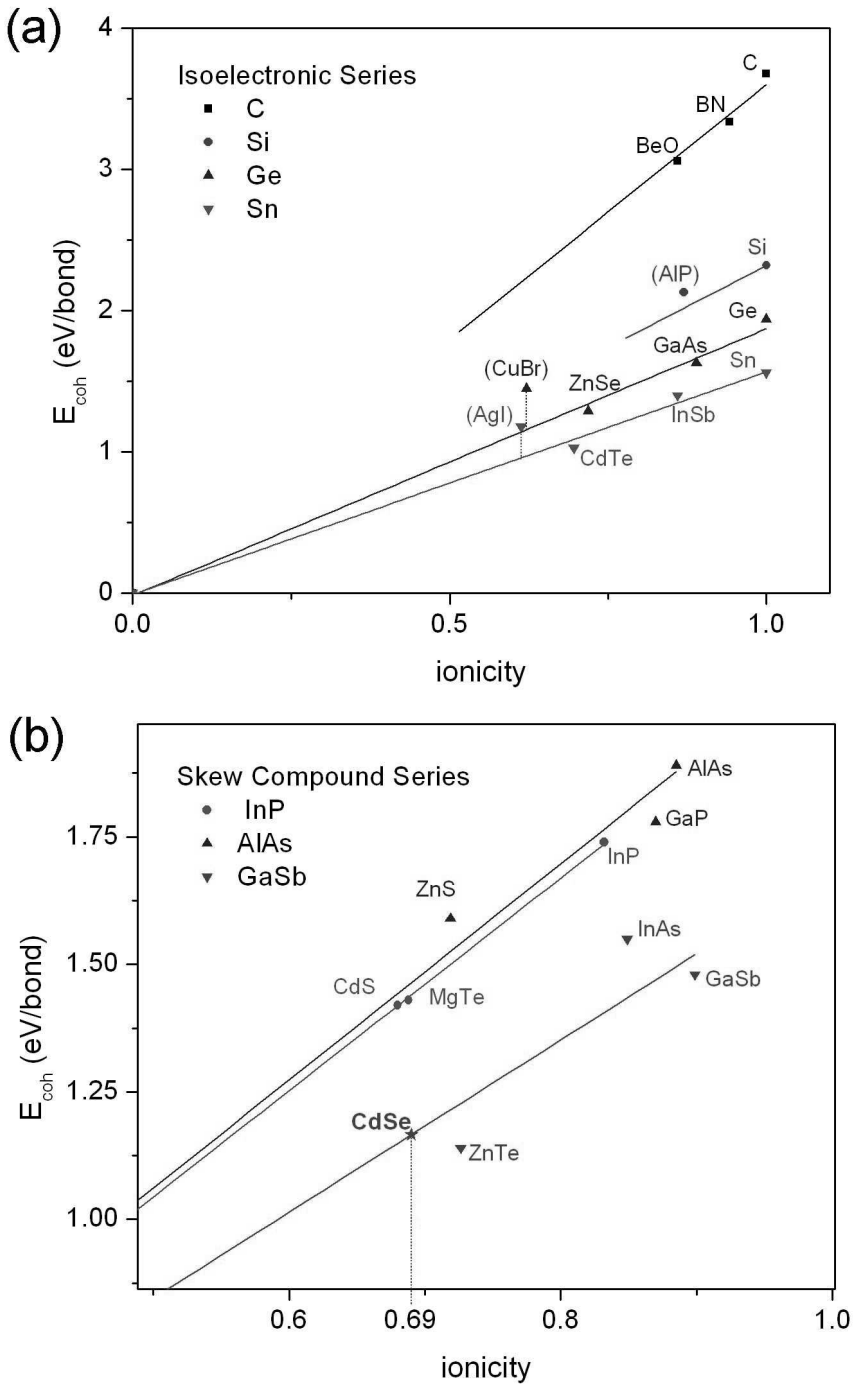

Figure 6.11: Plots showing the cohesive energies of the (a) isoelectronic and (b) skew compound series of semiconductors. Each series is matched with a linear fit that terminates at the origin. An estimated cohesive energy for CdSe is found with this fit to be 1.16 eV.

of the crystal will reduce.

The rate of mass-loss of the Cd atoms during damage can be modeled using a simple model first introduced by Medlin and Howitt [5] and generalized to include multicomponent crystals by Muller and Silcox [6] and used by Mkhoyan and Silcox [7] to estimate the vacancy-enhanced displacement cross-section for InN. The simple model assumes only forward scattering of crystal atoms by the incident electron in the area of a crystal lattice illuminated by the electron beam with j layers of crystal and N lattice sites per layer. B^i_j is the number of atoms of type i in layer j, and the probability that a lattice spacing in layer j of the crystal occupied by atom species j is vacant is given by,

$$f_j = 1 - \frac{1}{N}\sum_i B^i_j. \tag{6.4}$$

It is assumed the distribution of vacancies is random. The probability that any given atom is found on the surface is calculated by

$$s_j = \prod_{k=0}^{j-1} f_j, \tag{6.5}$$

and therefore the number of surface atoms of type i in layer j can be counted:

$$S^i_j = B^i_j \cdot s_j. \tag{6.6}$$

For an atom of type i with a cross-section of surface sputtering of σ^i_s and a cross-section for vacancy-enhanced displacement of σ^i_{ved} and for an incident beam current density of J, the rate of sputtering of atoms of type i from layer j is calculated by

$$\frac{dN_{sur}}{dt} = -J \cdot \sigma^i_s \cdot S^i_j. \tag{6.7}$$

The rate of the number of atoms of type i knocked from layer j into the next layer, $j-1$, is given by

$$\frac{dN^-_{vac}}{dt} = -J \cdot \left[\sigma^i_b \left(B^i_j - S^i_j\right) f_{j-1}\right]. \tag{6.8}$$

The rate of the number of atoms of type i knocked into layer j from the previous layer, $j+1$, is given by

$$\frac{dN^{+}_{vac}}{dt} = J \cdot \left[\sigma^{i}_{b}\left(B^{i}_{j+1} - S^{i}_{j+1}\right) f_{j}\right]. \tag{6.9}$$

Combining the rates of mass-loss described in Equations (6.7) through (6.9) gives a set of coupled differential equations describing the total lattice occupation rate of change in layer j of the crystal.

$$\frac{dN^{i}_{j}}{dt} = J \cdot \left\{\sigma^{i}_{ved}\left[\left(N^{i}_{j+1} - S^{i}_{j+1}\right) f_{j} - \left(N^{i}_{j} - S^{i}_{j}\right) f_{j-1}\right] - \sigma^{i}_{s} S^{i}_{j}\right\} \tag{6.10}$$

To calculate the total rate of mass-loss from the CdSe nanocrystals used in this experiment, the values for the current density, J, the total number of lattice sites per layer, N, and the number of layers, j, need to be measured and/or estimated.

The current density for the 0.2 nm, 100 keV electron beam from the VG STEM was measured by removing the sample from the column and allowing the beam to pass through the column unimpeded until it hit the side wall of the drift tube located at the end of the column. The drift tube coils had been turned off for this measurement, allowing the electrons to travel in a straight line and strike the side of the curved tube instead of the typical curved trajectory through the magnetic fields into the detectors. The current hitting the drift tube side was then measured, giving an accurate measure of the current density for the setting of extraction voltage and lens settings used in this experiment. A plot of the measured current hitting the drift tube is shown in Figure 6.12 for two separate measurements, and gives an average current of 18 pA. Now, in order to estimate the current density of the damage experiments, the size of the damage spot is measured. Although the beam itself is 0.2 nm in diameter, the diameter of the

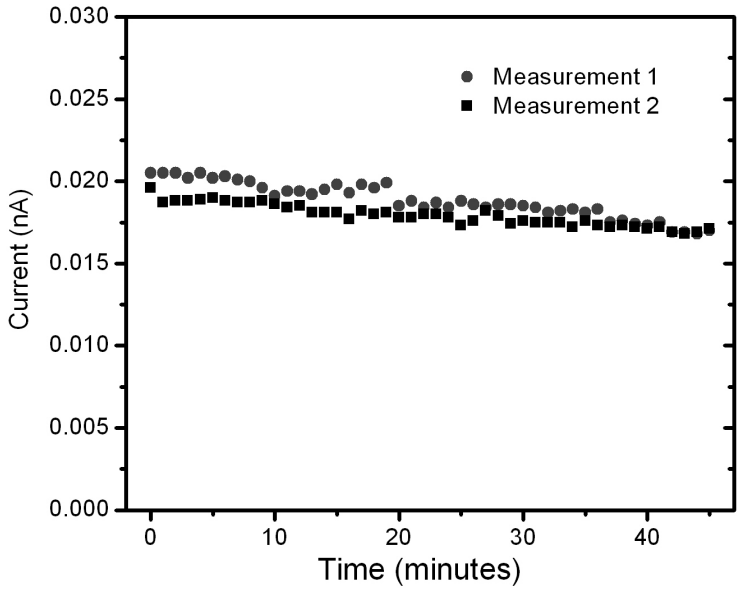

Figure 6.12: Plot of the beam current in VG STEM measured for 45 minutes in two different experiments. Both measurements show a slow decline of current over time with an average beam current density of 18 pA.

damage area will be larger due to beam spreading and drift. Using a larger area approximated by the damage spot areas in CdSe rods, the beam current density was estimated to be $9x10^{21} e/s \cdot cm^2$. Using the density of the wurtzite CdSe structure, the number of lattice sites per layer in the irradiated area was estimated to be $N = 13.46$. To estimate the number of layers, j, the thickness of the quantum rods can be used. For the damage measurements listed previously, the thickness of the quantum rods ranged from 4 to 6 nm.

The plot shown in Figure 6.13 demonstrates how close the simple model predicts the experimental mass-loss for the Cd atoms sputtered from the surface of the quantum rods. The theory was very sensitive to the surface sputtering cross-section, σ_s^{Cd}, and the thickness values. Referring to the earlier calculations

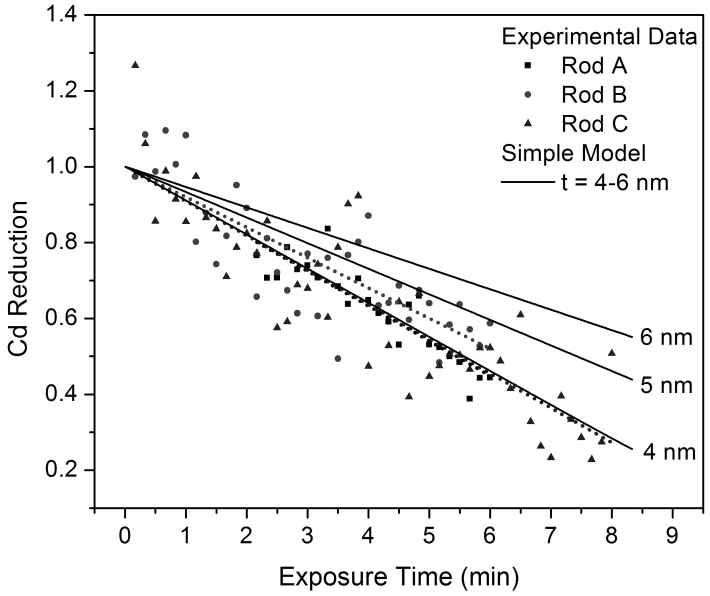

Figure 6.13: Plot showing the calculated decay of Cd using the simple model overlaid on the experimental data of Cd decay shown in Figure 6.7. The simple model is calculated for three thicknesses and can be compared with the linear fits for the three experimental data sets in corresponding color. The slopes of Rods A and C match very well with t=40 Å, and the slope of Rod B is between the slopes of t= 40 Å and 50 Å.

of the Mott cross-sections shown in Figure 6.10, it is unlikely the surface cross-section for Cd will be very large. Therefore, an estimated value for σ_s^{Cd} was chosen to be 1 barn, and the diameters of the experimental quantum rods used were 4, 5 and 6 nm. It can be seen that these estimated values give a very close match to the experimental rate of mass-loss.

The other parameter of the simple model that also had to be estimated was the vacancy-enhanced displacement cross-section, σ_{ved}^{Cd}. The simple model was found to be very insensitive to variations in this parameter, and a value range from 0 to 1000 barns for σ_{ved}^{Cd} yielded insignificant changes in the slope or shape of the Cd mass-loss rate.

6.4 Conclusions

Electron beam damage of nanoparticles is a pernicious problem, and has been shown to be detectable by both ADF STEM images and core-loss EELS integration. The EELS core-loss integration was used to show the loss of Cd from the CdSe nanoparticles when the nanoparticle was not being protected by the carbon substrate. This damage has also been shown to be reduced and the Cd loss, as measured by the core-loss EELS, almost eliminated by arranging the sample with the carbon substrate at the exit surface of the beam, creating a protective carbon coating. This orientation of the sample to the substrate also occasioned a white spot larger than the inter-atomic distance in the irradiated area. This white spot is believed to be beam scattering from the damaged crystal.

The stability of the nanodiffraction pattern upon damage was shown also, by demonstrating that a nanodiffraction pattern from a spot on a CdSe nanoparticle remains largely unchanged with a minute and a half of beam irradiation. This shows that previous (and future) nanodiffraction studies of nanoparticles are trustworthy measures of the crystal structure of the area measured, and any changes in the patterns are not due to a progressively damaged specimen.

Calculations for the threshold energy of bulk sputtering of CdSe show that neither Cd nor Se should be removed from a site in the bulk of the crystal due to the high cohesive energy. However, the calculations for the threshold energy of surface sputtering shows that Se should be easily sputtered from the surface of CdSe, but the Cd Mott cross-section becomes non-zero very close to the energy of the incident, 100 keV electrons. This demonstrates that the cohesive energy of Cd surface atoms needs to be understood more accurately to put a better value

on the Mott cross-sections.

The binding energy for CdSe used for the Mott cross-section is estimated using both the heat of sublimation as a guide and the predictable nature of the cohesive energies of semiconductors. Using a simple model of mass-loss from a sputtered sample, an estimated value for the Cd surface cross-section of 1 barn gives a close match to the experimental plots of mass-loss gathered from Cd core-loss EELS on CdSe nanoparticles.

The uncertainty of the binding energy of the Cd surface atoms is further exacerbated by the surface relaxation that is seen in very small particles of CdSe. Therefore, all that can be concluded about the surface binding energy of Cd in CdSe nanocrystals is that it is sufficiently low to allow surface sputtering, as observed by the STEM core-loss EELS measurements in this study.

BIBLIOGRAPHY

[1] Z. Yu, M.A. Hahn, J. Calcines, T.D. Krauss, J. Silcox, App. Phys. Lett. **86**, 013101 (2005).

[2] Z. Yu, PhD Thesis, Cornell University, Ithaca NY 2004.

[3] V.D. Blank, B.A. Kulnitskiy, I.A. Perezhogin, Y.L. Alshevskiy and N.V. Kazennov, Sci. Technol. Adv. Mater. **10**, 015004 (2009).

[4] N.J. Zaluzec and J.F. Mansfield, 1986, *Proceedings of the 44th Annual Meeting of Electron Microsopy Society of America*, edited by G.W. Bailey (San Francisco Press), p. 708.

[5] D.L. Medlin and D.G. Howitt, Phil. Mag. Lett. **64**, 133 (1991).

[6] D.A. Muller and J. Silcox, Phil. Mag. A **71**, 1375 (1995).

[7] K.A. Mkhoyan and J. Silcox, Appl. Phys. Lett. **82**, 859 (2003).

[8] C.R. Bradley and N.J. Zaluzec, *Proc of the NSF/CNRS Workshop on "Electron-Beam Induced Spectroscopies at Very High Spatial Resolution"*, Aussois France, Feb 28-March 5 1988, Eds. C. Colliex and M. Isaacson, pp 466-470.

[9] C.R. Bradley, *Calculations of Atomic Sputtering and Displacement Cross-Sections in Solid Elements by Electrons with Energies from Threshold to 1.5 MeV*, Report No. ANL-88-48, 1988.

[10] K.-H. Hellwege, *Landolt-Börnstein: Numerical Data and Functional Relationships in Science and Technology, Group III: Crystal and Solid State Physics*, Volume 17, Subvolume b (Springer-Verlag Berlin, Heidelberg, New York) p 202, 1982.

[11] W.A. Harrison, *Electronic Structure and the Properties of Solids*, (W.H. Freeman and Company, San Francisco) pp 167-179, 1980.

[12] W.J. Huang, R. Sun, J. Tao, L.D. Menard, R.G. Nuzzo and J.M. Zuo, Nature Mat. **7**, 308 (2008).

[13] A. Puzder, A.J. Williamson, F. Gygi and G. Galli, Phys. Rev. Lett. **92**, 27401 (2004).

[14] S.W.H. Eijt, A. Van Veen, H. Schut, P.E. Mijnarends, A.B. Denison, B. Barbiellini and A. Bansil, Nature Mat. **5**, 23 (2006).

[15] W.H. Qi and M.P. Wang, Jour. of Chem. Sci. Lett. **21**, 1743 (2002).

[16] H.K. Kim, S.H. Huh, J.W. Park, J.W. Jeong and G.H. Lee, Chem. Phys. Lett. **354**, 165 (2002).

CHAPTER 7

USING ADF TO MEASURE THICKNESS OF QUANTUM PARTICLES

7.1 Introduction

Understanding and studying the shape of colloidally grown quantum nanoparticles has been an important aspect of nanoparticle research because the most interesting properties of these small particles are highly shape-dependent [1, 2]. Though the shape of these nanoparticles is so important, it has been difficult to actually measure. The most popular and powerful tools to image these particles are the TEM and the STEM, but the images obtained from both of these instruments are created from electrons passing through the sample and are therefore projections of the shape of the particles. Projections provide information readily about two dimensions of the shape of an object, but the third dimension is missing. One promising way of obtaining information about all three dimensions of the particle is electron tomography [3], but this technique requires many images of the particle at different angles and intensive computer analysis to reconstruct the images to a three-dimensional model. This study points out that the use of annular dark field (ADF) images obtained using STEM can be used to infer information about the third dimension quickly and with very little computer analysis. The use of ADF image intensities to understand the thickness of nanoparticles has been explored previously by Kadavanich et al. [4] on CdSe quantum dots (QDs). Kadavanich reported the thickness profile of a single QD by using the intensity profiles from a heavily filtered ADF image, and found it to have similarities to thickness profiles from a model, faceted QD. The current study shows that raw, unfiltered images can give information about the

thickness and, therefore to some degree, the shape of the particle. This method was used successfully by Li et al. [5] to show the size, three-dimensional shape, orientation and atomic arrangement of gold nanoclusters. Both the simple kinematic thickness calculation and the more elaborate multislice simulations are used by Li, et al. to confirm the usefulness of the ADF images to predict shape. These calculations are also both used and discussed in this chapter.

Annular dark field images have been discussed previously in some detail, and it has been shown that the contrast and intensity in the ADF images is mainly dependent upon the mass of the scattering atom and the thickness of the sample. This feature of the ADF images has been exploited mostly with Z-contrast studies, but the thickness-dependence of the intensity of the image is an ideal way to obtain shape information for small, thin, single-crystal samples of relatively uniform composition such as nanoparticles.

7.2 Theory and Simulation

The majority of the nanoparticles examined in this study were colloidal CdSe quantum rods (QRs) synthesized by chemist collaborators discussed in Chapter 2.5. The average diameter of the QRs was 7 nm (± 1 nm) with an average aspect ratio of 1:4. Assuming a near-cylindrical cross-section, the small diameters of the QRs suggest that the maximum thickness traversed by the electrons in the microscope is about 7nm.

Given the incoherence of the ADF signal, we can intuitively expect that it would initially depend on the amount of material impacted by the electron beam. For a very thin, chemically homogeneous sample, this translates to a

linear dependence on the thickness, also described as the kinematic theory for scattering electrons. More explicitly, the intensity collected by the ADF detector follows the relation

$$I_{ADF} = I_0 \eta_{DET} \frac{\sigma_{EL}}{\sigma_{probe}} \times N \tag{7.1}$$

where I_0 is the intensity of the incident probe, σ_{EL} is the elastic scattering cross-section, η_{DET} is the fraction of elastically scattered electrons collected by the ADF detector, and N is the number of atoms illuminated by the probe of area σ_{probe}. In the single-scattering limit, $N = nt\sigma_{probe}$, where n is the atomic number density of the film of thickness, t. As electrons enter the crystal, the dynamics of the electron wave packets are impacted by coherent elastic interaction with the crystal and modifications can be expected. The short longitudinal coherence length enforced by the detector dimensions [9] can generate an additional limiting square dependence on t but this is usually small.

If linear dependence does indeed dominate then this becomes a valuable approximation in the rapid exploration of nanoparticle shapes. Assuming chemical homogeneity, the thickness across the diameter of a QR of cylindrical cross-section would follow the function,

$$t = \sqrt{R^2 - x^2}. \tag{7.2}$$

where R is the radius of the cylinder and x the location across the width relative to the center of the cylinder. Similarly, Figure 2.2 (b) of Chapter 2 shows a plot of the thickness of a hollow sphere, indicating the thickness profile that would occur from the shell material of a uniformly shelled QD. Further simple, kinematic models can be developed for faceted cylindrical rods using faceting configurations typical for small CdSe particles governed by the hexagonal crystal structure and the lattice constants of CdSe.

This simple kinematic thickness model was used also by Lozano-Perez et al. in an interesting way to confirm the spherical shape of Cu-rich particles in a ferritic steel matrix using the intensity of energy-filtered TEM images. [10]

In addition to simple kinematic thickness models, more sophisticated descriptions of the intensity of the ADF images were developed using multislice simulations described previously in Chapter 2.4 of this thesis as well as in literature [11, 12]. This method considers the vast majority of effects upon the transmitted electrons, including dynamical scattering, and simulates an ADF image resulting from the electrons scattered into angles between 54 and 300 mrad. First, the integrated intensity of the scattered electrons through successive layers of a large, bulk CdSe crystal was simulated. Thermal vibrations of the atom positions were included by using the frozen-phonon method [13] averaged over 16 phonon configurations. The resulting curves for the ADF image intensity of the two on-axis orientations existing perpendicular to the c-axis, the $[\bar{1}100]$ and $[\bar{2}110]$ orientations, are given in Figure 7.1.

Though these curves do not give a strictly linear relationship between thickness and intensity of the ADF signal, in the region representative of the thicknesses found in our QRs (< 8 nm) it is adequate for a first approximation. In further simulations, a large crystal with the size and shape of the CdSe QRs was modeled and oriented in the $[\bar{1}100]$ orientation and a simulated electron probe was transmitted through a the modeled QR using the multislice and the frozen-phonon method. A linescan across the width of the simulated QR segment gives an intensity profile that is compared with the profile of the known thickness of the QR in Figure 7.2. The near fit with the average intensity demonstrates the validity of the assumption of the linearity of intensity vs. thickness in

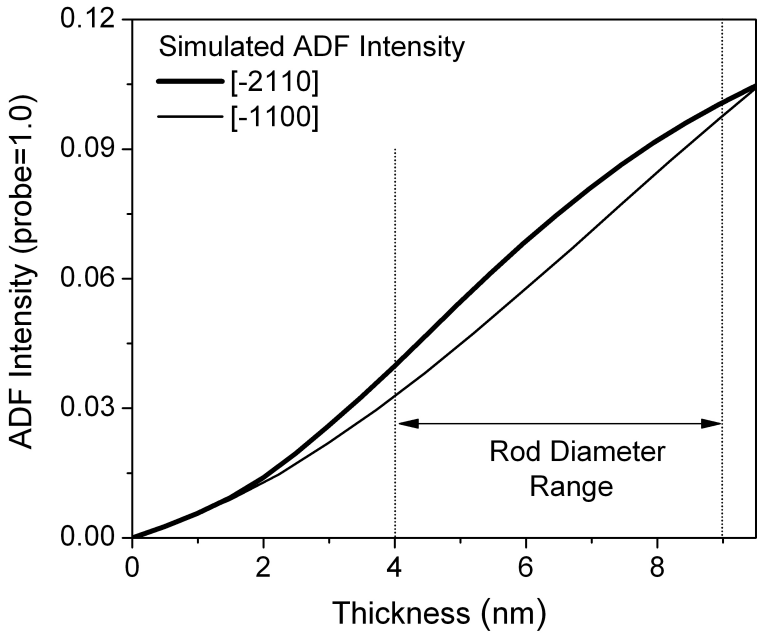

Figure 7.1: Multislice simulation of ADF intensity of electrons as a function of thickness through bulk CdSe for the two axis positions, [$\bar{1}$100] and [$\bar{2}$110] .

the ADF images of the QR. The inset of Figure 7.2 shows a simulated QR image composed of multiple units of the simulated QR segment.

7.3 STEM Measurements

The CdSe QR specimens were prepared for STEM observation by dropping a small amount of the QRs suspended in hexane (1 mL) onto an ultra-thin (about 3-5 nm) carbon film stretched on a copper grid (Ted Pella Inc.). ADF images of these QRs were taken using the Cornell VG HB501 100 kV STEM and were acquired with a single-electron-sensitive ADF detector with an angular collection range of 54 to 330 mrads. The intensity of the cross-section of the QRs is

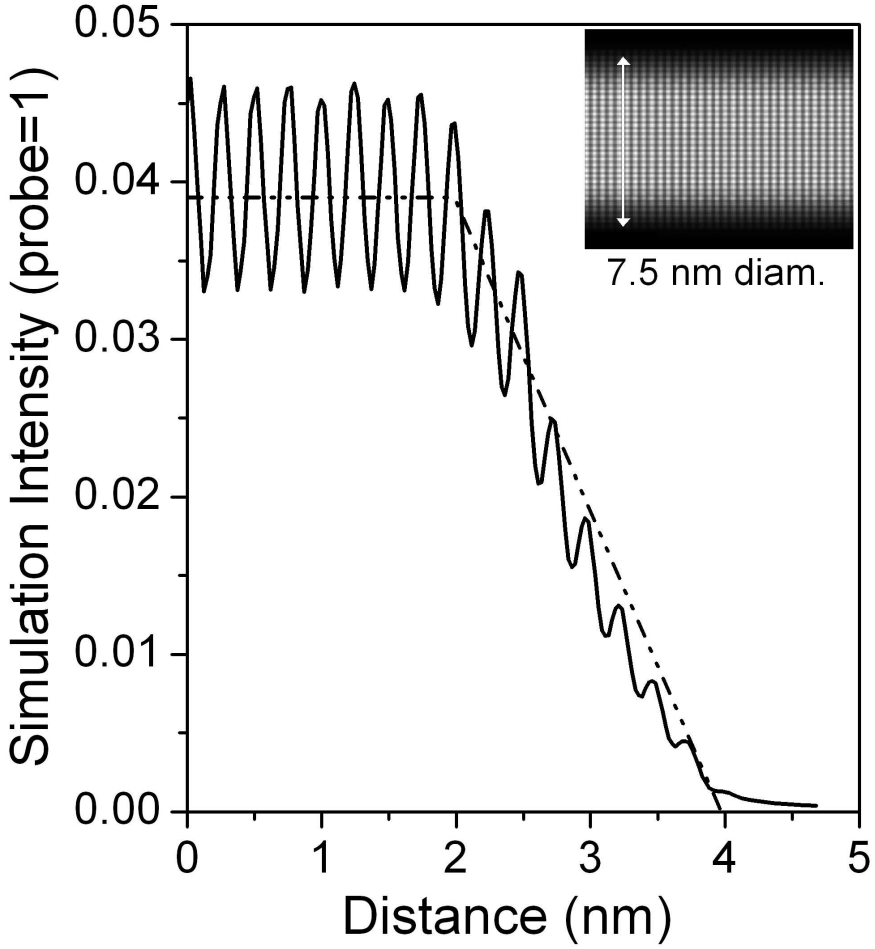

Figure 7.2: Intensity profile (solid line) taken from a simulated ADF intensity image of a rod-shaped model (inset). Also on the graph is the thickness profile of the faceted cross-section of the model QR (dashed line). Inset: Image collage of complete simulated QR created using multiple units of the simulated QR segment.

obtained from the ADF images by taking linescans of the ADF signal across the width of various QRs.

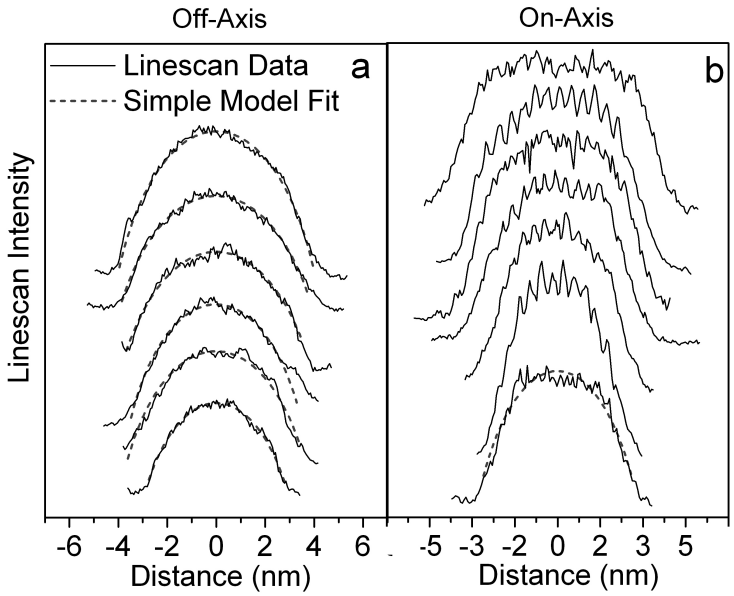

Figure 7.3: Various intensity linescans of ADF-STEM image of off-axis and on-axis CdSe QRs.(a) Linescans of off-axis QR images where the linescans (solid) are fitted with a simple round thickness profile (dashed). (b) Linescans of QR images while in the [$\bar{2}$110] orientation. One linescan is fitted with the simple round thickness model (dashed).

7.4 Results and Discussion

Linescans across the width of various off-axis QRs are shown in Figure 7.3a, along with the simple kinematic thickness model for a round cylinder whose function is given in Equation 2. This round simple model fits very well with these off-axis intensity profiles, but when an intensity linescan is taken from an on-axis QR things are different. Figure 7.3 (b) shows intensity linescans from ADF images of QRs all in the [$\bar{2}$110] orientation as identified by the characteristic two-dimensional lattice image. These linescans show often sharply planar features that suggest faceting of the QRs. When these highly planar linescans

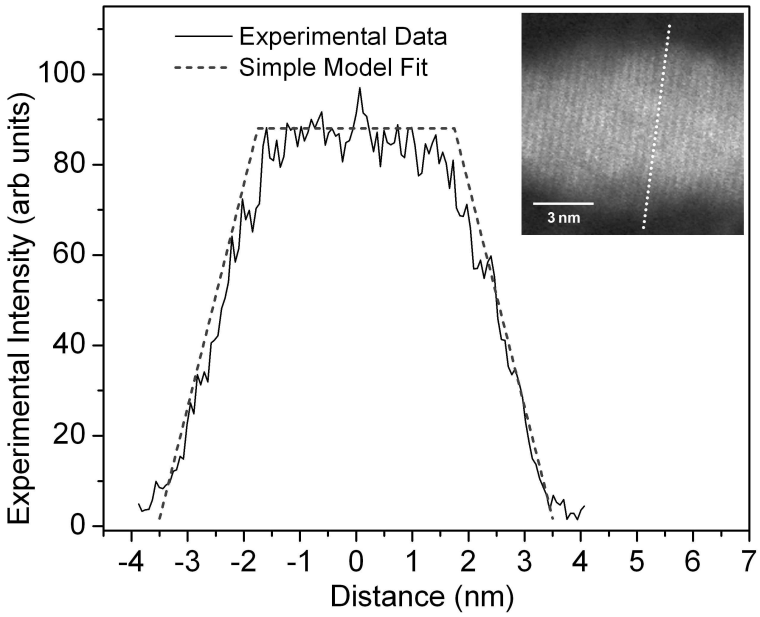

Figure 7.4: (inset) ADF image of a CdSe QR close to the [$\bar{1}$100] orientation. (graph) The linescan of the intensity across the QR (light solid). The thickness profile model for a hexagonal faceted QR (dashed) is overlaid on the linescan. In this and all subsequent ADF linescan plots, the carbon background intensity has been subtracted.

are fitted with the round thickness model, as in the bottom linescan of Figure 7.3 (b) there are many areas of discrepancy in the fit.

Figure 7.4 shows the intensity linescan from a QR that is close to an on-axis position. The ADF image of the QR is shown in the inset of Figure 7.4, and a nanodiffraction pattern (not shown) taken of the QR near the location of the linescan show that this QR is close to the [$\bar{1}$100] orientation. A simple round thickness profile would not adequately fit this intensity profile any better than the faceted QR in Figure 7.3 (b), but a faceted thickness profile, shown with the intensity plot, fits remarkably well.

It is not surprising that on-axis QRs display evidence of faceting more readily than the off-axis QRs when one looks at the thickness profiles of a faceted shape tilted at different angles, as shown in Figure 7.5. Parts a and c of Figure 7.5 show on-axis thickness profiles, elements of which can be seen in various intensity profiles of the on-axis QRs in Figure 7.3 (b). Part b of Figure 7.5, however, shows an off-axis QR tilted 15° from the on-axis positions. This thickness profile is less angular than the two on-axis profiles, and itself could be fitted fairly well with the round thickness profile. This series of thickness profiles shown in Figure 7.5 helps explain why on-axis, faceted QRs require a faceted model to be fitted accurately while off-axis, faceted QRs can be fitted well with a round thickness profile especially when one considers that actual faceted QRs will not be free from additional, often inhomogeneous intensity variations due to irregularities on the surface, organic surface ligands, etc.

In this study, simulated QR intensities are also compared with experimental intensities. Figure 7.6 shows the experimental linescan of Figure 7.4 graphed with the simulated linescan. The tight fit in all regions shows that the multislice simulation gives an accurate representation of the ADF intensity of an experimental image. The small peaks in intensity up the side of the experimental intensity linescan match well with those up the side of the simulated intensity linescan. The peaks in the simulated linescan are due to the appearance of successively thicker columns of atoms, and thus the small peaks in the experimental linescan must come from the same source. This intensity resolution of the different thicknesses of columns suggests that it may be possible to link certain intensities in the ADF image with a unit of thickness, and with care one may be able to link the difference in intensity between atomic columns in the QR image to the addition or lack of a single atom, as was claimed by Kadavanich et al. [4].

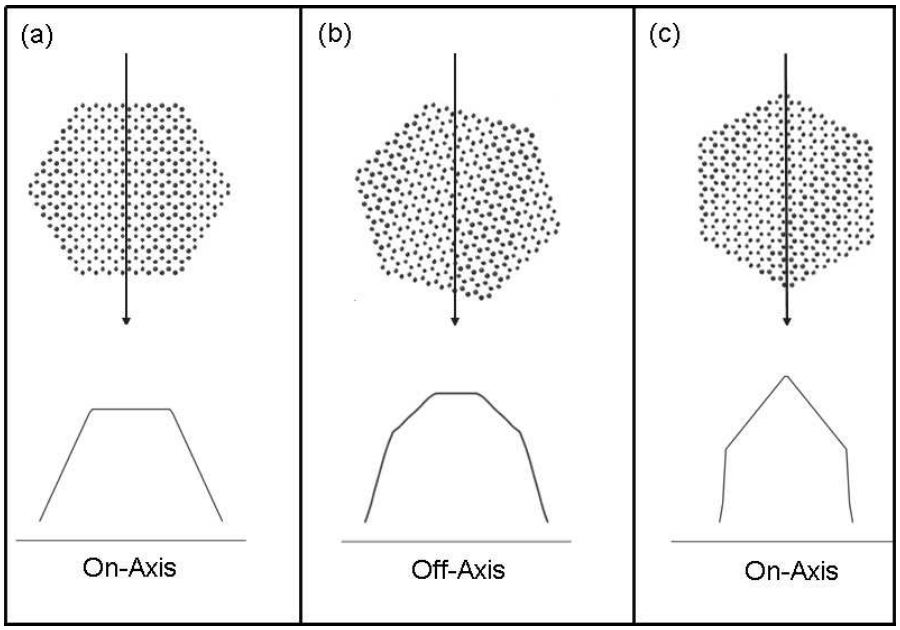

Figure 7.5: The cross-section of a faceted CdSe QR is shown in three orientations along with the projected thickness profile of each. The orientation of the simulated rod, as it relates to the electron beam direction (arrow) are the $[\bar{1}100]$ (a) resembling a mesa, $[\bar{2}110]$ (c) resembling a house, and 15 ° between the two (b). However, because of the number of ways that atoms can facet themselves around the rod, both the $[\bar{1}100]$ and the $[\bar{2}110]$ orientations can display the two characteristic "mesa" and "house" on-axis cross-section shapes.

One notable difference between the simulated and experimental intensity linescans is the contrast at the top of the linescan. The simulated linescan is showing the contrast between columns of atoms and spaces between the columns. The major reasons for this marked contrast difference between experiment and simulation are threefold. First, the experimental linescan is taken from a QR that is tilted a bit off-axis and therefore the atomic columns are not well resolved. Second, there is a large background intensity in the experimental intensity due to the substrate that is not present in the simulated intensity. Third is the presence of Stobbs factor [14, 15]. The Stobbs factor is the name given to the large factor of contrast reduction, about 3-5 times, found between simulated and experimental images. Several factors may contribute to this contrast reduction in

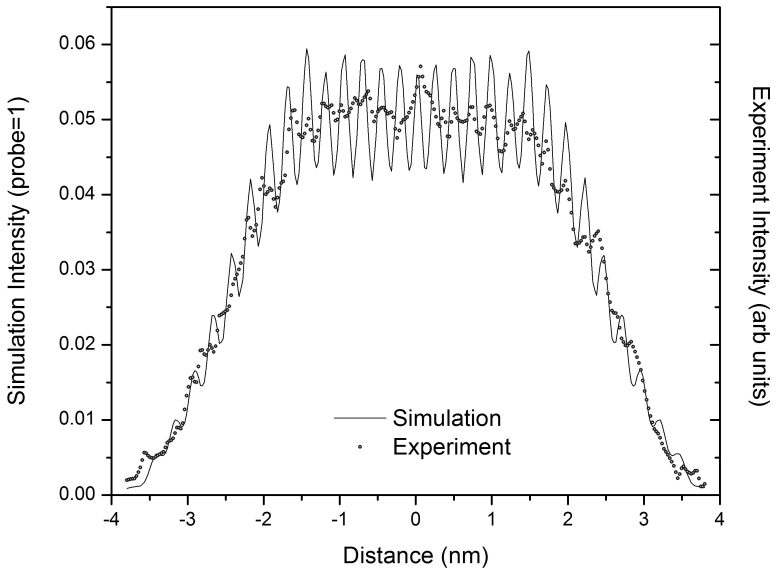

Figure 7.6: The intensity linescans of the simulated (solid) and the experimental (circles) ADF image (data previously shown in Figure 7.4) are plotted together showing the close prediction given by the multislice method for intensity vs. thickness.

STEM images, three of which have been discussed earlier in this thesis: inelastic scattering [17], small sample tilts [18], and the presence of amorphous material [19].

The ability to understand the shape of a nanoparticle using the ADF intensity is further examined in the next two images. Figure 7.7 shows multiple linescans from a single CdSe QR in the [$\bar{2}$110] orientation. Each subsequent linescan, from left to right, is taken two atomic layers away from the one before it, and is taken from the area between the atomic columns of the layers as to reduce the high intensity fluctuations that come from each column and allow us to concentrate more upon the general trend of the intensity variation. The left-most linescans in the plot show the faceting one would expect from the [$\bar{2}$110] orientation of

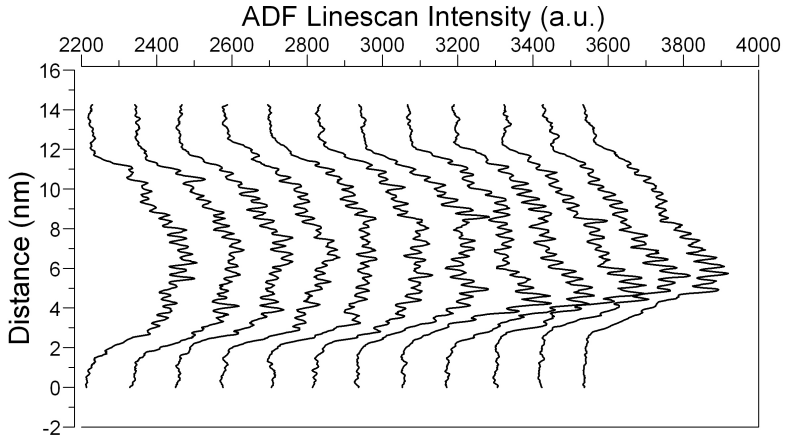

Figure 7.7: Intensity linescans across a section of a CdSe QR in the [$\bar{2}$110] orientation. Linescans are taken between the atomic columns at every second atomic layer (for plot clarity) along a portion of the length of the QR.

wurtzite, but as one travels along the QR there appears a major increase in intensity on one side of the QR that causes the thickness profile to deviate from the expected shape. This likely indicates a sudden increase of material creating something like a crystal spur on the side of the QR. One can imagine that this spur may ultimately cause electronic surface anomalies such as charge trap sites or polarization due to the anisotropy of the wurtzite crystal.

Another example of using ADF images to discover the shape of a nanoparticle is given in Figure 7.8. This QD is taken from a sample of CdSe QDs capped with a ZnS capping layer. The QD appears to be in the [100] orientation, and a linescan taken across the QD reveals it to be faceted with a shape common to a crystal oriented in the ”house” orientation, as seen in Figure 7.5 (c) and also in Figure 7.7. In this QD, however, there is a gradual increase in intensity on the side of the QD not obscured by a clump of extraneous material. This grad-

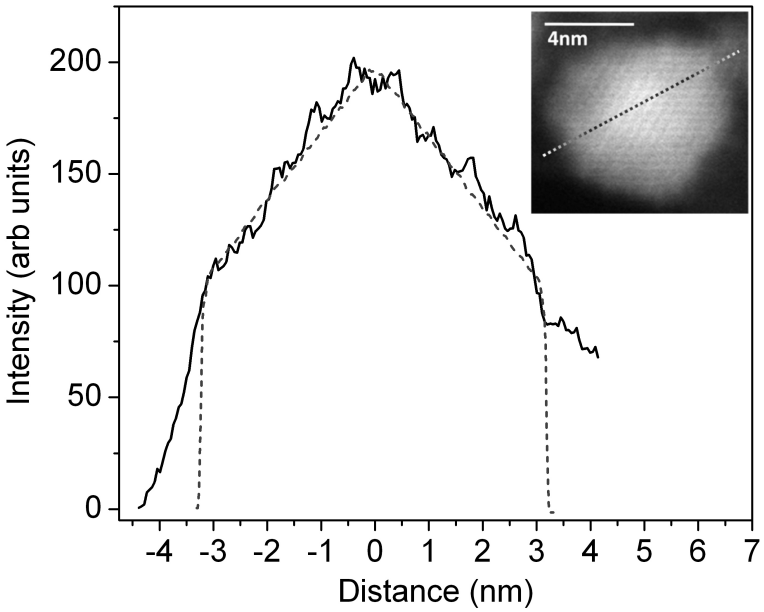

Figure 7.8: Plot of the intensity linescan across a CdSe/ZnS QD (solid) compared with a thickness profile for a wurtzite crystal in the [$\bar{2}$110] (″house″) orientation (dash). Inset: The ADF image with a dotted line indicating whence the linescan was taken.

ual increase does not match the characteristic sudden increase for the ″house″ faceting. This could be due to the presence of a shell material on the surface of the QD which would cause a deviation from the linear relationship between intensity and thickness we have come to expect from a homogeneous crystal material. It could also be due to inhomogeneous distribution of surface material or organic ligands.

7.5 Conclusions

Multislice simulations confirm that the intensity of ADF images of small, single-crystal nanoparticles can be used to interpret the thickness and the shape of the particles. Faceting of quantum rods and dots has been detected, and in some cases the intensity profiles of faceted particles can be quickly translated via a thickness profile to a particular shape. Those ADF images of quantum particles that do not show ideal faceting behavior can be used to assist identification of deviation from the ideal and thereby, to some degree, help understand the growth or shelling abnormalities that may exist in the sample.

BIBLIOGRAPHY

[1] J. Hu, L. Li, W. Yang, L. Manna, L. Wang, A. P. Alivisatos, Science, **292**, 2060 (2001).

[2] S. Kan, T. Mokari, E. Rothenberg, U. Banin, Nature Mat., **2**, 155 (2003).

[3] P.A. Midgley, M. Weyland, Ultramicroscopy, **96**, 413 (2003).

[4] A. V. Kadavanich, T. C. Kippeny, M. M. Eriwin, S. J.Pennycook, S. J. Rosenthal, J. Phys. Chem. B, **105**, 361 (2001).

[5] Z.Y. Li, N.P. Young, M. DiVece, S. Palomba, R.E. Palmer, A.L. Bleloch, B.C. Curley, R.L. Johnston, J. Jiang and J. Yuan, Nature **451**, 46-48 (2007).

[6] X. Peng, L. Manna, W. Yang, J. Wickham, E. Scher, A.Kadavanich, A. P. Alivisatos, Nature (London) **404**, 59 (2000).

[7] Z. A. Peng, X. Peng, J. Am. Chem. Soc., **123**, 1389 (2001).

[8] Z. A. Peng, X. Peng, J. Am. Chem. Soc., **124**, 3343, (2002).

[9] M.M.J. Treacy, J.M. Gibson, Ultramicroscopy, **52**, 31 (1993).

[10] S. Lozano-Perez, J.M. Titchmarsh and M.L. Jenkins, Ultramicroscopy, **106**, 75-91 (2006).

[11] J. M. Cowley, A. F. Moodie, Acta Crystal., **10**, 609 (1957).

[12] E. J. Kirkland, R. F. Loane, J. Silcox, Ultramicroscopy, **23**, 77 (1987).

[13] R. F. Loane, P. Xu, J. Silcox, Acta Crystal. A, **47**, 267 (1991).

[14] C. B. Boothroyd, Journal of Microscopy, **190**, 99 (1998).

[15] A. Howie, Ultramicroscopy, **98**, 73 (2004).

[16] M. Isaacson, D. Kopf, M. Ohtsuki, M. Utlaut, Ultramicroscopy, **4**, 101 (1979).

[17] K. A. Mkhoyan, S. E. Maccagnano-Zacher, M. G. Thomas, J. Silcox, Phys. Rev. Lett. **100**, 025503-(1-4) (2008).

[18] S. E. Maccagnano-Zacher, K. A. Mkhoyan, E. J. Kirkland, J. Silcox, Ultramicroscopy **108**, 718-726 (2007).

[19] K. A. Mkhoyan, S. E. Maccagnano-Zacher, E. J. Kirkland, J. Silcox, Ultramicroscopy **108**, 791-803 (2008).

[20] S. Amelinckx, R. Gevers, J. Van Landuyt, *Diffraction and Imaging Techniques in Material Science*, (North-Holland, Amsterdam) 2^{nd} Rev. Ed. pp 24-26, 1978.

CHAPTER 8

QUANTUM ROD GROWTH BY ORIENTED ATTACHMENT

8.1 Introduction

The current theory of colloidally-grown quantum dot growth relies upon the even buildup of new material upon each different face of the small, seed particle that appears in the hot (above 300 degrees C) liquid surfactant (90% trioctylphosphine oxide (TOPO)). This growth is believed to be controlled by the quantity and proportion of precursors and the temperature of the growth solution. In the case of CdSe colloidal nanoparticles, quantum rods (QRs) are encouraged to grow in the solution from dots that have reached a size that is close to the desired rod diameter. At this point, small amounts of phosphonic acids are added to the solution and high-aspect-ratio nanocrystals are seen to grow.

The proposed growth mechanism is that, with the addition of the phosphonic acids, only one face of the CdSe wurtzite structure becomes a favorable growth face with all others remaining stable in the solution [1]. The stability comes from the passivation of the surface bonds of the atoms due to the organic surfactants. The side surfaces of the CdSe wurtzite nanocrystals have an equal distribution of Cd and Se atoms and can be passivated by the either the TOPO or the phosphonic acids and therefore resist any additional atoms bonding to these surfaces. However, the two end faces, (001) and $(00\bar{1})$, are either a layer of Se atoms which are anionic and are only weakly passivated by the surfactant, or a layer of Cd atoms. Weakly passivated bonds encourage crystal growth, so if a face has a layer of only Se a layer of Cd atoms will quickly grow. The two end

faces are not physically the same, however, and this affects the way each face grows upon exposure to the phosphonic acids. On the (001) face, the Cd layer has only one dangling bond, which is quickly and thoroughly passivated by organic ligands. This drastically slows the growth of this face. The (00$\bar{1}$) face, however, has a Cd layer with three dangling bonds. Because of steric effects and the sheer number of dangling bonds, these atoms are not quickly and easily passivated by the ligands, and are therefore likely to attach a Se atom, growing the crystal one more layer. This single-face growth pattern would lead one to expect QRs to exhibit single-crystal tendencies, with perhaps an occasional stacking fault along the c-axis. In many samples of QRs, however, this is not the type of crystal observed.

Figure 8.1 shows a QR grown according to standard preparation techniques. It can be seen in this image that the QR is not a single-crystal at all, but has many changes in the appearance of the crystal lattice along the length. Rods such as this one show that there must be more to the growth mechanism than just the one proposed above. It has been suggested that in addition to the mechanism described, there is an additional growth of the QRs due to oriented attachment. [2, 3]. Oriented attachment was disussed by Penn and Banfield [4, 5] as it was observed in aggregates of nanocrystalline titania particles coarsening under hydrothermal conditions. The observation of imperfect oriented attachment, or the appearance of defects due to slight misorientations in the attachment interface, was reported by Penn and Banfield in nanocrystalline anatase (TiO2) [6]. Oriented attachment as a growth mechanism in colloidally grown, CdSe nanorods was first reported by Yu, et al. [2], and the material presented in this chapter contributed to the demonstration of the importance of oriented attachment in QRs and was incorporated in Reference [3].

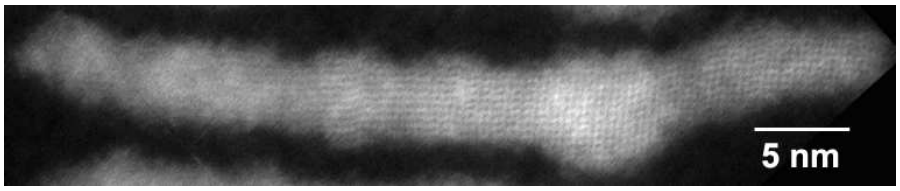

Figure 8.1: ADF image of CdSe QR showing different areas of crystal lattice orientation along its length. The center and right end show the lattice fringes typical with on-axis orientation, whereas the left end shows no lattice fringes.

Oriented attachment would come about by the alignment of the rods in the solution. One proposed mechanism to drive the oriented attachment is a dipolar electric field outside the QR created by net surface charges. These net surface charges are brought about by the spontaneous polarization along the c-axis of the wurtzite crystal, and were estimated by Yu et al. [3] to be between ±0.24 e and ±0.6 e. In a back-of-the-envelope estimate, this charge on oppositely charged, 25 Å diameter QR ends spaced 50 Å apart gives an attractive energy between 8.5 and 53 x10^{-21} J. The low value is comparable with the thermal energy of the hot growth solution, which is 7.9 x10^{-21} J. In this case, therefore, the oriented attachment model is just as favorable as the layer-by-layer diffusion growth.

8.2 Measurements

8.2.1 ADF Images

The physical evidence supporting the occurrence of oriented attachment in CdSe colloidally grown QRs can be found two ways. The first is nanodiffraction along the length of the QR. This was done first very thoroughly by Yu et al. [2, 7]

and is also explored quickly in this thesis in Chapter 6.1. The nanodiffraction measurements found there to be random and non-progressive rotations of the orientation of the crystal along the c-axis of the QR. This matches well with a model that predicts that dots or small rods align end-to-end, along the c-axis, but not necessarily perfectly matching crystal orientation across the join boundary.

High-resolution STEM imaging is also useful in determining if there is any evidence of oriented attachment. By observing high-resolution ADF STEM images, crystal lattice shifts can be seen along the length of a rod. This is not as accurate as measuring the rotation using nanodiffraction, but is a quick, qualitative way of demonstrating the existence of the offset rotations. Another benefit of using ADF STEM high-resolution imaging is that the images are easily interpreted. As discussed in Chapter 7 of this thesis, the intensity of the ADF images increases primarily with thickness and with Z-value and, since the type of material in these QRs is uniform, the Z-contrast will not change noticeably. Therefore, the intensity changes along the QR can be interpreted as occurring mostly from thickness changes. As an example, Figure 8.2 shows high-resolution ADF STEM images of QRs that have drastic changes of diameter along the length of the rod. This change in diameter is evidenced not only by the narrowing of the QR at the attachment spot, but also by the intensity reduction.

In the original observations of oriented attachment by Penn et al. [6, 4], long nanoparticle chains were observed and the individual nanoparticles making up the chain were as easily differentiable from one another as the small QRs in Figure 8.2. These long chains of differentiable particles were also seen in the early stages of nanowire formation from spherical CdTe nanoparticles [8]. On

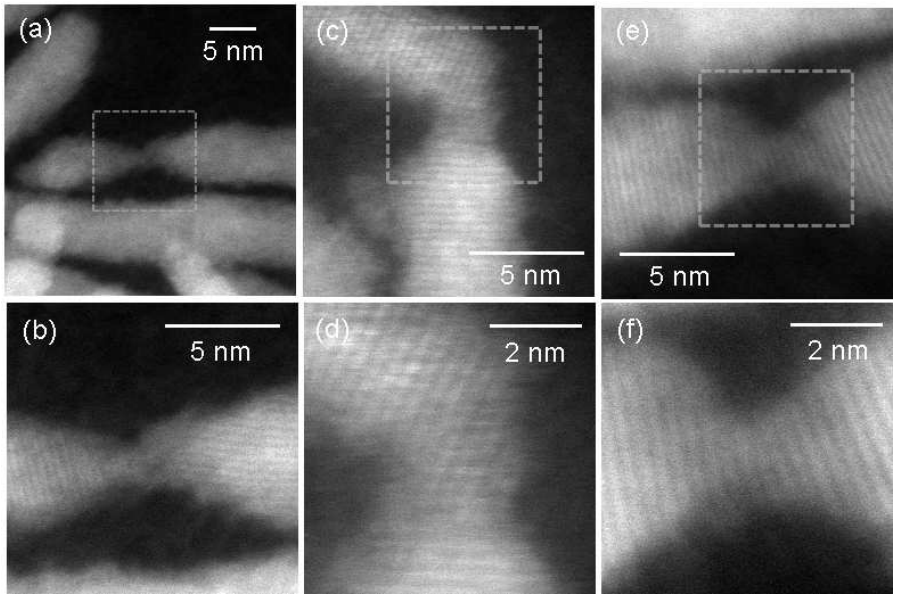

Figure 8.2: ADF images of CdSe QRs that appear to be joined at the tips. (a), (c) and (e) show lower resolution images of the join area and (b), (d) and (f) are higher resolution images of the area in grey boxes in the respective images above. The lattice fringes seem to be continuous through the joins in (d) and (f).

the other hand, in the images of QRs examined for this thesis linear chains of nanoparticles have not been observed. However, this is consistent with the proposal of oriented attachment for numerous reasons. First, the very high aspect ratio QRs studied were typically removed from the growth solution after a fairly long growth time, providing ample time for smaller QRs to completely fuse. Second, QR growth forms only under a high monomer concentration. Since both oriented attachment and diffusion-controlled growth likely coexist and complement each other during the growth process in solution, we can expect that highly reactive monomers can fill in the "gaps" between two oriented QRs efficiently and relatively quickly. One such example is the formation of an elbow between a QR and an attached nanoparticle [2]. Finally, even without the presence of monomers, uniform cylindrical rods of CdTe nanoparticles were formed by simply allowing spherical nanoparticles to coalesce [8]. Thus, similar

behavior from the attachment between two QRs can be expected.

8.2.2 Length Histograms

If oriented attachment is the source of the observed changes in crystal orientation and also thus contributes to the QR growth process, then it can be expected that the QR growth solution should contain smaller as well as larger rods. To study the change of the rods in growth solution as a function of growth time, samples were removed from the hot growth solution at specific times during the growth process, thereby providing a snapshot of the rods up to that point in the growth. These samples were subsequently measured by taking images of them in STEM and examining the appearance of the crystal lattices along the lengths of the QRs to see the uniformity of growth along an individual QR. Low-resolution ADF images were also taken of large rafts of dots to gather statistics about the size and aspect ratio of the samples as a whole. There were four samples from the same growth solution with different growth times compared using STEM. Images were taken of rods grown for 10 minutes, 20 minutes, 45 minutes, and 1 hour. The sample grown for 45 minutes was prepared for STEM a bit differently than the other three samples, which will be discussed later in more detail. Figure 8.3 shows an example of high resolution images taken of each of these samples, giving an idea of the sizes and crystal uniformity of the QRs. The rods grown for 10 and 20 minutes, shown in Figure 8.3 (a) and (b), exhibit chiefly a single-crystal nature with less examples of kinks and elbows in the sample. The rods grown for 45 minutes and 1 hour, shown in Figure 8.3 (c) and (d), both show the kinks common for the previous samples discussed, as well as the crystal lattice changes along the length of the rod. The white arrows

in these two images point out thinner, lower intensity ”necks” in the ADF images that suggest a join between two nanoparticles. The nanoparticles on either side of the neck also show different lattice fringes, which suggests that there is a different crystal orientation between the nanoparticles. Typical sample processing for STEM imaging involves careful removal of the TOPO, which involves precipitating the QRs with a nonsolvent followed by centrifugation and dilution to a density suitable for electron microscopy. This is the same process used to separate larger nanoparticles from smaller ones and thus the STEM sample prep inadvertently causes larger particles to be kept while smaller ones in the supernatant are typically discarded. Indeed, the length histograms of the three QR samples prepared for STEM imaging in the standard way, with representative images shown in Figure 8.3 (a), (b) and (c), have only one peak that is fitted well with a Gaussian distribution (Figure 8.4 (a)).

To determine the nature of the particles that are normally discarded during the ”washing” process, some of the typically discarded supernatant product was collected and examined. Figure 8.5 shows a photo of the QR solution after centrifugation. The top, slightly colored layer is the liquid from which the sample was taken. This is typically the layer discarded in the STEM sample preparation process, along with the white, organic layer. The dark pellet of QRs in the very bottom is the part typically kept and resuspended for STEM analysis. In Figure 8.4 (b), the length histogram of QRs from a supernatant sample taken from a 45min growth solution after a single wash is shown. The image of the QRs in this sample is shown in Figure 8.3 (d). The histogram of the QR length in the supernatant shows two distinct peaks, giving evidence of the presence of smaller particles, which are also seen in low-magnification images, an example of which is shown in Figure 8.6. The bimodal length distribution is in stark con-

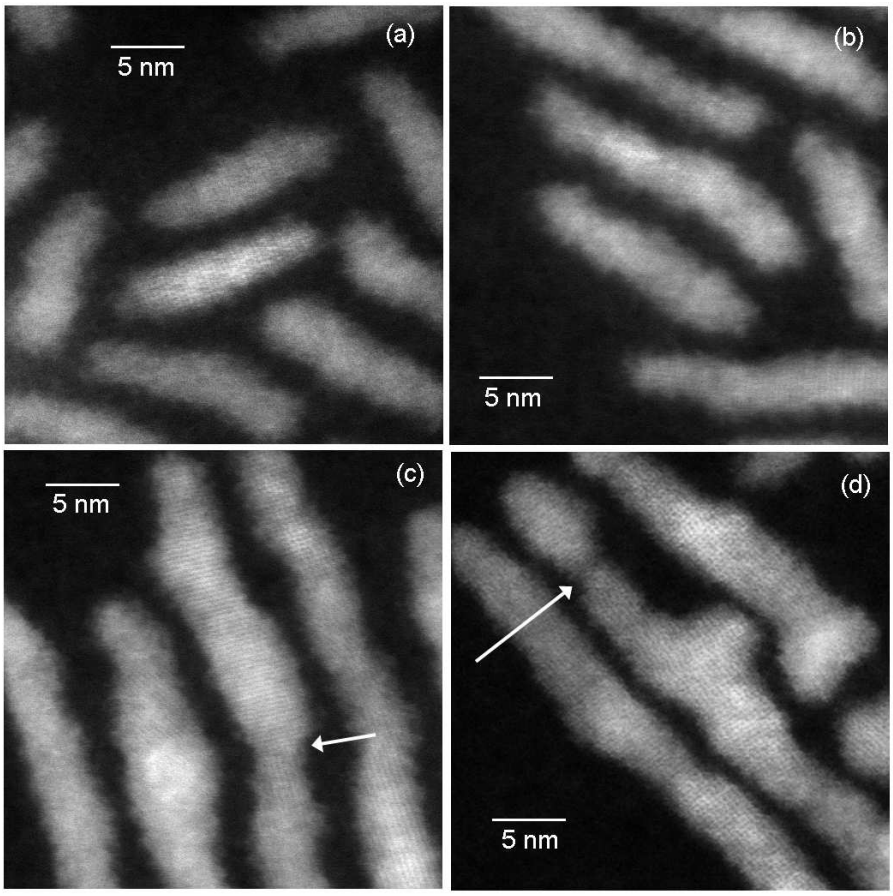

Figure 8.3: ADF images of CdSe QRs grown (a) for 10 minutes, (b) for 20 minutes, (c) for 45 minutes and (d) for one hour. The shorter QRs grown for shorter times in (a) and (b) exhibit only single-crystal lattices. The longer QRs in (c) and (d) exhibit both multiple lattice fringes along the length and necks of low intensity suggesting joining of two QRs (white arrows).

trast to the length histograms of the three samples prepared for STEM imaging in the standard way, which displayed only a single Gaussian distribution.

8.3 Conclusions

The method of oriented attachment to describe QR growth has been proposed before, but is further reinforced as a viable description by examining ADF STEM

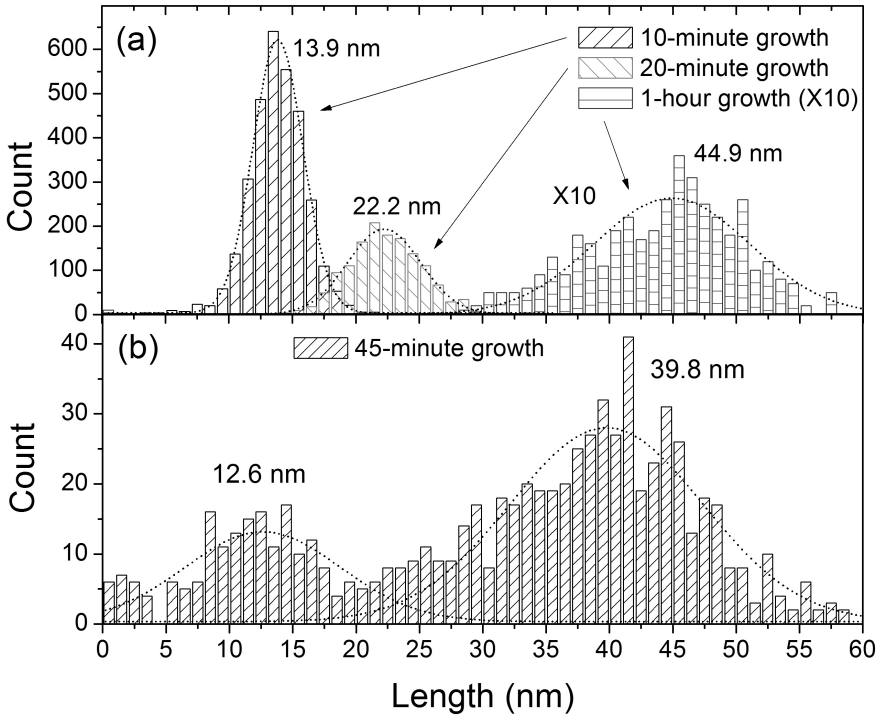

Figure 8.4: Histograms of the number of QRs as a function of length for QRs grown for different lengths of time. The QRs are the same shown in the images displayed in Figure 8.3. (a) Plot shows single-peak length histograms for three samples washed prior to microscopy. (b) Plot shows the length histogram for a sample taken from the normally discarded wash product. This displays what seems to be two peaks.

images and deriving from them length histograms of the QRs in the image. When the sample is carefully prepared and cleaned so as to not sift out the small rods that may be present, it is clear that there are multiple lengths of rod in the samples grown for long periods. The length distribution is not continuous, but displays distinct peaks as would be expected from a sample of QRs attaching together to make longer rods. This attachment can also be inferred from examining ADF images of long QRs and observing multiple crystal lattice

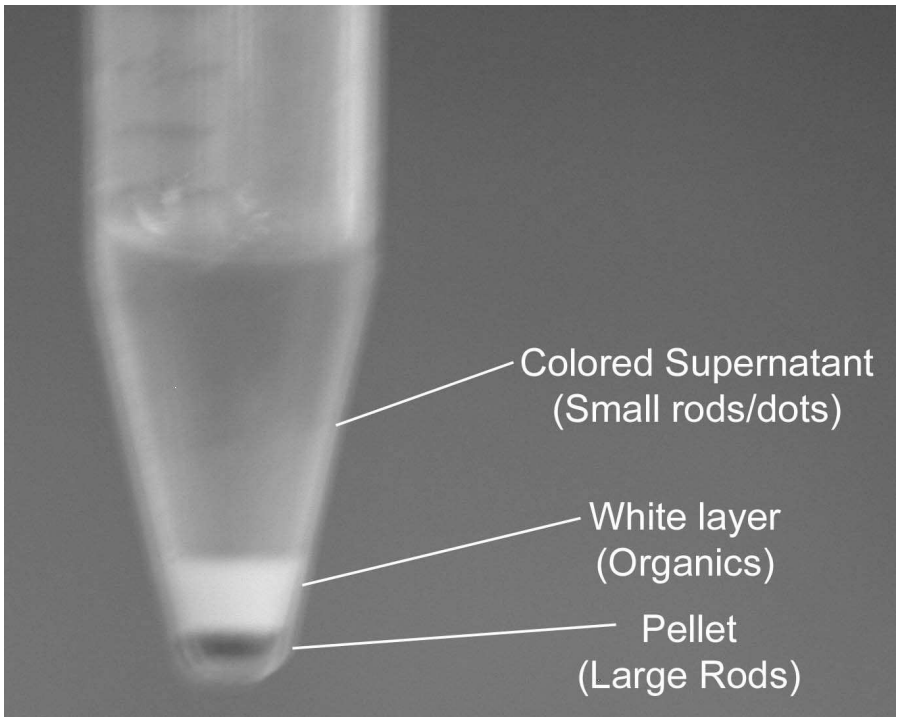

Figure 8.5: Photograph of the suspension of QRs grown for 45 minutes after the first step of the washing process and centrifugation. The suspension has divided into three distinct densities and materials. The upper, amber colored region is the supernatant typically discarded during the washing process. Below this is a white region of organics, and the very bottom is a dark pellet of densely packed QRs. Typically this is kept, diluted and placed into STEM. Photo courtesy Jack Calcines.

structures along the length and narrow necks between two joining nanoparticles. Together with the previous evidence given by nanodiffraction, this is a strong argument for oriented attachment being a growth mechanism on par with diffusion growth in importance.

8.4 Appendix

To obtain the length and width histograms for the QR samples, several low-resolution images were taken of large rafts of rods for each sample. The bound-

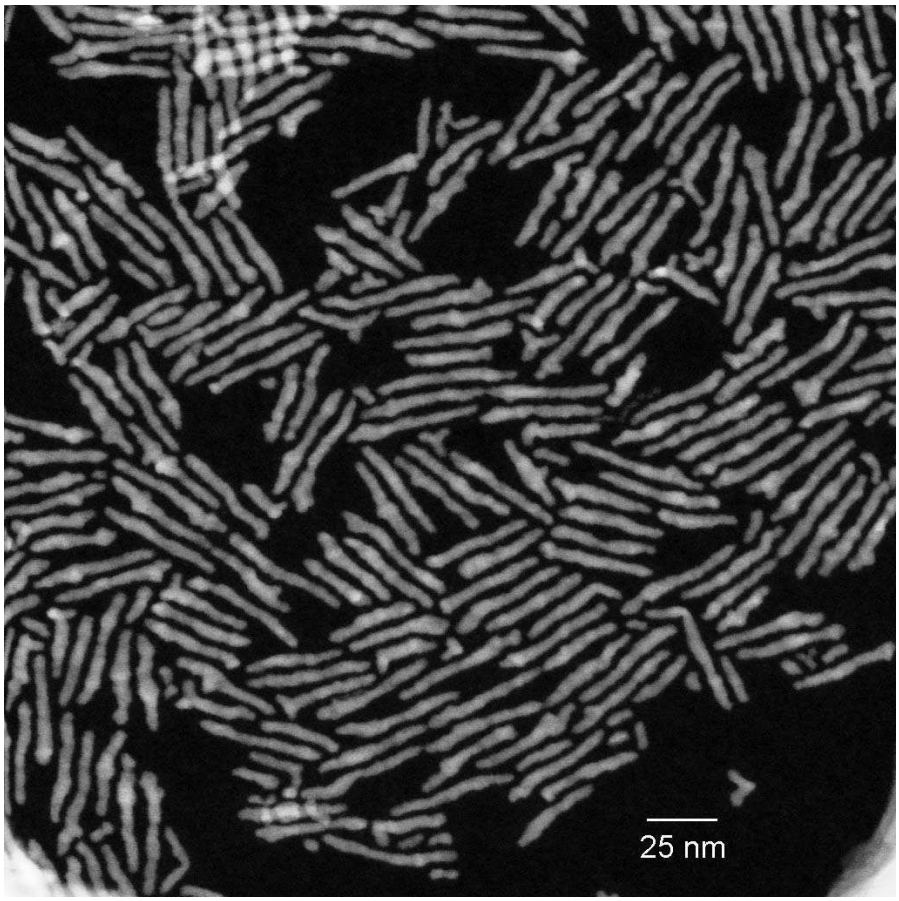

Figure 8.6: ADF image of the supernatant of the sample of QRs grown for 45 minutes. Both long and short QRs can be seen within this sample.

aries of the QRs were picked out from the images using an intensity histogram and varying the range of intensity chosen until it included only the bright QRs up to the edge. There is some uncertainty as to where the ”edge” of the rods should be determined, so after ”eyeballing” a best guess for the edge, the location for the minimum intensity in the intensity histogram is noted and the process is done several times. The error for where the location of the edge is found by the minimum and maximum of the picked intensity. An example of an intensity histogram with the chosen intensities down to the minimum is shown in Figure 8.7.

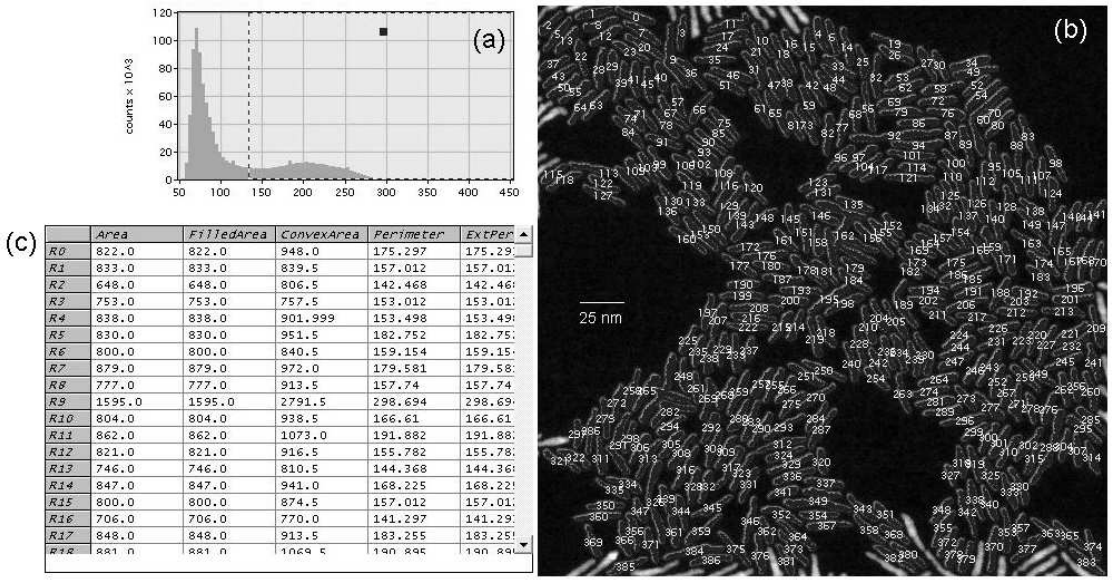

	Area	FilledArea	ConvexArea	Perimeter	ExtPer
R0	822.0	822.0	948.0	175.297	175.29
R1	833.0	833.0	839.5	157.012	157.01
R2	648.0	648.0	806.5	142.468	142.46
R3	753.0	753.0	757.5	153.012	153.01
R4	838.0	838.0	901.999	153.498	153.49
R5	830.0	830.0	951.5	182.752	182.75
R6	800.0	800.0	840.5	159.154	159.15
R7	879.0	879.0	972.0	179.581	179.58
R8	777.0	777.0	913.5	157.74	157.74
R9	1595.0	1595.0	2791.5	298.694	298.69
R10	804.0	804.0	938.5	166.61	166.61
R11	862.0	862.0	1073.0	191.882	191.88
R12	821.0	821.0	916.5	155.782	155.78
R13	746.0	746.0	810.5	144.368	144.36
R14	847.0	847.0	941.0	168.225	168.22
R15	800.0	800.0	874.5	157.012	157.01
R16	706.0	706.0	770.0	141.297	141.29
R17	848.0	848.0	913.5	183.255	183.25
R18	881.0	881.0	1069.5	190.895	190.89

Figure 8.7: Example of the (a) intensity histograms, (b) images with particles picked and numbered and (c) dimension data of the picked particles produced by the particle analysis software, Digital Micrograph. The data is then plotted as a length histogram to find the average lengths of QRs in the sample.

Once an intensity for the edge is picked, this intensity is maintained for each image taken of the sample. This is done by determining and maintaining the relative distance between the picked intensity to two marker peaks in the intensity histogram. The first marker peak is that from the high intensity resulting from the QRs and the second marker peak is that from the low intensity resulting from the carbon substrate. When the images are kept contamination-free and are taken with the same dwell times, this location will remain the same for the same sample. This picked intensity is chosen for each different sample, and maintained throughout the images for each sample.

Once the edges of the QRs are found, the particle picking software from Digital Micrograph is used to transform the picked intensities from the intensity histogram into solid particles. These particles are analyzed by the particle picking software for length. Picked QRs on the edge of the image or crossing

with other rods are discarded and the length values for the remaining QRs are copied into a plotting program, producing length histograms.

BIBLIOGRAPHY

[1] E.C. Scher, L. Manna, A.P. Alivisatos, Phil. Trans. R. Soc. Lond. A **361**, 241 (2003).

[2] Z. Yu, M.A. Hahn, J. Calcines, T.D. Krauss, J. Silcox, App. Phys. Lett. **86**, 013101 (2005).

[3] Z. Yu, M.A. Hahn, S.E. Maccagnano-Zacher, J. Calcines, T.D. Krauss, E.S. Alldredge, J. Silcox, ACS Nano **2**, 1179 (2008).

[4] R.L. Penn, J.F. Banfield, Geochem. Cosmochim. Acta **63**, 1549(1999).

[5] J.F. Banfield, S.A. Welch, H.Z. Zhang, T.T. Ebert, R.L. Penn, Science **289**, 751 (2000).

[6] R.L. Penn, J.F. Banfield, Am. Mineral. **83**, 1077 (1998).

[7] Z. Yu, M.A. Hahn, J. Calcines, T.D. Krauss, J. Silcox, App. Phys. Lett., 179 (2004).

[8] Z. Tang, N.A. Kotov, M. Giersig, Science **297**, 237 (2002).

CHAPTER 9

CONCLUSIONS

9.1 Summary

An electron microscopist often finds herself fulfilling two different roles in her career; that of material pathologist and scientist. Materials pathology, a term coined by Prof. Silcox, is the work of assisting materials scientists in characterizing their materials to discover what is actually happening in the physical construction and bonding, as can be discovered with (S)TEM. As a graduate student, there were many opportunities for me to examine materials created by other groups. Todd Krauss's group of chemistry students created many quantum nanoparticles for me to examine. Li Guo was growing CdSe QDs that she was experimentally capping with SrSe and needed help discovering if Sr was actually on the QD and what kind of capping was being achieved. Jeff Peterson was growing PbS QDs and studying the effect of photooxidization on the emission as a function of QD size, whose size measurements were done quickly and accurately in STEM [1]. Lisa Carlson was growing CdTe/ZnS core/shell QDs that needed characterization, and Jaques Calcines provided copious amounts of excellent CdSe nanorods for personal study as well as for studies of his own. All of the quantum nanorods in this thesis were grown by Calcines. The Webb group at Cornell provided some interesting opportunities to study different materials as well. Jie Yao provided some examples of high-quantum-yield QDs and low-quantum-yield QDs for comparison in STEM. Also, Huizhong Xu provided samples of Cornell Dots, which are silica shells covering a silica core embedded with dye molecules producing a bright and stable dye particle. A collaboration

with Kodak provided samples of QDs and quantum wires being grown for use in a QD-based light-emitting diode.

I was fortunate enough to have the opportunity to do a lot of science with the STEM as well, and the bulk of this thesis consists of those studies. In the struggle to match simulation to experimental STEM ADF images and CBED patterns, three different possible sources of intensity reduction were examined: amorphous layers, inelastic scattering and small tilts of the specimen.

Analysis using multislice simulations indicates that as the probe propagates through amorphous material it has a component of the beam that is simply defocused and a component that is scattered into a Gaussian-like background. This background decreases contrast in the ADF image no matter if the amorphous layer is on the top or bottom of the specimen, but more contrast reduction is seen when the amorphous layer is on the top.

In considering the role of inelastic scattering in intensity reduction, a direct comparison of experiment with theory was accomplished using single-electron detection for CBED patterns for amorphous silicon samples. A close match was made between experimental and theoretical CBED intensities when multiple inelastic scattering, approximated by bulk plasmon scattering, was included into the multislice simulations.

The use of multislice modelling to simulate highly-controlled specimen tilts of 25 nm-thick crystalline silicon samples has shown that even small tilts, on the order of 10-15 mrad, have been found to reduce the contrast of ADF-STEM images by as much as a factor of two, and increases as the thickness of the sample increases. This is true for both uncorrected and corrected STEM probes. The

coherent effects due to the propagation of the probe through a slightly off-axis crystal sample can be readily seen in LAADF images, making LAADF an intriguing tool for detecting small tilts while running the microscope, avoiding the need to change the optics in order to take a diffraction pattern to test for tilts off-axis.

It can be concluded that for crystalline samples, amorphous layers and small tilts will reduce the contrast of ADF STEM images when present. Tilt can be detected and eliminated, but amorphous layers cannot be avoided in every case and cannot be measured to determine their thickness to allow for a more accurate simulation. Amorphous layers will, therefore, remain an unknown in the simulation of ADF STEM images. Inelastic scattering can be included in amorphous samples to closely match simulation with experiment.

The use of STEM to understand quantum nanoparticles was also explored in this thesis. The damage of CdSe nanoparticles has been detected both with ADF STEM image intensity reduction and through core-loss EELS integration reduction. Using EELS, the rate of Cd loss from the sample was measured and found to be detectable when there is no carbon protecting the exit surface of the nanoparticle. When the carbon substrate is oriented so that it protects the exit surface of the nanoparticle there is no mass-loss detected, but a white spot sometimes appears at the damage site, most likely due to beam scattering from the disordered crystal. The detection of a nanodiffraction pattern from the nanoparticle is stable even under long electron-probe exposure.

The Mott cross-section of surface Se atoms is relatively large in the energy range of the 100 keV electrons used in the Cornell VG STEM, but the surface Cd Mott cross-section becomes non-zero somewhere near 100 keV. The uncertainty

of the exact location of the surface Cd threshold energy can be eliminated with an accurate value for the cohesive energy of CdSe in nanoparticles. However, this is a difficult enterprise considering the cohesive energy is known to change as particles reduce in size and become quantum particles. This is due to the large number of surface atoms (~30-55% of the total atoms in the particle) and the surface reconstruction that is known to occur.

Multislice simulations were used to confirm that the intensity of ADF images of small, single-crystal nanoparticles can be used to interpret the thickness and the shape of the particles. Faceting of quantum rods and dots has been detected, and in some cases the intensity profiles of faceted particles can be quickly translated via a thickness profile to a particular shape. Those ADF images of quantum particles that do not show ideal faceting behavior can be used to assist identification of deviation from the ideal and thereby, to some degree, help understand the growth or shelling abnormalities that may exist in the sample.

ADF STEM images were also used to obtain length histograms of nanorod samples, and it is found that when the sample is carefully prepared and cleaned so as to not sift out the small rods that may be present, it is clear that there are multiple lengths of rod in the samples grown for long periods. The histogram displays distinct peaks for nanorod length as would be expected from a sample of nanorods attaching together to make longer rods, as can also be inferred from examining high-resolution ADF images.

STEM was, therefore, shown to be effective in measuring damage, shape and growth mechanisms of quantum nanoparticles.

9.2 Future Work

There are several areas of study suggested by the work in this thesis. Considering the success of using calculated multiple inelastic scattering with simulated CBED patterns to match the intensities of experimental CBED patterns of amorphous Si, it would be useful to expand the method and include inelastic scattering in multislice simulations of crystal specimens. This cannot be achieved using the exact method outlined in this thesis because the interaction of the electron probe with the crystal would create many incoherent effects that would need to be accounted for as the probe moved through the sample. The method could, therefore, be altered to allow convolution of the calculated plasmon loss cross-section with the electrons in the probe at each slice in the multislice simulation program. This would entail changing the multislice code, but is feasible and could produce simulated images that more closely reflect the intensities found in experimental images of crystal specimens.

The study of damage of CdSe nanoparticles revealed the uncertainty of the cohesive energy of CdSe in nanoparticles. A further study in this damage experiment would be to measure damage in bulk CdSe to attempt to calculate the cohesive energy in that case using the rate of mass-loss of surface Cd. When the value of the cohesive energy is more fully understood in the bulk case, and the rate of mass-loss in the bulk sample matched to the simple calculation, an intermediate case can also be studied; that of a CdSe nanowire. Nanowires are exceedingly long in the z-direction, but are varying in thickness. Some nanowires can be found that are ten times the radius of quantum nanorods, but some are the same radius as nanorods. Damage experiments can be done on nanowires whose radii are somewhere between the two extremes of bulk and quantum

nanorods in an attempt to understand the role the surface reconstruction on the nanorods has on the cohesive energy of CdSe.

Finally, several new studies can be done taking advantage of the new aberration-corrected STEM at Cornell. The Nion UltraSTEM has a high beam current which allows for EELS mapping of samples. I propose to expand the study mentioned briefly in Chapter 2 where the core of a CdSe/ZnS core/shell quantum dot was detected using core-loss EELS to detect the relative abundance of Cd. Using the Nion UltraSTEM, an EELS map can be made of a core/shell quantum dot, giving an even more accurate measure of the location and size of the core, as well as the distribution of the shell material. This could be instrumental in discovering the distribution of the core and shell material in the unblinking, sintered CdZnSe/ZnSe core/shell QDs described in the Introduction [2]. Of the three types of atoms in the unblinking dot, only the Cd atom gives adequate EELS signal for EELS mapping. It is proposed that if the shell material, ZnSe, can be replaced with ZnS the S atoms can provide enough signal to collect an EELS map of the shell (S) to accompany an EELS map of the core (Cd). Such a map may provide enough evidence to confirm or disprove the suspicion that the boundary between the core and shell of this unblinking dot is gradual, upon which the theory of its unblinking nature is based.

A study that can be done on the new Nion aberration-corrected STEM is to take advantage of the dual dark-field detectors installed in the microscope and experimentally confirm the artefacts of tilt seen in crystal specimens in LAADF that are not seen in HAADF reported with simulations in Chapter 5. The two ADF detectors are mounted such that they can be used in unison and the sample holder can be tilted with angles accurately measured and controlled, allowing

for an experimental equivalent. This would be a good experimental confirmation that using LAADF in conjunction with HAADF for crystal samples allows the microscope operator to detect small tilts without switching the optics to diffraction conditions.

Another proposed study taking advantage of the aberration-corrected STEM and its high beam current is to continue the study of oriented attachment of CdSe nanorods. It has been proposed that a dominant growth mechanism for these rods is the oriented attachment of smaller rods (sub-particles) in the growth solution, creating long, multi-crystal rods. It was reported by Yu et al. [3] that the crystal orientation between two sub-particles in an individual nanorod could be twisted by as little as two to three degrees. If one considers the interface between the regions as two ideal crystal faces, in order for a twist in the joining of the two faces to be energetically favorable it would be necessary to have several of the atomic columns align and provide the bonding between the sub-particles. A twist of as few as two or three degrees in areas as small as the nanoscale quantum rods would not allow the necessary column alignments. Ideal nanocrystals would be unstable in such an arrangement and snap back to perfect alignment. Therefore, it is proposed that perhaps the organic ligands themselves allow for smaller twists in the interface between sub-particles. One possibility is that organic ligands coating the outer surfaces of the subparticles interact and provide the necessary bonding, like smearing peanut butter on the outer edges of two Lego blocks and sticking them together. The peanut butter would provide enough sticking power to hold the blocks together even if they were rotated so they could not snap in to place. Another possibility is that the organic ligands are still involved somewhat on the interface crystal faces, interacting with the atoms and organic ligands on the opposite face and assisting

in the bonding. This possibility could be likened more to the sticking power of the white stuff in an Oreo cookie. With either possibility, the plausibility of this proposal could be tested by mounting the CdSe nanorods on a substrate that contains carbon and acquiring an EELS map of the placement and relative abundance of carbon on the rods. If the proposed assisted-bonding situation is occurring, there may be evident a greater amount of carbon in and beside the interfaces between sub-particles.

BIBLIOGRAPHY

[1] J.J. Peterson and T.D. Krauss, Phys. Chem. Chem. Phys. **8**, 3851-3856 (2006).

[2] X. Wang, X. Ren, K. Kahen, M.A. Hahn, M. Rajeswaran, S. Maccagnano-Zacher, J. Silcox, G.E. Cragg, A.L. Efros and T.D. Krauss, Nature **459**, 686-689 (2009).

[3] Z. Yu, M.A. Hahn, J. Calcines, T.D. Krauss, J. Silcox, App. Phys. Lett. **86**, 013101 (2005).

APPENDIX A

APPENDIX–PLASMON DISPERSION CALCULATION

In a solid, the valence electrons can be modeled as coupled oscillators interacting with one another and with the fast incident electron via electrostatic forces. These electrons can be thought of as essentially free particles in a free-electron "gas". This free-electron gas interacts weakly with the ions in the lattice, with the interaction included by simply modifying the standard rest mass of the electrons, m_0, to an effective mass, m, and by introducing a damping constant, Γ, from which one can derive a damping coefficient of $\Delta E_P = \hbar\Gamma$. When the free-electron gas interacts with an external electric field, such as a fast incident electron transmitting through the sample, there is a collective response of oscillations in the gas with a characteristic frequency, ω_P. This collective response would continue forever except for the introduction of the damping from the lattice. This collective frequency of the free-electron gas can be thought of as creating a pseudoparticle of energy, $E_P = \hbar\omega_P$, called a plasmon. There can be different types of plasmons, most notably those caused in the bulk of the sample, called bulk plasmons, and longitudinal plasmon oscillations propagated in the surfaces of the sample, called surface plasmons. This Appendix will concentrate solely upon bulk plasmons.

The distribution of energies of the plasmon as a function of angle is given by the plasmon dispersion relation,

$$E_P = E_{P,0} + 2\gamma E_0(\theta^2 + \theta_E^2), \tag{A.1}$$

where θ is the scatter angle, θ_E is the characteristic angle of scatter with relativistic correction included, and γ is the dispersion coefficient. The cross-section

of single-bulk-plasmon generation by a fast electron that loses energy E and scatters to the angle θ can be expressed as [5, 6]:

$$\frac{\partial^2\sigma}{\partial E\partial\Omega} = \frac{D}{2\pi^2 n a_0}\frac{1}{E_0}\frac{1}{\theta^2+\theta_E^2}\times \frac{E\Delta E_P E_{P,0}^2}{\left[E^2-E_{P,0}^2-4\gamma E_{P,0}E_0(\theta^2+\theta_E^2)\right]^2+E^2\Delta E_P^2} \tag{A.2}$$

where D is the normalization constant, n is the atomic density of the specimen, a_0 is the Bohr radius, E_0 is the incident electron energy and $E_{P,0}$ is the plasmon energy at θ=0.

Figure A.1 shows a plot of the cross-section of Si as a function of energy, E, and scatter angle, θ. A significant drop of the cross-section with increasing scattering angle is observed. The cutoff angle, θ_0, marked on the plot indicates the angle at which the plasmon is absorbed by the material either as phonons or by obtaining enough energy to scatter an electron into the valence band. Also marked is the plasmon energy for Si at k_0, $E_{P,0}$. It should be noted that for very thin specimens, typically <10nm, where the bulk plasmon scattering is not the dominant mechanism, the inelastic scattering caused by surface plasmon excitations becomes equally as important or more important than bulk plasmon scattering and must be considered.

In Chapter 4, simulated CBED patterns are modified to include inelastic scattering from bulk plasmons by scaling them with the probability of a single plasmon generation, $\beta = (\Delta t/\lambda_{pl})\exp(\Delta t/\lambda_{pl})$ and convoluting them with the angular distribution of the plasmon cross-section. To produce the angular distribution of the plasmon cross-section, the bulk plasmon cross-section is integrated over energy and plotted as a 2-D plot as a function of scattering angle. Figure A.2 shows a calculated plasmon cross-section integrated over energy from 0-300 eV.

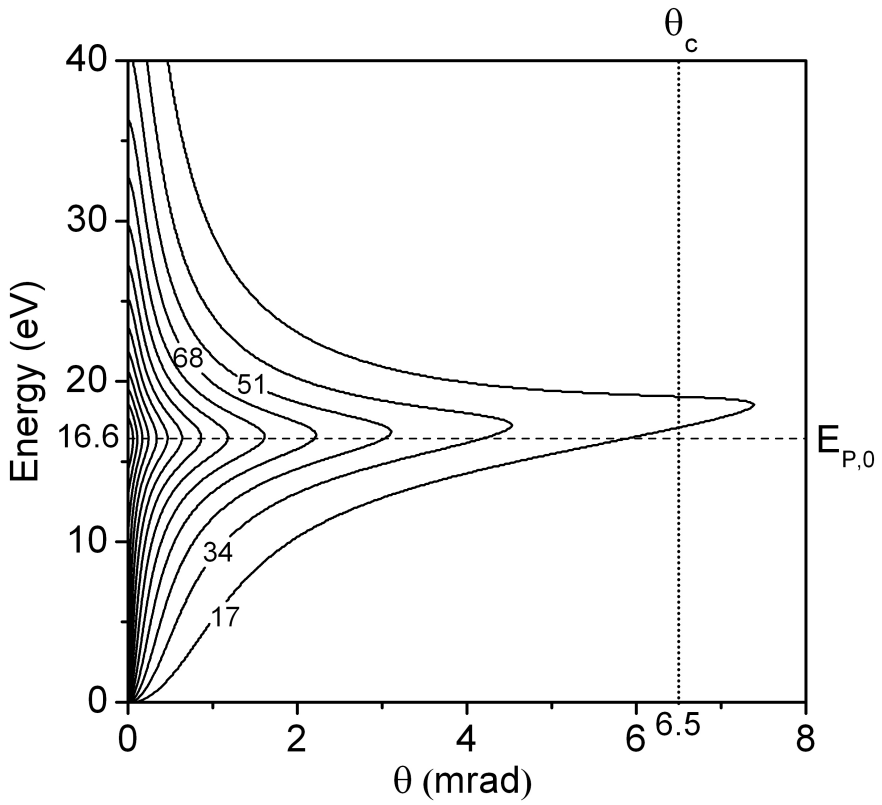

Figure A.1: Silicon bulk plasmon cross-section as a function of energy and scatter angle. The value of plasmon energy at k_0, $E_{P,0}$, as well as the cutoff angle, θ_0 are marked.

The inset shows the complete 2-D plot of the cross-section as a function of scattering angle and is the form in which the convolution with the simulated CBED patterns took place in Chapter 4. These plots represent the cross-section of a single inelastic scattering of the incident electron by the bulk plasmon. To include the possibility of multiple scattering, therefore, this cross-section is convoluted with the simulated CBED patterns a number of times depending upon the thickness of the simulation sample. For the process described in Chapter 4, it was found sufficient to convolute $t/\Delta t$ times, where t is the thickness of the sample and $\Delta t = \lambda_{pl}/16$, where λ_{pl} is the plasmon mean-free path. If the sample was not an even multiple of Δt, the number of convolutions performed was P+1, where

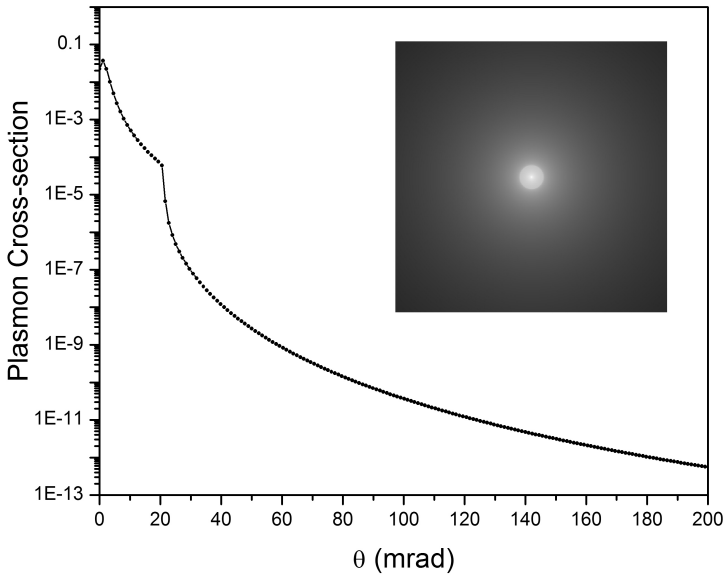

Figure A.2: Silicon plasmon cross-section integrated over energy, from 0-300 eV, and plotted as a function of scatter angle. The inset shows the 2-D plot of the plasmon cross-section. The axis of the 2-D plot represents 400 mrad.

P is the maximum integer times Δt that does not exceed t.

To make the process used in Chapter 4 more clear, the following is a simple algorithm of the process used to scale and convolute the simulated CBED patterns to include inelastic scattering as calculated by the cross-section for a single inelastic scattering of the incident electron.

Input A; (*Read in CBED image and crop to 256 x 256 pixels.*)

thick = (thickness of sample); (*Determine thickness of sample in CBED image.*)

Input B; (*Read in plasmon loss cross-section matrix and crop to 256 x 256 pixels.*)

Δt = $\lambda/16$; (*Divide mean free path value by chosen value.*)

P = integer(thick/Δt); (*Divide t by Δt and change to integer.*)

```
if P==0;
    t = thick;
else;
    t = thick-P*Δt;
    for i=1 to P;
        β = (Δt/λ)*exp(-Δt/λ); (For every section calculate scaling.)
        A = A*(1-β) + β*A⊗B; (Scale A and convolute with B.)
    end;
end;

newβ = (t/λ)*exp(-t/λ); (If thick < λ, this convolutes first and final time. If thick > λ, this convolutes the remainder.)
finalA = A*(1-newβ) + newβ*A⊗B;

Figure out the area under the central disc using a mask wherein every pixel not in the central disc has a value of 0, and every pixel in the central disc has a value of 1.
Input C; (Read in mask calculated from initial probe, central disc value is not zero.)
for i=1 to 256; (For every pixel in image...)
    for j=1 to 256;
        if C(i,j) == 0; (...where the pixel value of mask=0...)
            finalA(i,j) = 0; (...remove pixel value from convoluted CBED image.)
            initialA(i,j) = 0; (Also mask off unaltered initial CBED image.)
        end;
    end;
end;
```

fAsum = sum(sum(finalA)); (*Integrate all of finalA image after masking*.)

iAsum = sum(sum(initialA)); (*Integrate all of initialA image after masking*.)

Ratio = iAsum/fAsum; (*Find the ratio representing the change the plasmon loss has made to the initial image integration*.)

BIBLIOGRAPHY

[1] H. Watanabe, J. Phys. Soc. J. **11**, 112 (1956).

[2] H. Raether, in Vol 38 of *Springer Tracts in Modern Physics*, edited by G. Höhler (Springer-Verlag, Berlin 1965), p.85.

[3] P.E. Batson and J. Silcox, Phys. Rev. B **27**, 5224 (1983).

[4] R.F. Egerton, *Electron Energy Loss Spectroscopy in the Electron Microscope, 2nd edition* (Plenum, New York, 1996).

[5] R.H. Ritchie and A. Howie, Philos. Mag. **36**, 463 (1977).

[6] K.A. Mkhoyan, T. Babinec, S.E. Maccagnano, E.J. Kirkland and J. Silcox, Ultramicroscopy **107**, 345 (2007).

[7] In specimens with thickness $\Delta t=\lambda_{pl}/16$, the ratio of probabilities for single to double plasmon generation, described by Poisson statistics, is $\beta_1/\beta_2=2\left\lfloor\lambda_{pl}/\Delta t\right\rfloor=32$.